The history of the Bachkovo-Dobralak metamorphic unit of the Upper Rhodopian terrane, Bulgaria

Collapse folds in the Rhodope Mountains indicating extension, explained on page 23

Master thesis; Utrecht University

Author: Olfert, N.C., MSc student (3471977)
Supervisor: Matenco, L.C.
2nd Supervisor: Pleuger, J.

Abstract

The Rhodope massif is located in southern Bulgaria and northern Greece, north of the Aegean Sea. The Rhodope massif was affected by different stages of deformation and metamorphism during Mesozoic-Cenozoic times. It is situated in the transitional area between the late Jurassic – late Cretaceous shortening recorded in the Dinaric – Hellenic orogen by the N-ward subduction and collision of the Neotethys Ocean and the Cretaceous – Eocene shortening recorded in the Carpatho-Balkanides orogen by the S-ward subduction and collision of the Ceahlau-Severin Ocean, an eastern branch of the Alpine Tethys. Partly coeval and post-dating this orogenic build-up, the Rhodope was affected by the formation of a large core-complex starting with the Middle Eocene times, the driving extension being associated with the formation of a number of well-known top-S to SW detachments, such as Kerdilion and Strymon. The northern boundary of the core-complex in Bulgaria is marked by a significant number of kinematic indicators showing top-N sense of shear. It is rather unclear if this stretching took place in response to the earlier nappe stack kinematics or formed as result of local detachments dipping N-wards, mechanically accommodating the exhumation of the large dome. They could have accompanied the formation of extensional basins at the northern boundary of the core-complex starting in late Eocene times, such as the Plovdiv Basin. We have studied the balance between orogenic nappe stacking and subsequent extensional collapse in part of the Upper and Uppermost units of the northern Rhodope, by a field kinematic study followed by microstructural observations and laboratory analysis. The results demonstrate that a top NW-NNW shearing event documented in the upper Rhodope was associated with burial and prograde metamorphism during nappe stacking. This event was subsequently followed by one other tectonic deformation, characterized by pervasive top – ENE to NE senses of shear and retrograde metamorphism. This deformation is interpreted as an extensional detachment exhuming the deeper Rhodope units previously buried by the nappe stack. The deep exhumation of the Rhodope core-complex has probably reached a situation in which the extension was not accommodated anymore by top-S sense of movement and led to the formation of a number of local top-N detachments sustaining the continuation of footwall uplift.

Local top-N detachment resulted in the unloading of originally structurally deeper rocks that are thought to have been subject to rapid retrograde metamorphism (partly) overprinting earlier prograde metamorphic characteristics.

Table of contents

1 – Introduction

The Rhodope massif is located in southern Bulgaria and northern Greece, north of the Aegean Sea. It evolved as a consequence of different stages of deformation and metamorphism, covering the period Mesozoic-Cenozoic. Shortening and continental collision led to nappe stacking contrasting transport directions.

Contractional deformation took place during the late Jurassic – late Cretaceous. Shortening in the Dinaric – Hellenic orogen is recorded by the N-ward subduction and collision of the Neotethys Ocean and during the Cretaceous – Eocene, shortening is recorded in the Carpatho-Balkanides orogen by S-ward subduction and collision of the Ceahlau-Severin Ocean, an eastern branch of the Alpine Tethys (e.g. Jahn-Awe *et al.*, 2010, Okay *et al.*, 2001).

The Cenozoic extension formed core complexes, exhuming the previously buried high-grade rocks during nappe stacking (Ivanov, 1988; Burg *et al.*, 1990, 1996b).

Cenozoic extension is represented by top-to E-NE (e.g. Bonev & Beccaletto, 2007) and top-to ±S sense of shear (e.g. Krohe & Mposkos, 2002).

The period of orogenic contraction was followed by extension that started ~40Ma, continued throughout the Miocene and resulted in the formation of the Rhodope core complex that formed by dominantly top-S to SW sense of shear (e.g. Sokoutis *et al.*, 1993; Krohe & Mposkos, 2002; Brun & Sokoutis, 2007; Jolivet *et al.*, 2010). The exhumation of the core complex was accommodated laterally by the formation of local detachments with top to ENE sense of shear (e.g. Bonev & Beccaletto, 2007) while along its western strike, extensional deformation is gradually reduced in the Kraishte area of western Bulgaria (Kounov *et al.*, 2004; 2010).

Based on the initial nappe stack burial and subsequent exhumation, the Rhodope metamorphic units can be structurally grouped in four major unit systems (Schmid *et al.*, 2011). The lower units contain a pre-Mesozoic continental basement and metamorphosed Mesozoic cover (the Pangaion or Drama unit, Turpaud & Reischmann, 2010). The middle units contain a variegated series of metamorphosed sediments, plutons and mafic material, including eclogites thought to be the relicts of a major suture zone located south of a late Jurassic island arc (e.g., the Nestos suture zone, Krenn *et al.*, 2010). The upper units contain the metamorphosed remnant of this island-arc exhumed during the formation of the core-complex. The upper units are heterogeneous in nature and have been affected by high-grade metamorphism (amphibolite facies to anatectic at the base of the unit). They often contain rocks diatexitic, as well as metatexitic in nature, indicating peak temperatures of 700-750˚C (e.g., such as in the Chepinska tectonic unit, Naydenov *et al.*, 2013).

The uppermost units of the Rhodope contain a continental basement and Mesozoic cover affected by upper greenschist facies to lower amphibolite facies metamorphism displaying top-to N sense of shear. The upper and uppermost tectonic units of the Rhodope were interpreted to be separated by an extensional detachment that reactivated a former thrust from the previous nappe stack system (the N Rhodope detachment, Schmid *et al.*, 2013).

The studied area, located roughly S of the city of Plovdiv in Bulgaria, is situated at the northern boundary of the extensional system, near the structural contact between the Upper and Uppermost Rhodope units. In the Upper units to the west and south, the Madan, Asenitsa and Chepinska units display top-to S sense of shear, while the Bachkovo-Dobralak unit displays top-to E to NE, as well as top-to S sense of shear (Burg, 2011). In their hanging-wall, the uppermost units show pervasive top-N senses of shear (Schmid *et al.*, 2013).

It is rather unclear if all this stretching took place in response to the earlier nappe stack kinematics or formed as result of local detachments dipping N-wards, mechanically accommodating the exhumation of the large dome and accompanied by the formation of extensional basins that formed with the late Eocene basin at the northern boundary of the core-complex. Top-to-NW shear sense criteria have usually been associated with accretion of a Mesozoic sequence onto the Rhodope margin (Bonev and Stampfli, 2003), nappe stacking and high-grade metamorphism (e.g. Jahn-Awe *et al.*, 2010, Okay *et al.*, 2001). Top-to E to NE sense of shear in the Bachkovo-Dobralak unit has been associated with extension, post-dating the prograde metamorphism (e.g. Bonev & Beccaletto, 2007).

We have studied the balance between orogenic nappe stacking and subsequent extensional collapse by a field kinematic study followed by microstructural observations and laboratory analysis in the Bachkovo-Dobralak and adjacent units of the northern Rhodope. In particular we aim to study the metamorphism associated with the various deformation events observed, in order to derive the genetic mechanism and discriminate between the effects of nappe stacking and subsequent extension.

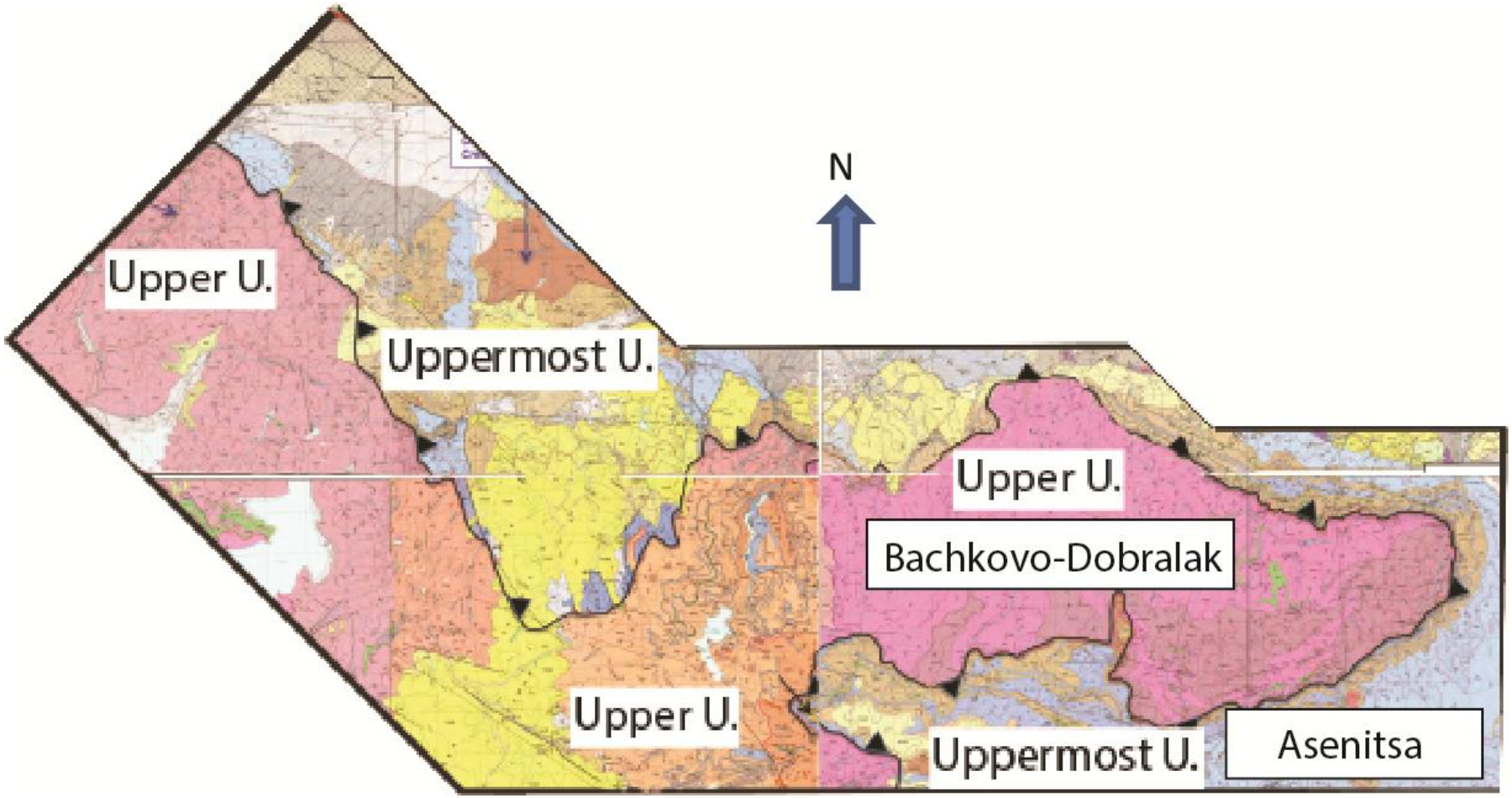
N
Upper U.
Uppermost U.
Upper U.
Bachkovo-Dobralak
Upper U.
Uppermost U.
Asenitsa

Figure 1 - The fieldwork area of this study, showing the Upper unit and Uppermost unit, after Bulgarian geological map sheets and Schmid *et al.* (2013). The top of the image is directed towards the east. The North-Rhodopean detachment fault (NRDF) represents a former thrust which is possibly reactivated as a consequence of extensional tectonics. The geographical location of this map is obvious from appendix 1.1, figure 1, in which the fieldwork area is provided as inset.

2 - Geological background

In the northern part of the Rhodope, the Maritsa Shear Zone (MSZ) and the recent Maritsa basin separate the Rhodope massif from the Sredna Gora volcanic arc, a late Cretaceous (Turtonian-Maastrichtian) volcanic arc and back-arc basin, and the Balkan mountain range (Naydenov *et al.*, 2013). The southern limit of the Rhodope massif is the Aegean Sea, a back-arc basin stretching in age from Miocene to recent. The south-western border of the Rhodope massif is represented either by the Vardar suture zone (Ricou *et al.*, 1998), or the Serbo-Macedonian Massif (Kockel & Walther, 1965), depending on the author. To the east, the Rhodope Massif disappears below the Thrace basin with its Eocene-Oligocene sedimentary cover (Gorur and Okay, 1996), additionally, directly overlying the structurally lower part of the Strandja Massif: the Strandja autochton (Jahn-Awe *et al.*, 2010).

The Rhodope Massif has classically been linked with the Alpine-Himalayan orogen (e.g. Meyer, 1968; Kronberg, 1969; Kronberg *et al.*, 1970; Dixon and Dimitriadis, 1984; Burg *et al.*, 1990). More recent research on the Rhodope massif has re-mapped the thrust contacts (Ivanov, 1988) and involved the investigation of syn-metamorphic structures (Burg *et al.*, 1990, 1996a,b). Currently, the Rhodope massif is regarded as a complex of syn-metamorphic nappes of Mesozoic age stacked in an Alpine active margin, possibly continuing in the Eocene (Jahn-Awe *et al.*, 2010; Froitzheim *et al.*, 2014). The Alpine active margin is thought to have undergone extension in the Cenozoic, exhuming high-grade rocks formed earlier.

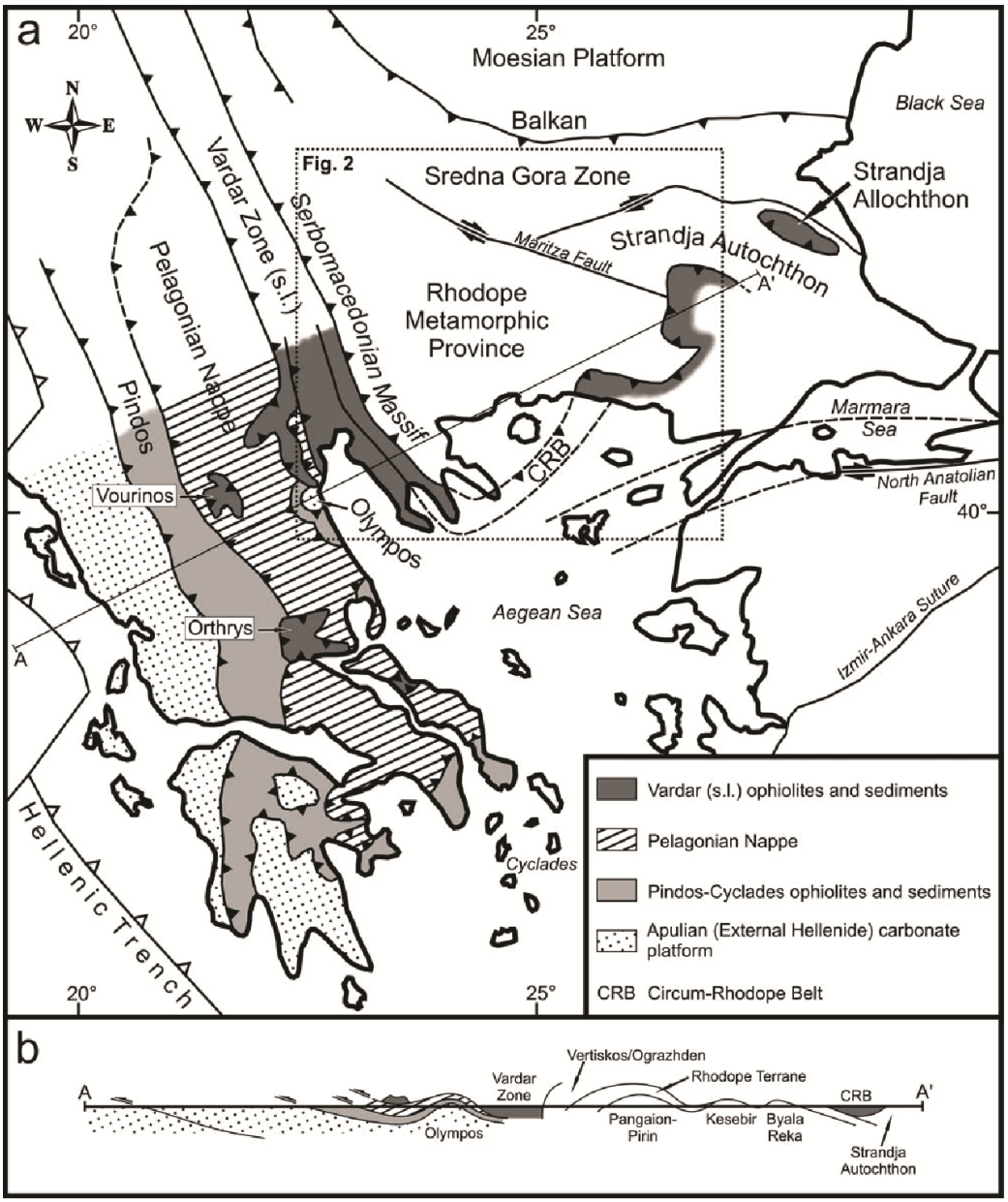

Figure 2 – a) The current Rhodope Complex configuration, additionally indicating its geological limits. In addition, the location of units bordering the Rhodope Complex can be derived from the figure. A number of these units will subsequently be discussed in section 2, in presenting the Rhodope Complex evolutionary stages. A-A' represents a transect, drawn through part of the Rhodopes and bordering units. b) Transect A-A'. The figure is from Jahn-Awe *et al.* (2010).

2.1 – Contractional evolution of the Rhodope massif

Several authors (e.g. Ricou *et al.*, 1998 & Jahn-Awe *et al.*, 2010) incorporated a summary of the Rhodope Mesozoic-Cenozoic formation history, involving its evolution merely as a consequence of contractional tectonics (figure 3 & 4).

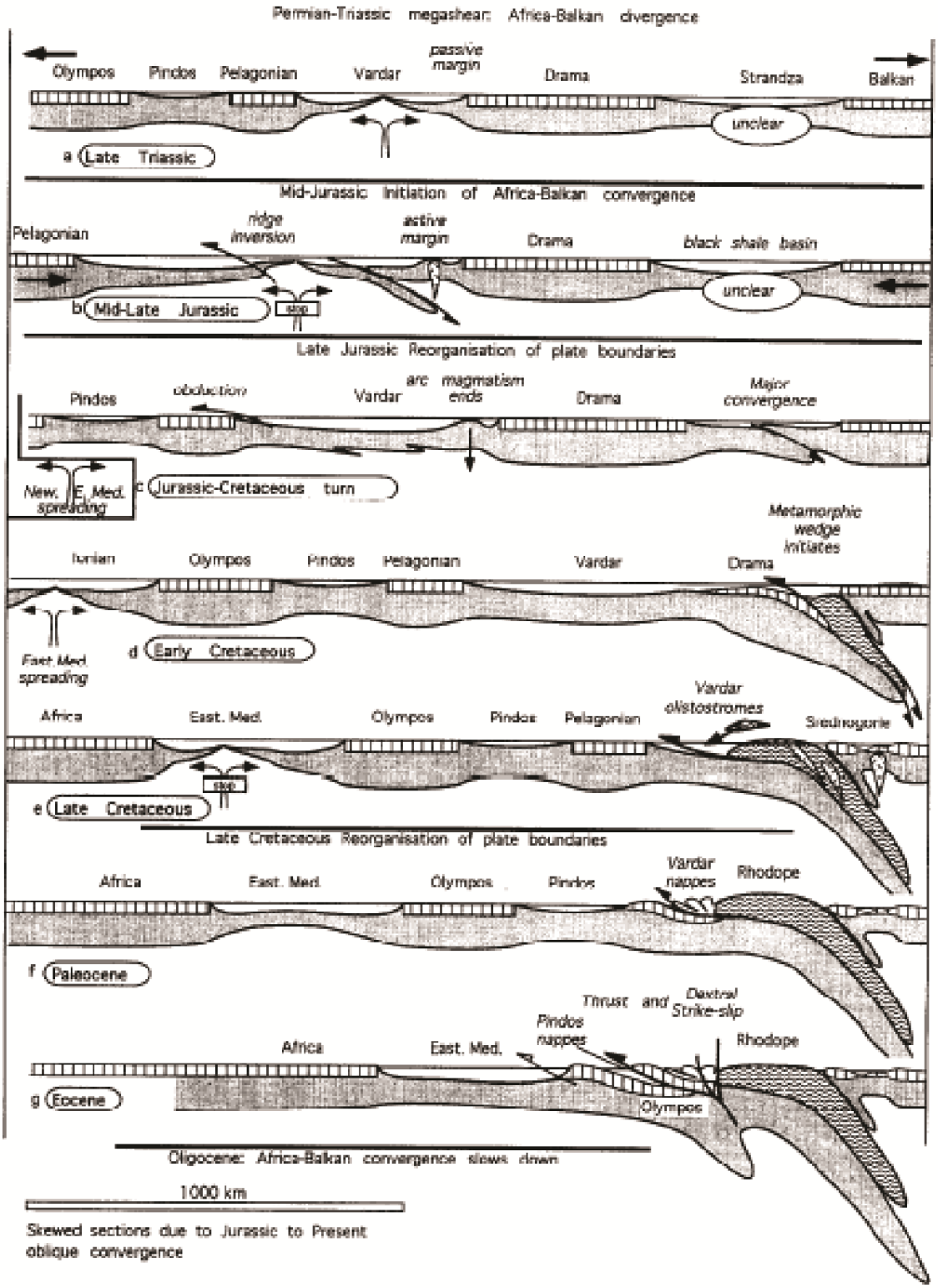

Figure 3 - The contractional evolution of the Rhodopian Mountains and their bordering units. After Ricou *et al.* (1998).

Figure 3a shows the initial configuration. The Pelagonian is located in the south-southwest and Moesia/Balkan (hereafter termed Balkan) in the north-northeast. A mid-oceanic rift exists at Vardar. The Vardar basin developed in the Mid-Triassic (Ricou *et al.*, 1998). Africa and Balkan drifted apart as a consequence of divergence in the Late Triassic.

Convergence between Africa and Balkan initiated in the period covered by Mid-Late Jurassic, as a consequence of the opening of the Central Atlantic. The mid-oceanic rift originally coincident with Neotethys ceases to exist (figure 3b) and the tectonic regime is inverted. The term Neotethys is introduced here to describe both Triassic and Jurassic oceanic crust.

New Eastern Mediterranean spreading occurs to the south of the configuration and a zone of major convergence is consequently developed in between Drama and Balkan (figure 3c).

Figure 3d shows that Eastern Mediterranean Spreading continued in the Early Cretaceous. The zone of major convergence developed earlier during the Jurassic-Cretaceous continues to evolve. In the Early Cretaceous configuration it is occupied by Drama, which is being subducted in that stage. It is thought that subduction of a significant quantity of the low-density continental fragment of Drama, reduced subduction velocity or even caused the temporary cessation of subduction. The metamorphic wedge represents the Rhodopes.

Ricou *et al.* (1998) argue that the opening of the Srednogorie volcanic arc in the Cenomanian (figure 3e) may reflect more readily executed subduction of the denser oceanic lithosphere underlying the Vardar basin, upon the migration of the subduction plane towards the southwest of Drama. The Vardar basin is progressively filled with olistostromic material during the Cretaceous, including pebble- to mountain-sized blocks. These were originally thought to have been derived from the Vardar basement, but are now reconsidered as originating from the Rhodope Metamorphic Complex. The olistostromic blocks vary in composition from serpentinite to marble, gneiss and amphibolite, in a volcano-detritic matrix, which would account for the presence of varied volcanic sources.

Cretaceous – Eocene shortening is recorded in the Carpatho-Balkanides orogen by S-ward subduction. Subduction is accompanied with northward thrusting (e.g. Jahn-Awe *et al.*, 2010). From Jahn-Awe *et al*. (2010) it can be implied that possibly a south-dipping subduction zone was present or backthrusting took place coincident with north dipping subduction. Ricou *et al.* (1998) do not incorporate northward thrusting and therefore implications similar to those proposed by Jahn-Awe *et al*. (2010) are not evident from figure 3. For the purpose of this report, northward thrusting is incorporated in figure 4. This figure does not show northward thrusting in

a tectono-evolutionary framework, but rather shows the results of northward thrusting. The position of transect A-A' is shown in figure 2.

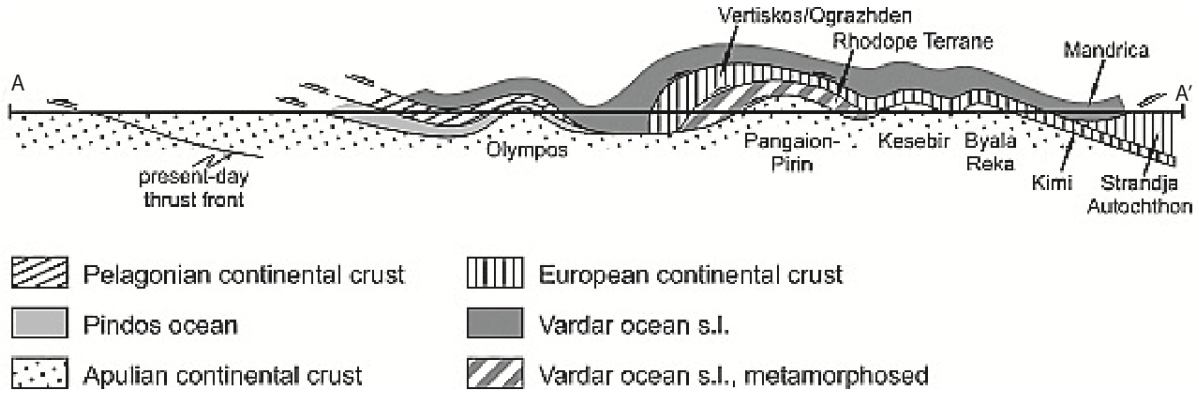

Figure 4 – Cross-section of the Rhodope Massif and its bordering units, illustrating thrusting. From Jahn-Awe *et al.* (2010). The geological map with which this cross-section is associated can be obtained from Jahn-Awe *et al.* (2010), figure 2.

Figure 4 incorporates northward thrusting in the Carpatho-Balkanides and illustrates the principles and constituents of the interpreted tectonic model for the Rhodope evolution of Jahn-Awe *et al.* (2010).

Southwestward migration of the subduction plane in the Senonian provided thrusting upon the Pelagonian (figure 3e-g). Afterwards, the position of subduction was transferred further southwest, to its current position, at the Hellenic trench (Ricou *et al.*, 1998). Reversal of subduction polarity (Jahn-Awe *et al.*, 2010) is implied by obduction of the Vardar nappes, south-southwestward onto the partly subducted Pelagonian (figure 3f). This shift in subduction polarity is accompanied by the formation of NE-dipping thrusts, forming a crustal-scale duplex (Wutrich, 2009) and is inferred from the fact that Europe-derived rocks (Vertiskos-Ograzhden in figure 4) are both overlain and underlain by ophiolite-bearing units derived from Vardar (Jahn-Awe *et al.*, 2010). The accompanied stage of deformation led to high-pressure (HP) regional metamorphism (e.g. Burg *et al.*, 1996a; Liati *et al.*, 2004) and even ultra-high-pressure metamorphism, locally (e.g. Mposkos and Kostopoulos, 2001; Perraki *et al.*, 2006).

New uplift and magmatism in the Rhodope initiated in the Eocene. This uplift has most likely been accompanied with the final release of the low-density, continental root of the Rhodope (Ricou *et al.*, 1998). This concept is further discussed in section 2.2.1 (Syn-orogenic extension).

2.2 – Extensional evolution of the Rhodope

Cenozoic extension resulted in the formation of core complexes, exhuming the high-grade rocks buried earlier during the Mesozoic shortening (Ivanov, 1988; Burg *et al.*, 1990, 1996b). The evolution of the Rhodope Massif is strongly linked with the relatively rapid extensional history of the Aegean region (Wutrich, 2009). Extension in the Aegean region commenced in the Rhodope Massif and migrated southward (Brun & Facenna, 2008).

Two possible, sequentially operating events have been suggested for Cenozoic extension, namely syn-orogenic, or syn-thickening extension, and post-orogenic, slab-rollback driven extension (e.g. Brun and Facenna, 2008).

Syn-orogenic extension is likely to have happened in a fore-arc setting and is thought to have been accompanied with little or no overall horizontal stretching of the crust or lithosphere (Wutrich, 2009 and references therein). Post-orogenic extension is ascribed to whole-lithosphere stretching, in addition, involving large detachments (Lister *et al.*, 1984; Gautier *et al.*, 1993; Jolivet *et al.*, 1994; Avigad *et al.*, 1997; Zeffren *et al.*, 2005; Brichau *et al.*, 2007).

2.2.1 – Syn-orogenic extension

Initial Rhodopian extension coincides with the Aegean setting represented by figure 3f. According to most authors, amongst others Kounov *et al.*, 2004 however, syn-orogenic etension started only in the Eocene. Syn-orogenic extension is thought to have been associated with the effect of extrusion wedges or the influence of a subduction channel (e.g. Schmädicke and Will, 2003; Ring et al, 2007b,a). It is assumed by Brun & Facenna (2008) that syn-orogenic extension is coeval with ongoing subduction and initiated as a continental block (Pelagonian) was accreted, following subduction of Vardar (Ricou *et al.*, 1998; van Hinsbergen *et al.*, 2005; Bonev *et al.*, 2006a).

2.2.2 – Post-orogenic extension

Obduction causes portions of previously subducted continental and oceanic crust to return towards the surface. As the mantle wedge becomes progressively opened during obduction of continental crust, asthenospheric material is able to flow into the opening mantle wedge. This causes the obducted continental material to be heated up and weakened, in the process (Chemenda *et al.*, 1995; see figure 5, step 2).

The heated and weakened, obducted continental crust is able to undergo a second (initial post-orogenic) stage of exhumation. Post-orogenic extension initiated at ~35 Ma (Forster & Lister,

2009). This exhumation stage is coeval with final closure of the Pindos oceanic basin and extension is related to core-complex formation in the Rhodope Massif (e.g. Brun & Sokoutis, 2007). Post-orogenic exhumation occurred at a lower rate than syn-orogenic extension and is associated with the formation of core complexes (Brun and Facenna, 2008). These core-complexes show rather uniform top-to-the-north to top-to-the-northeast senses of shear and are bounded by low-angle shear zones (Wutrich, 2009 and references therein). The southwestern Rhodope show dominantly top-to SW extensional shearing (e.g. Dinter & Royden, 1993; Burg *et al.*, 1990; Brun & Sokoutis, 2007; Georgiev *et al.*, 2010; Kroho & Mposkos, 2002).
From Wutrich (2009), it is apparent that alternative views exist on the extensional history of the Rhodope Massif. Forster & Lister (2009) argue that only whole lithosphere stretching has taken place, also during periods assigned to be syn-orogenic extension, above. They state that several events of accretion of individual continental fragments to subducted oceanic lithosphere bring about a sequence of push-pull-cycles affecting the Aegean lithosphere. Accretion of continental fragments in this case causes overall shortening, whereas subduction of an oceanic basin, taking place subsequently, brings about overall extension in the overriding plate.

3. Methods

3.1 - Fieldwork and field sampling

173 different locations have been described (see appendix 1.1 Maps and legends, figure 2).
S1 Foliation has regularly been measured infield, measuring dip-direction/dip of the fault plane. Whenever apparent, second generation (S2) foliation was measured in the same way.
Lineation was often recognized as stretching lineation, produced by stretching out clasts and analyzed by measuring azimuth and plunge of the lineation. Whenever apparent, second generation (L2) lineation was measured in the same way. In the presence of L2, L1 often appears to be crenulated with an angle between both generations of lineation, commonly ≤50°.
Infield shear sense indicators include shear bands, sigma and delta clasts (often of quartz and K-feldspar).
Occasionally, brittle faults have been analyzed measuring dip-direction/dip of the axial planes.
Folds were analyzed, measuring the azimuth and plunge of the fold axis.
These data have been assembled in stereographical projections, presented in section 4.1 (Infield results) of the Results.
Mineralogical observations and outcrop appearance provided first-order temperature estimations.

36 oriented samples have been collected from the fieldwork area.

The sample locations are indicated in figure 1, appendix 2. Appendix 2.1 provides an overview of the petrologic, microstructural and general structural geologic characteristics of the samples collected, sorted by lithotectonic unit and lithology.

3.2 - Optical Microscopy (OM)

Samples have been prepared for optical microscopy (OM).

Shear sense indicators determined by OM include shear bands, sigma clasts and mica fish.

Mineral content has been presented for the thin sections and it has been attempted to determine first-order apparent stable mineral assemblages.

Mineral stability or instability has been inferred on the basis of their appearance, shape and size, and the presence of mineral inclusions.

These characteristics have been used in order to provide estimations of metamorphic grade recorded by the samples.

All thin sections used for optical microscopy (and further study) have been assigned a specific section in appendix 2.1 (Thin section description), from which their general lithologic and petrologic characteristics can be derived.

The most revealing thin sections have been extensively described in further sections of this report, (on the basis of petrologic characteristics). Plan views of these thin sections have been assembled in appendix 2.2 (Optical Microscopy). Whenever possible, the location of sample-specific areas has been indicated on the plan views, which are more extensively described in further sections (amongst which the Results) of this report. Images of these sample-specific areas are obtained with the Leica® imaging system. As an example of this, reference is made to appendix 2.2 (Optical Microscopy), figure 1, showing the plan view of thin section 133, assembling the sample-specific areas, termed: 1, 2, 3 and 4. The numbers of these sample-specific areas are provided in the lower right corner of the sample-specific area images.

3.3 - Electron Microprobe analysis (EMPA)

Samples that have been deemed sufficiently qualified to be employed in further electron microprobe (EMP) study were carbon coated and prepared for utilization with the EMP.

The Electron Microprobe Analyzer (EMPA), version JEOL JXA-8230N, has been utilized at the Friedrich-Schiller-Universität Jena to obtain mass fractions of major element oxides and additionally, accessory element concentrations, characteristic for certain minerals. Major

element oxides measured include: SiO_2, Al_2O_3, FeO, MnO, MgO, CaO, Na_2O, TiO_2, Cr_2O_3, NiO, and K_2O. The EMP contains five wavelength dispersive spectrometers (WDS), an EDAX energy-dispersive spectrometer (EDS), standard operating conditions with acceleration voltage of 15 kV and a beam current of 15 nA. WDS has been carried out in order to provide high-resolution mineral chemical analyses.

Mineral instability was used as diagnostic for changing metamorphic conditions. Furthermore, chemically zoned minerals were traced and subsequently analyzed.

Spot analyses were carried out in order to obtain the character of chemical zonation and to infer prograde and retrograde metamorphism, coincident with mineral growth.

It has been inferred which minerals have grown coincident with prograde metamorphism and which minerals have grown coincident with retrograde metamorphism.

With the aid of the EMPA, it has become evident which samples record highest peak metamorphic conditions and which samples record retrograde and/or prograde metamorphic characteristics.

Excel tables have been made available to calculate relative components/fractions of a single solid solution of a certain mineral for garnet, white mica, feldspar, amphibole and biotite. These analyses have been incorporated in appendix 2.3.

The excel tables additionally correctly calculate Fe^{3+} element concentrations.

The EMP is capable of hosting three thin sections simultaneously. The total area covered by the three thin sections is represented by a system of coordinates, of which the 'x'-coordinate represents horizontal position and the 'y'-coordinate represents vertical position on the thin-section. The (0,0) position represents the center of the coordinate system, which corresponds to the upper third of the middle thin section in the sample holder. Minimum and maximum travelling distance for the sample holder corresponds to: Xmin (right) = -45.0000, Xmax (left) = 45.0000, Ymin (up) = -36.6443, Ymax (down) = 36.6443.

Image labeling and features

A considerable amount of figures have been obtained with the EMPA, serving mainly as indicators for WD spot analyses. Appendix 2.3, table 2 provides an overview of the approximate coordinates of the more specific smaller areas analyzed over the course of this report. Figures of these areas have further been assembled, partly in the report itself and partly in appendix 2.3. On occasion, in the report reference is made to these figures and, in specific, to individual spot analyses. Spot analyses are numbered. Appendix 2.3, table 1 represents the complete database

of EMP measurements/spot analyses. Whenever reference is made to an individual spot analysis or a set of spot analyses, the spot analysis number for a specific mineral is left in brackets. [13], e.g. represents spot analysis 13. [1-3] represents the range of spot analyses 1 to 3.

3.4 – PT calculations and winTWQ

Chemical analyses of assemblages of (chemically zoned) minerals serve as input for PT calculations. The garnet-biotite geothermometer and hornblende-plagioclase geothermometer (after Holland & Bundy, 1994) have been used initially to calculate PT conditions of mineral assemblages.

Subsequently thermodynamic modeling was done with winTWQ. winTWQ uses sets of geothermometers and geobarometers to calculate the position of phase equilibria in P-T space. Peak temperature, for the samples analyzed, is calculated from this.

4. Results

4.1 – Field results

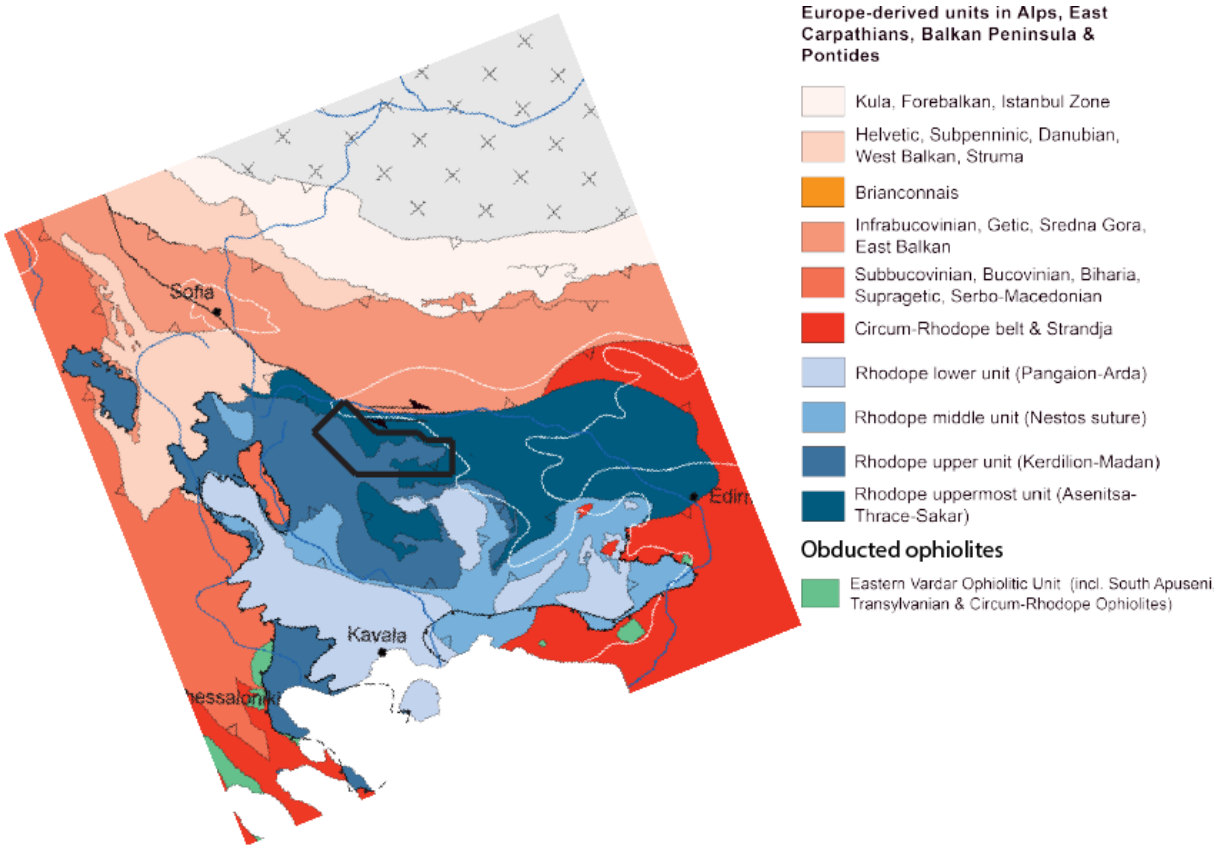

Figure 6 – Cropped-out portion of the map after Schmid *et al.* (2011), showing the tectonic units of the Alpine collision zone between eastern Alps and western Turkey. This cropped-out portion represents the Rhodope Massif, together with part of its bordering constituents. The legend provides the location of Rhodope Lower, Middle, Upper and Uppermost units, together with the constituents of those units (in brackets). In addition, the map shows the presence and location of thrust, normal and strike slip faults (or fault zones).

Structural characteristics

General features

Rocks possess very consistent foliation throughout the area of interest, although exceptions and inconsistency of foliation intensity within a single lithology exist.

(Stretching) lineation is not documented consistently and occasionally lineation is not very pervasive.

Rocks in the area of interest are commonly very competent and appear fractured and brecciated with exceptions of highly schistose biotite-epidote metagranites, amphibolites (of the Upper Unit), medium-grained marbles (of the Uppermost Unit).

Rocks in the area of interest are commonly affected by late-stage normal faulting. This is occasionally accompanied with the development of fault striations.

Folding is relatively consistent in the area of interest.

Mylonitization in biotite and amphibole-biotite gneiss and gneiss-schist at a contact with another lithotectonic unit implies the general presence of tectonic contacts.

Massive medium-grained marble of the Uppermost Unit records ancient cross-stratification in close vicinity with migmatized biotite and amphibole-biotite gneiss and marbles with graphite due to the strong lithologic contrast between both lithologies (personal communication Matenco).

Upper unit

D1

Top-±S sense of shear on ±S-dipping foliation planes in the Bachkovo-Dobralak unit (see figure 7) is occasionally recognized, in association with high grade rocks, mostly near by the boundary with the Asenitsa unit (fig. 21).

Flat-lying ±E-W folding with fold axes parallel to S-ward stretching lineation and axial planes parallel to ±SW-dipping foliation is characteristic for this deformation stage (see figure 8).

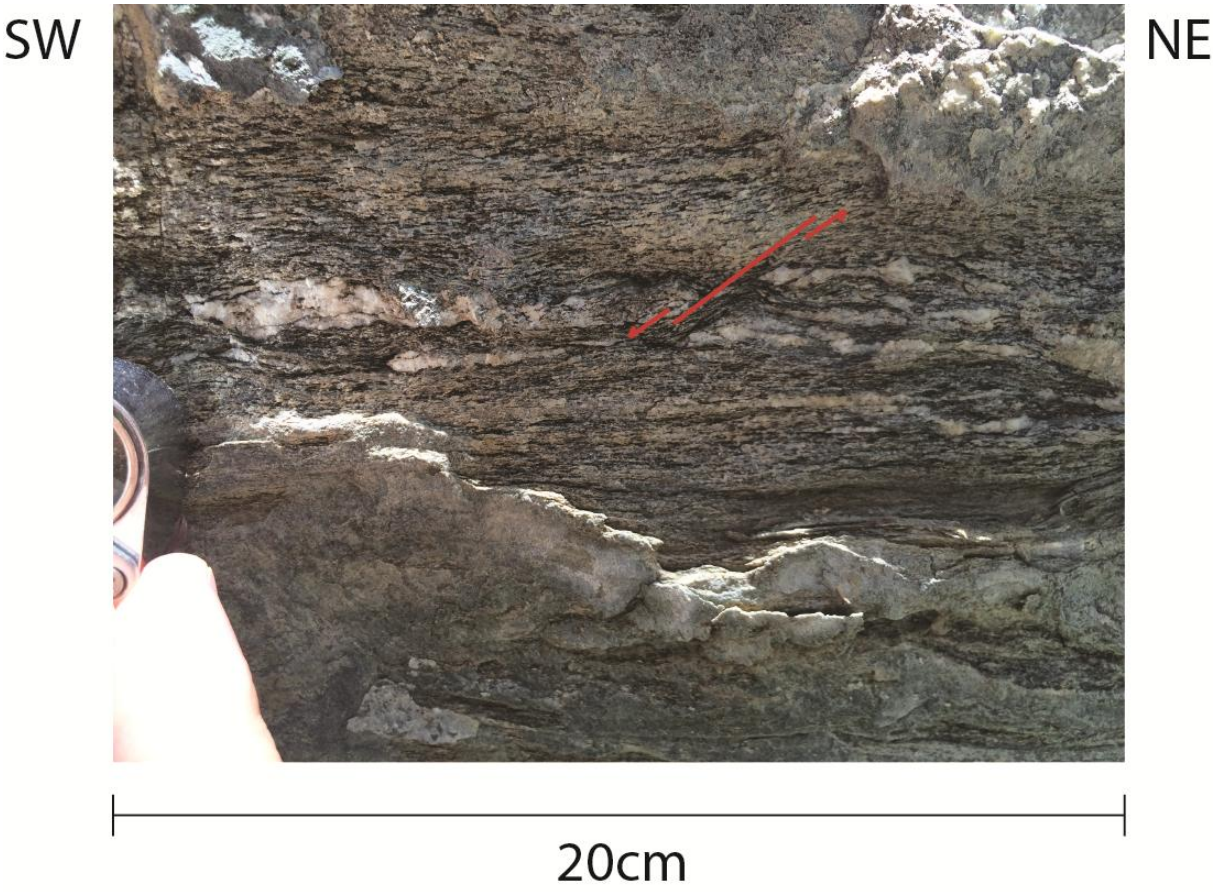

Figure 7 – An example of an interpreted shear band (in red) in ms+qtz-bearing gneiss, part of the muscovite metagranite lithology. Associated shear sense is towards SW (225) on a ±SE-dipping foliation plane (S: 135/30). Image coincides with placemark 107. See compass on the left for scale.

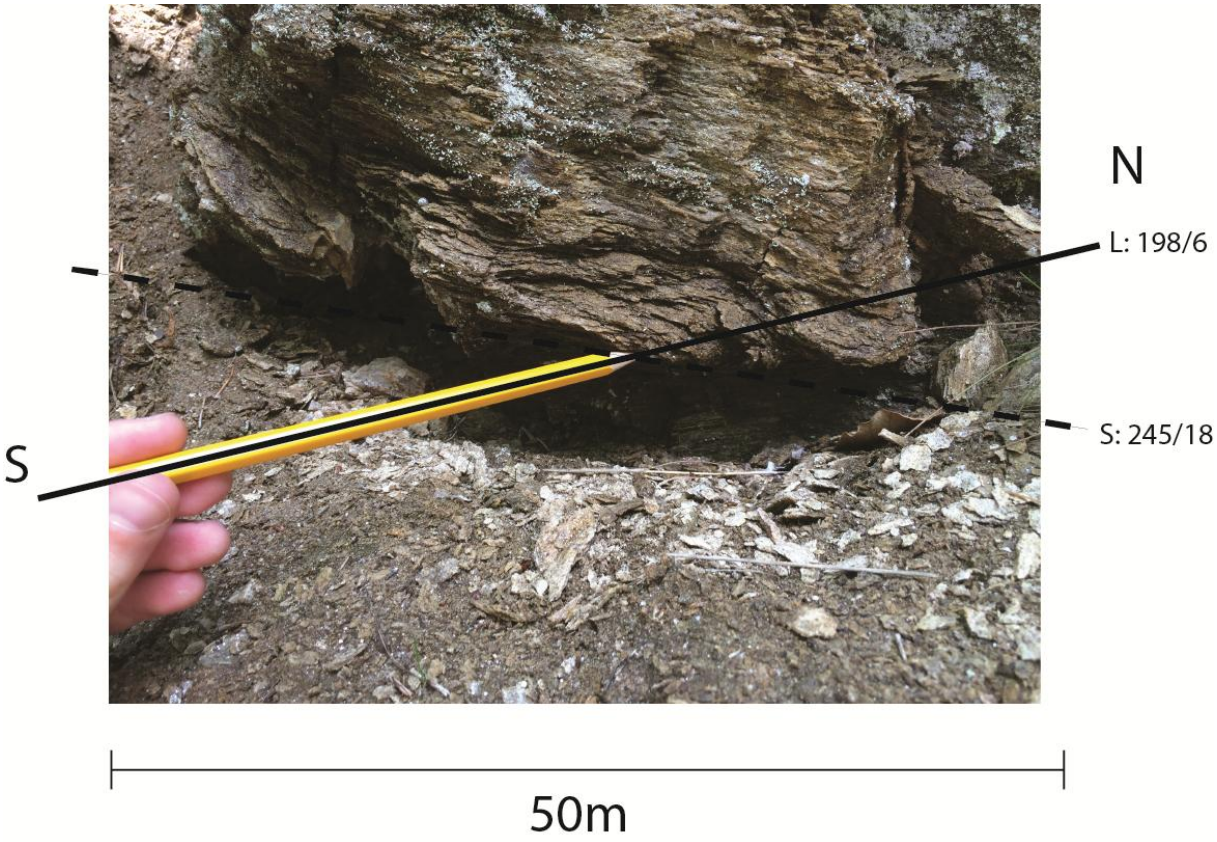

Figure 8 – An example of flat-lying ±E-W folding in muscovite metagranite. The image coincides with placemark 144. The axial plane of cm-scale folding is ±parallel to foliation (S: 245/18) and the fold axis (in the extension of the pencil) is ± parallel to stretching lineation (L: 198/6).

D2

Top -±S sense of shear on ±N-dipping foliation planes is occasionally recognized in the Bachkovo-Dobralak (e.g. placemarks 20, 142, see fig. 22). This deformation is however mainly recognized in the Madan and Chepinska units, which are outside the area of interest. For top-S shearing in occurrence with NE-dipping foliation, pervasive E-W folding exists, the axial planes of which are parallel to lineation. Migmatized rocks exist that cut right across folding. In other localities, it is evident that migmatisation is concomitant with folding, in which case migmatisation generally takes place in the axial planes of folds in which case it may be related to lineation. Also migmatisation that is both aligned with and cuts across W/NW-dipping foliation is observed.

NW-dipping foliation contains folds with horizontal axial planes that are parallel to foliation.

Baby granites are present, which intruded simultaneously with an extension event. The intrusion is of large dimension; it has almost completely replaced the amphibolite host rock.

Figure 9 shows an example of the coexistence of evidence for two distinct deformation phases characterized by S-dipping foliation which is crenulated by N-dipping foliation (described later), in the Bachkovo-Dobralak unit.

Figure 9 – An example of S-dipping (S1) foliation that is crenulated by N-dipping (S2: 05/12) foliation in a biotite-and-muscovite-rich mylonitic gneiss. Pencil and hammer for scale. Pervasive NW (313)-trending lineation (not seen in this image) is also observed. Image coincides with placemark 142.

D3

Top ±N sense of shear is recognized on ±S-dipping foliation planes (see fig. 10) in low grade rocks from the Bachkovo-Dobralak unit. Often, the trend of lineation is parallel to the strike of foliation (see fig. 23-25, purple shear senses).

±S-dipping foliation planes have cm-scale felsic folds with axial planes ±parallel to the ±S-dipping foliation (see figure 11).

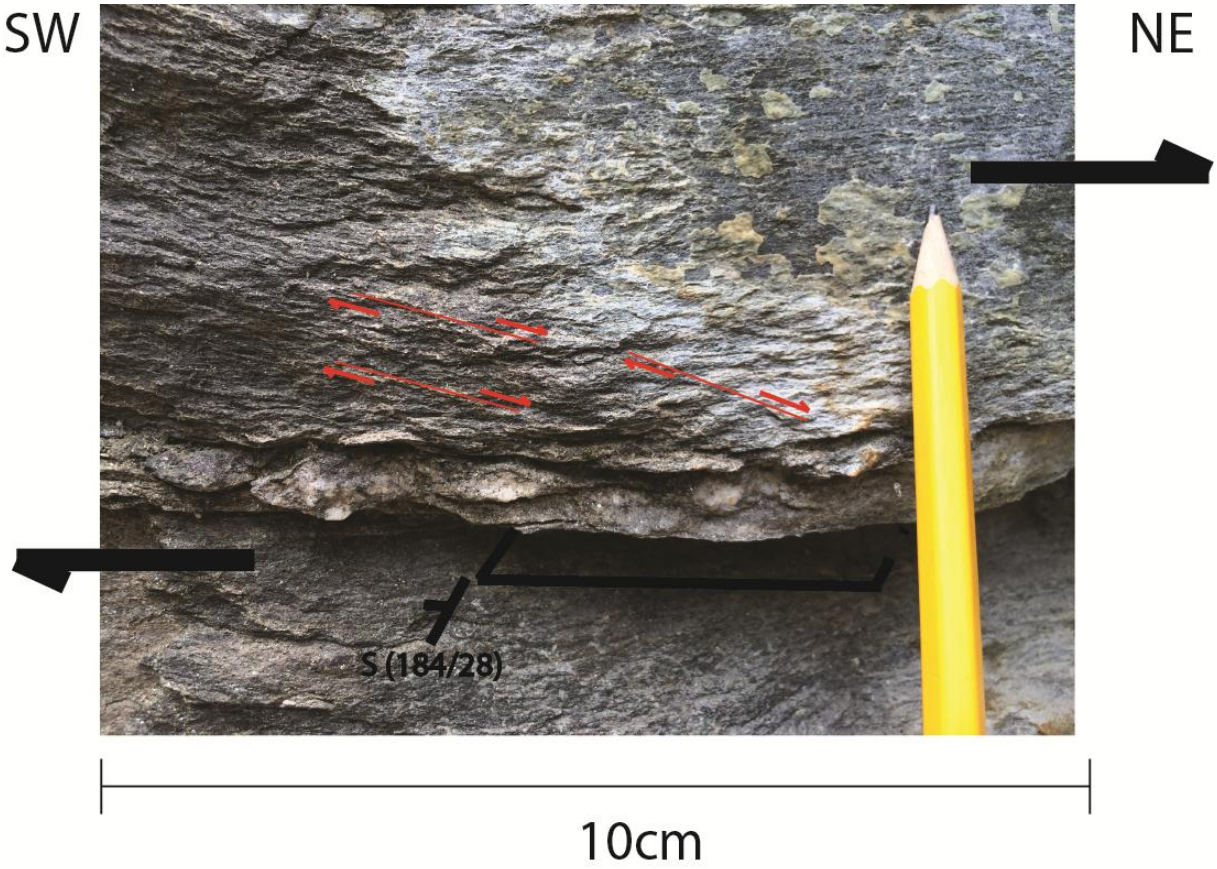

Figure 10 – An example of top-±N sense of shear on a ±S-dipping foliation plane in the Bachkovo-Dobralak. Top-NE (60) sense of shear (black arrows) is evidenced by dm-scale shear bands (indicated in red) with 240/16 lineation. Rock is ms-containing amphibolite-schist. Image coincides with placemark 86. Pencil for scale.

Figure 11 – From the same locality as figure 10 (placemark 86). Rock is a ms-containing amphibolite-schist. Folded felsic material follows the ±E(SE)-dipping foliation, with the axial plane being ± parallel to the foliation, and has thus intruded prior to or concomitant with this deformation. The rocks are affected by ±E-directed normal faulting. Pencil for scale.

Top-±W/NW-N (fig. 12) and top-±E/NE-N sense of shear on ±N-dipping foliation planes are combined for description purposes (see figure 23-25, orange and red shear senses), but it is thought that both transport directions comprise a different stage of deformation, as will be discussed.

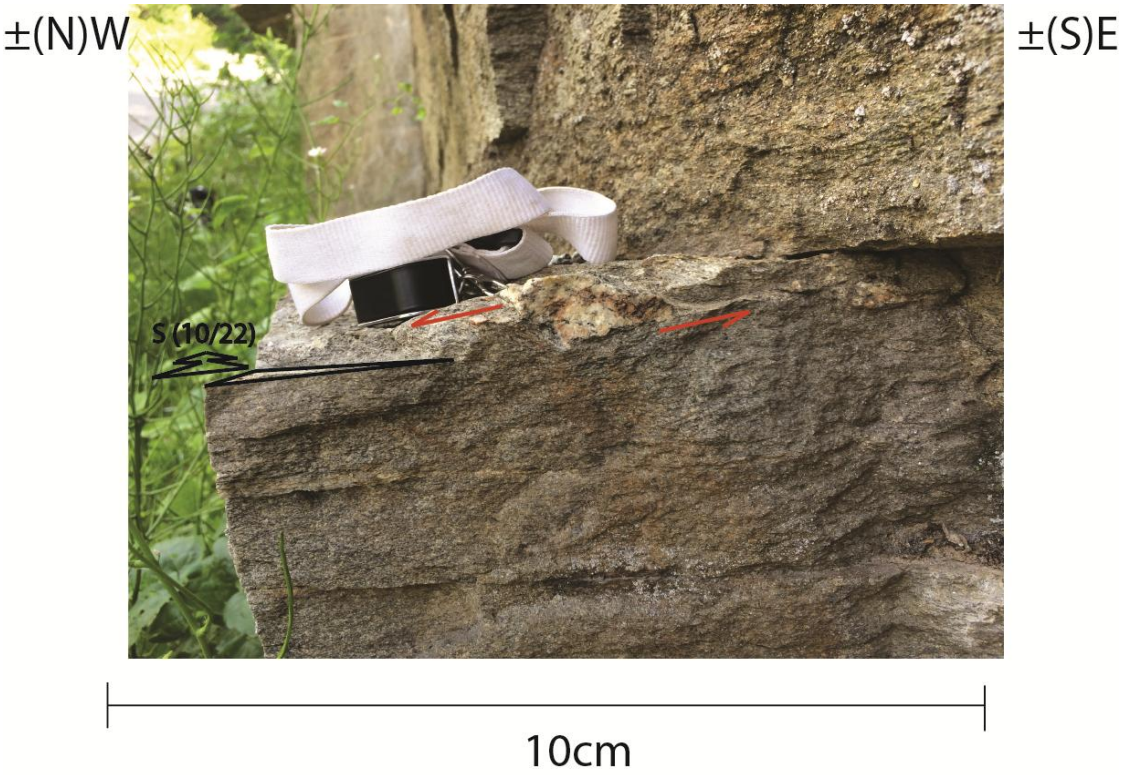

Figure 12 – An example of N(E)-dipping foliation in association with top-(N)W (298) shear sense (in red), as evidenced by a cm-scale sigma clast. The rock is a qtz-containing 2-mica gneiss. The image coincides with placemark 63. Lens for scale.

Top-±E/NE-N sense of shear on ±N-dipping foliation planes is recognized (see figures 13, 15 & 16). Occasionally, this deformation stage is associated with isoclinal folds, the axial planes of which coincide with the trend of stretching lineation. These are often collapse folds, developed as a consequence of extension. The hinge zones of the collapse folds may consist of felsic material or evidence of top-NE sigma clasts (see figures 15 & 16).

The transition of two different tectonic regimes may be inferred from the structural characteristics of the outcrop shown in fig. 13 and 14: from ±S-dipping foliation with top-±S sense of shear to ±N-dipping foliation with top-±N sense of shear, defined by tilted or crenulated original S(W)-dipping foliation, currently dipping towards N(E). It is assumed that the original shear sense associated with ±S-dipping foliation is overprinted largely by top-±E/NE-N sense of shear.

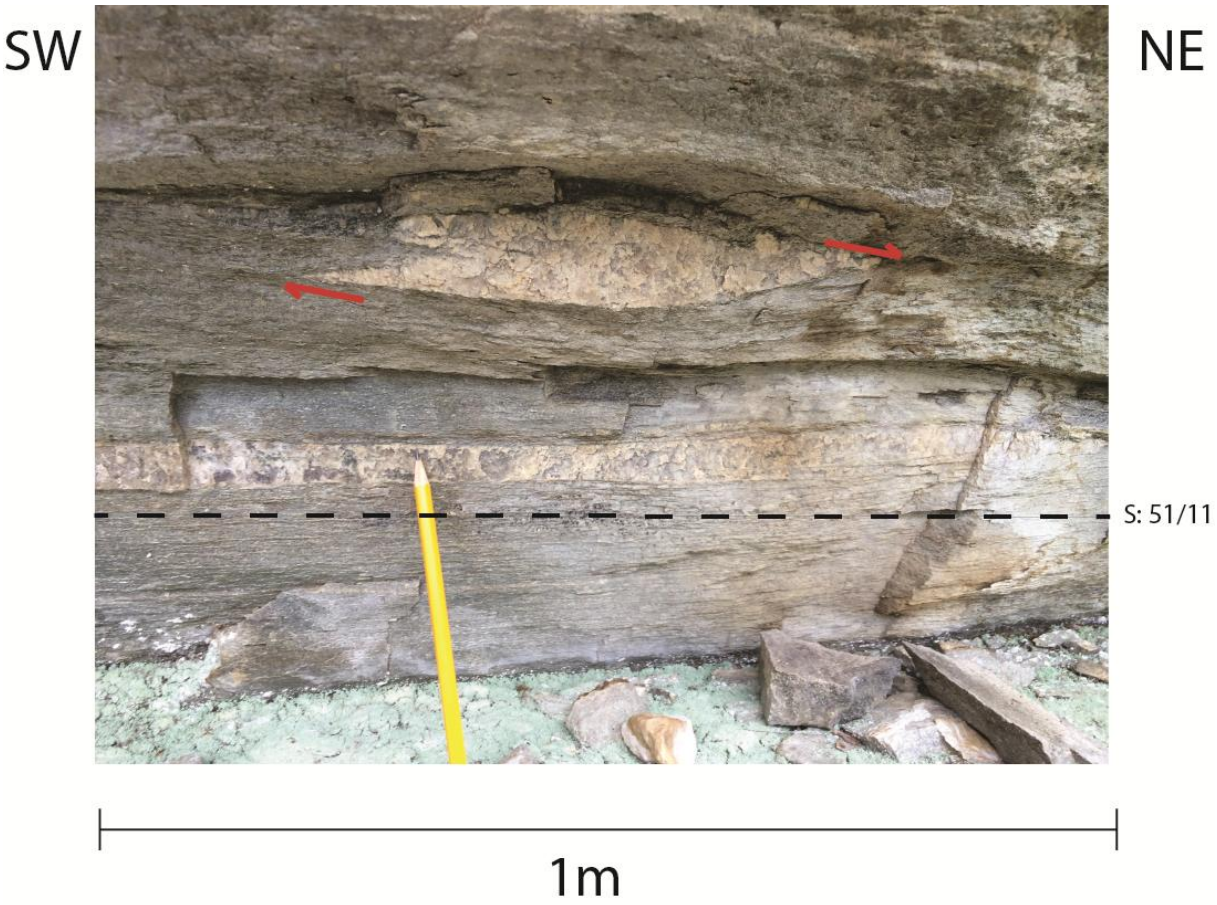

Figure 13 – An example of top-NE (60) sense of shear (red arrows) on a NE-dipping foliation (S: 51/11) plane. The figure is from the same locality as figure 14. Top-NE sense of shear is evidenced by a relatively large (m-scale) sigma clast with well-defined lineations (L: 60/11). The rock is a bt+ms+chl-bearing gneiss, part of the biotite-epidote metagranite lithology. Pencil for scale.

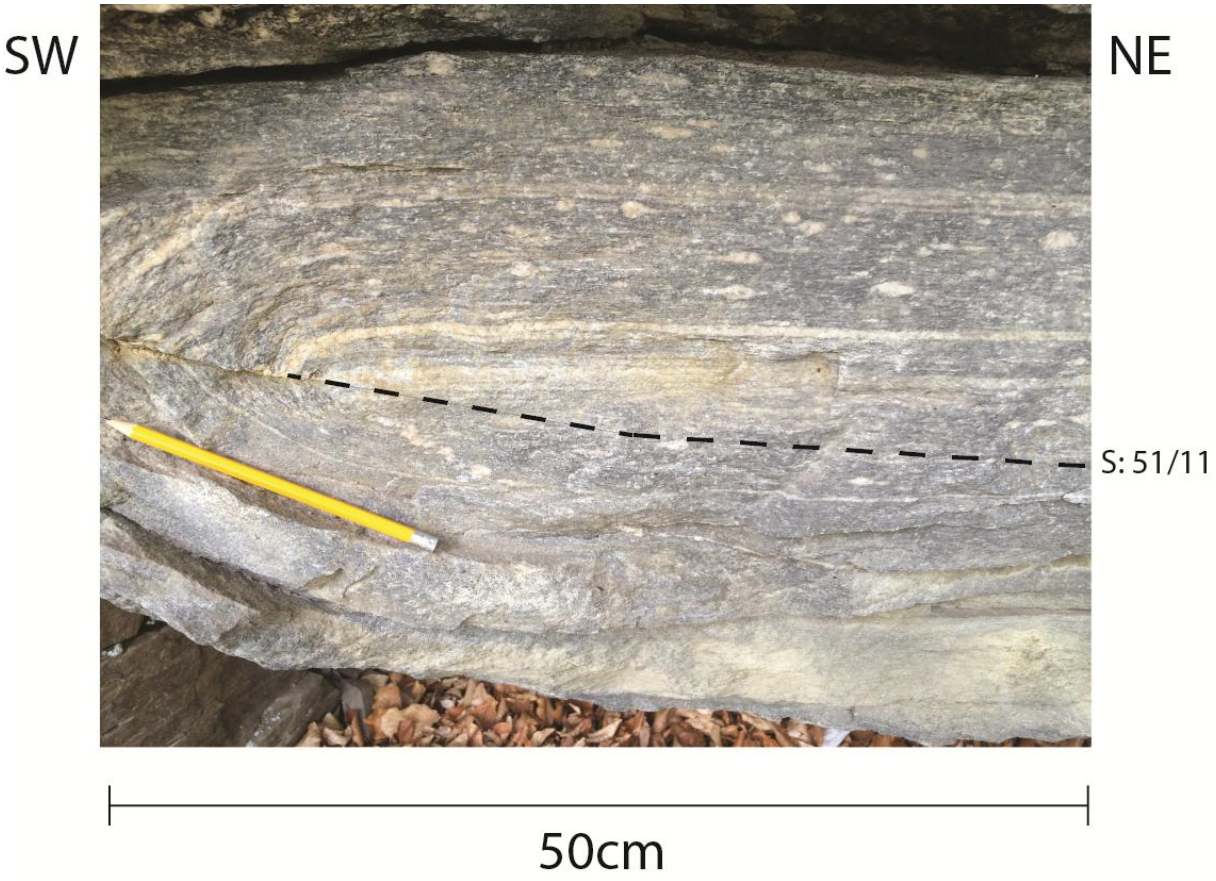

Figure 14 – An example of recumbent, dm-scale horizontal folding in a bt+ms+chl-bearing gneiss. The axial plane indicated is parallel to the foliation. Felsic material is caught up in folding. An example of a refolded felsic vein is present slightly upper right from the pencil. ±Symmetric sigma clasts present within the fold hinge zones follow the observed folding. The refolded felsic material and sigma clasts are interpreted to originate from an earlier deformation event, predating recumbent folding. The image coincides with placemark 114. Pencil for scale.

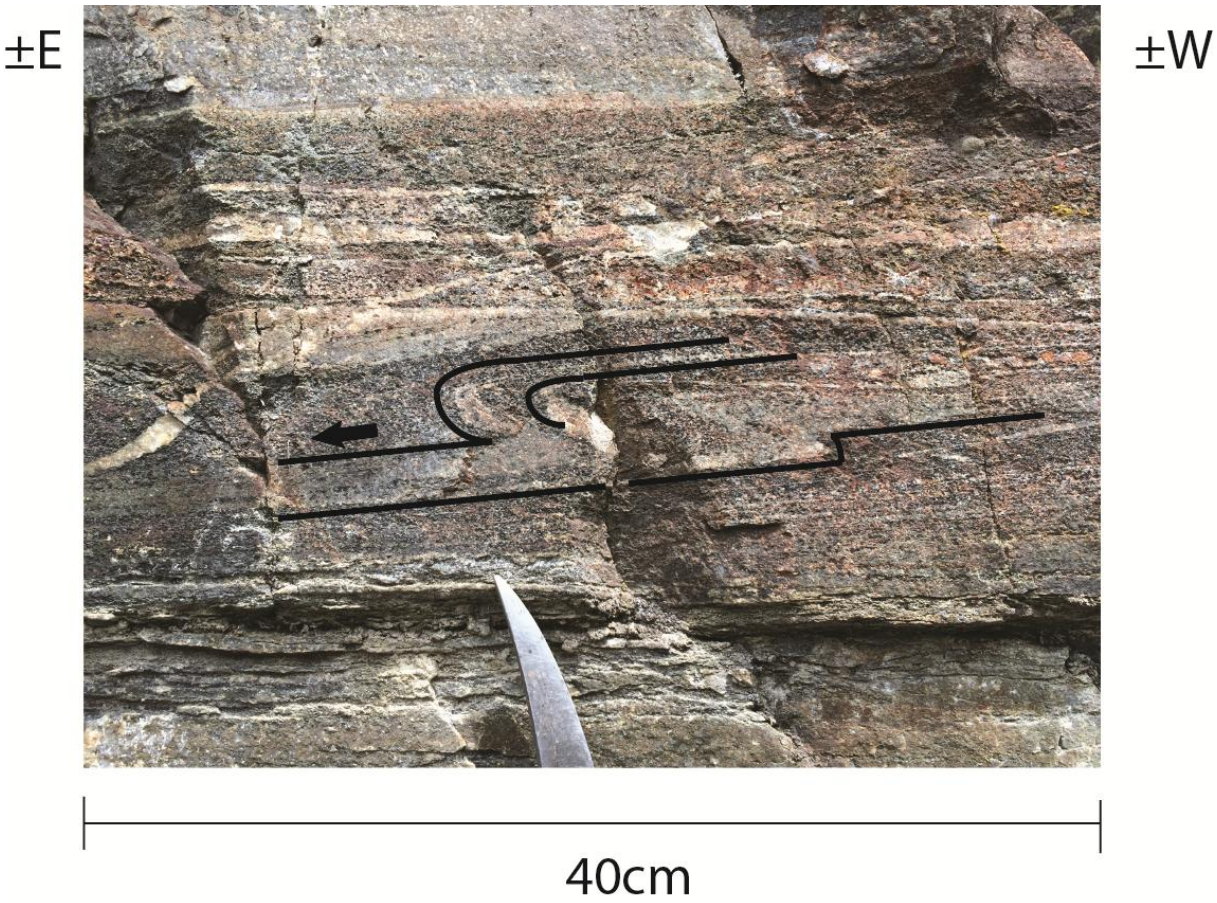

Figure 15 – An example of dm-scale collapse folds indicating ±E-ward (top 70; measured nearby) extension. The hinge zones consist of felsic material, occupying space left. Furthermore, 2 different generations of felsic intrusion exist: (1) an older one, which follows foliation (S: 147/47; measured nearby) and folding and (2) a more recent intrusion, cross-cutting the pervasive foliation. The rock is a gt-ms-qtz-bt-containing paragneiss, part of the muscovite metagranite lithology of the Upper unit. Image coincides with placemark 59. See hammer for scale.

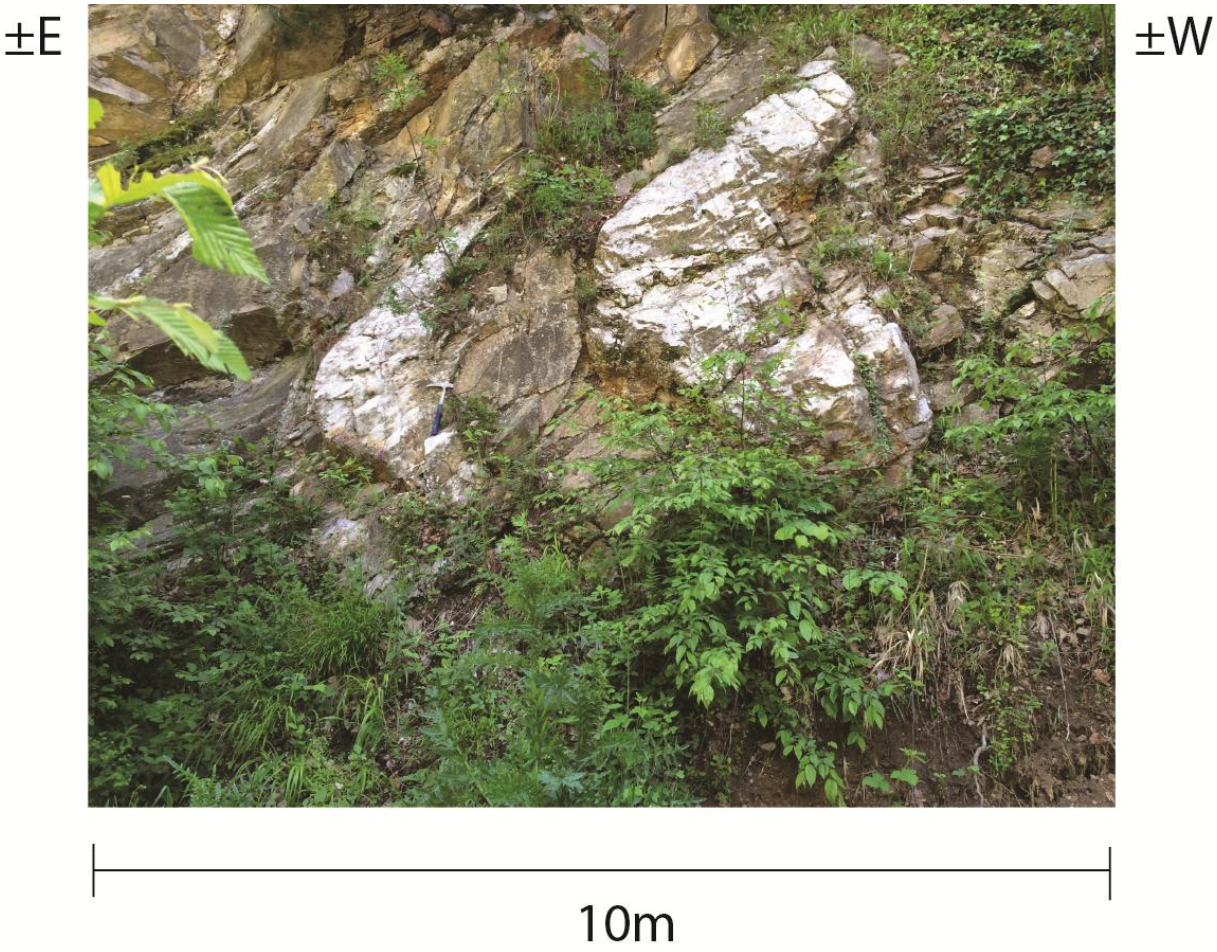

Figure 16 – An example of m-scale collapse folds indicating ±E-ward extension. The hinge zones consist of felsic material, occupying space left. The rock is a gt-ms-qtz-bt-containing paragneiss, part of the muscovite metagranite lithology of the Upper unit. Image coincides with placemark 59, with similar measurements as in figure 12. See hammer for scale.

Uppermost Unit

D1

Top-±N sense of shear on ±S-dipping foliation planes in the Asenitsa unit (e.g. placemark 36 and 56, see fig. 21), is occasionally recognized, in association with high grade rocks.

D2

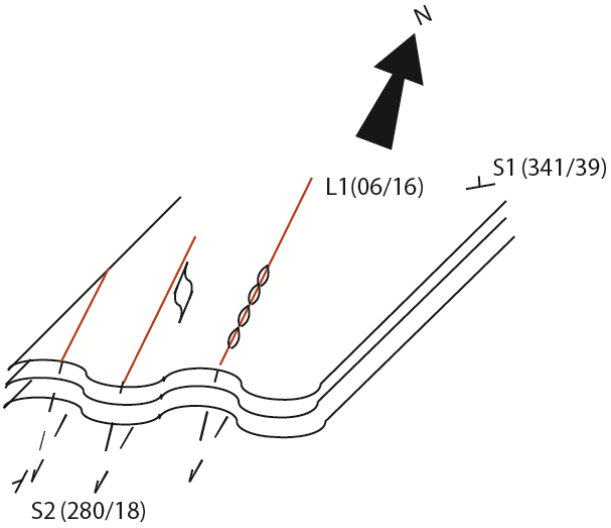

Figure 17 - ±NW dipping foliation (S1) has N-plunging stretching lineations in association with boudins. This is likely diagnostic for ±N-ward extension. S1 is crenulated by ±W dipping foliation (S2), defined by E-W folding.

Fold axes of certain folds often appear to plunge in a direction similar to N-plunging lineation associated with ±NW-dipping foliation observed. N-plunging lineation is in association with boudins in a direction parallel to the pervasive stretching lineation (see fig. 17). This is likely associated with ±N-ward extension. ±N extension is identified in association with quartz which is not dynamically recrystallized, diagnostic for low temperature (as is the case for sample 16, see appendix 2.1). ±N extension is identified in association with Kfs clasts that have not been smeared out, evidencing low-temperature conditions.

D3

Throughout the entire Asenitsa unit, often top-E/NE sense of shear is recognized on ±N-dipping foliation planes (see fig. 23-25, red shear senses).

Top-±S sense of shear on ±S-dipping foliation planes in the Asenitsa unit is recognized e.g. at placemarks 13 and 23 (see fig. 23-25, purple shear senses).

Low temperature SW-dipping shear bands are identified in association with N-S-trending lineation in the Asenitsa unit. These are potentially related to top-±S exhumation.

NE-SW trending intersection lineation, crenulating lineation with top-N sense of shear, may imply a shift in tectonic regime from ±N thrusting to SW extension.

Figure 18 shows a Schmidt net distinguishing between foliations for the Bachkovo-Dobralak and Asenitsa lithotectonic units. Figure 19 shows a Schmidt net distinguishing between trend of (stretching) lineations for the Bachkovo-Dobralak and Asenitsa lithotectonic units. Figure 20 shows a Schmidt net distinguishing between shear sense for the Bachkovo-Dobralak and Asenitsa lithotectonic units. In particular, combining the Schmidt nets in figures 18 and 20, the deformation phases discussed above can be recognized. Figure 21-25 shows the area of this study, incorporating the combinations of shear senses and foliations.

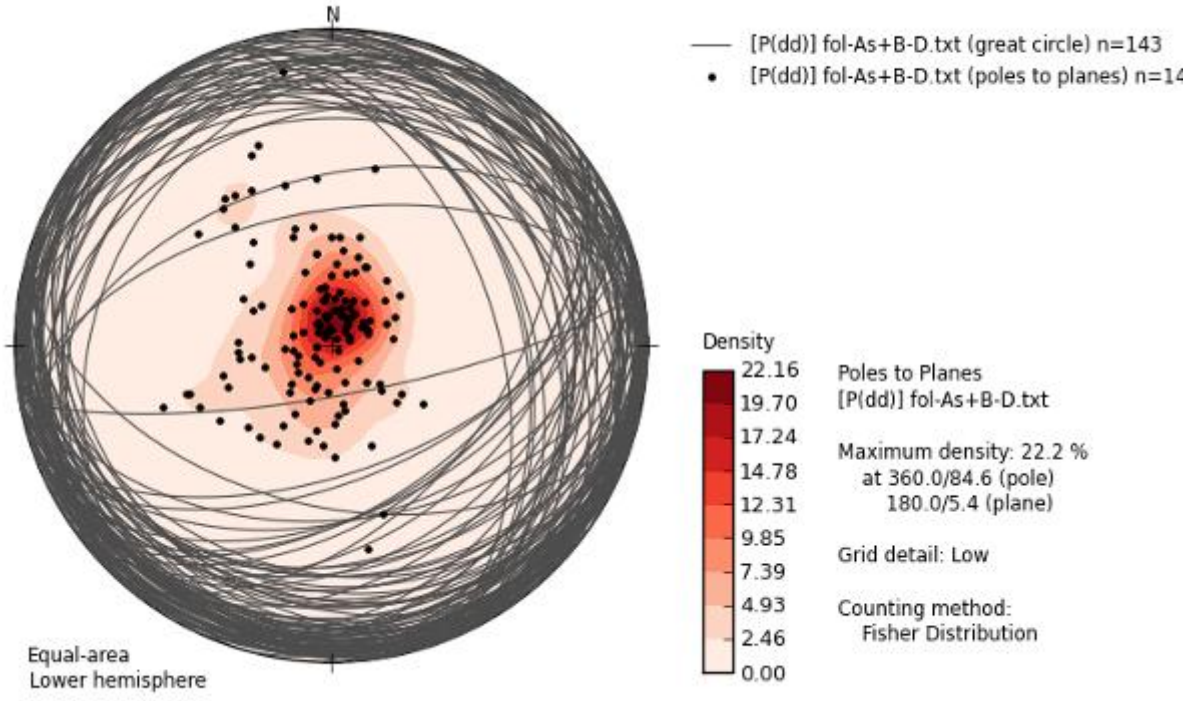

Figure 18 – Schmidt net distinguishing between foliations for the Bachkovo-Dobralak and Asenitsa lithotectonic units (see appendix 1.2, table 1).

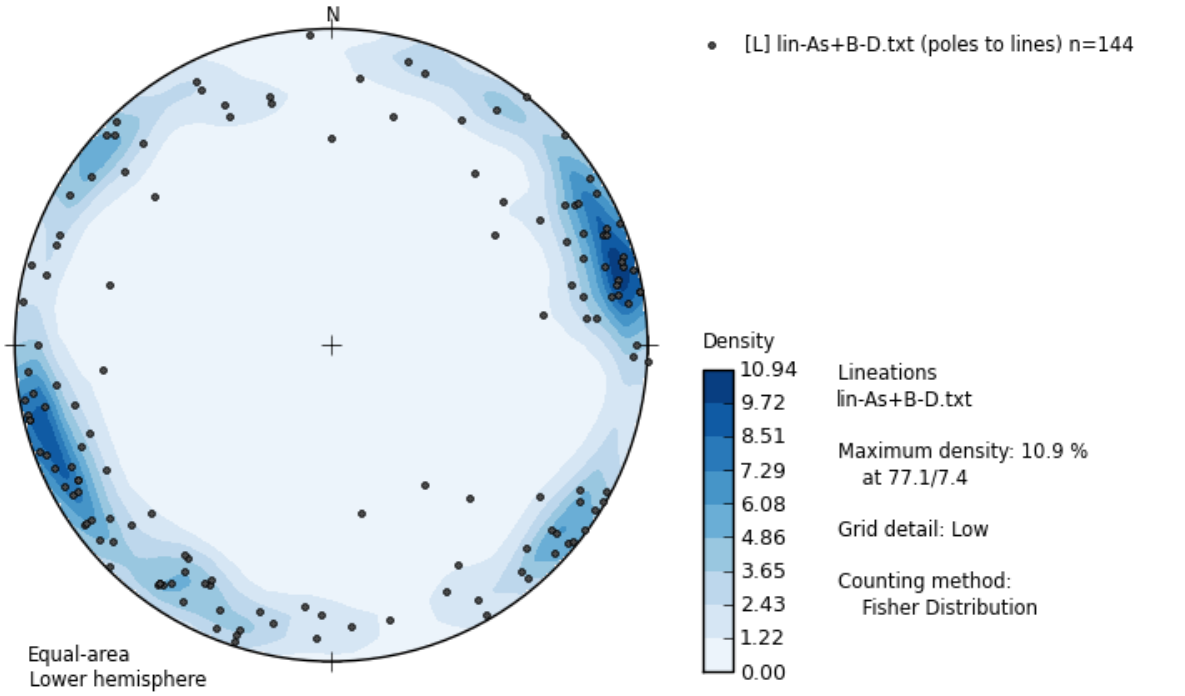

Figure 19 – Schmidt net distinguishing between trend of (stretching) lineations for the Bachkovo-Dobralak and Asenitsa lithotectonic units. Earlier generations of lineations are mostly associated with a trend towards ±NW, ±NE and ±S-SE. L2 is mostly associated with a trend plunging towards ±NE (see appendix 1.2, table 2).

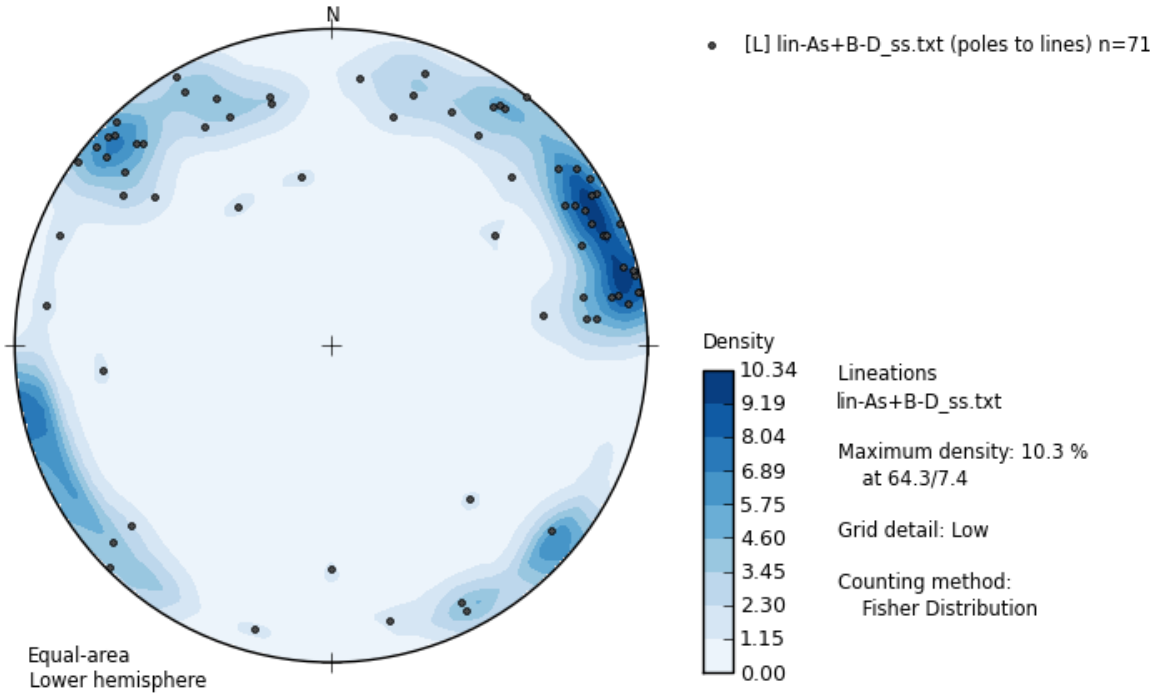

Figure 20 - Schmidt net distinguishing between shear sense for the Bachkovo-Dobralak and Asenitsa lithotectonic units (see appendix 1.2, table 2).

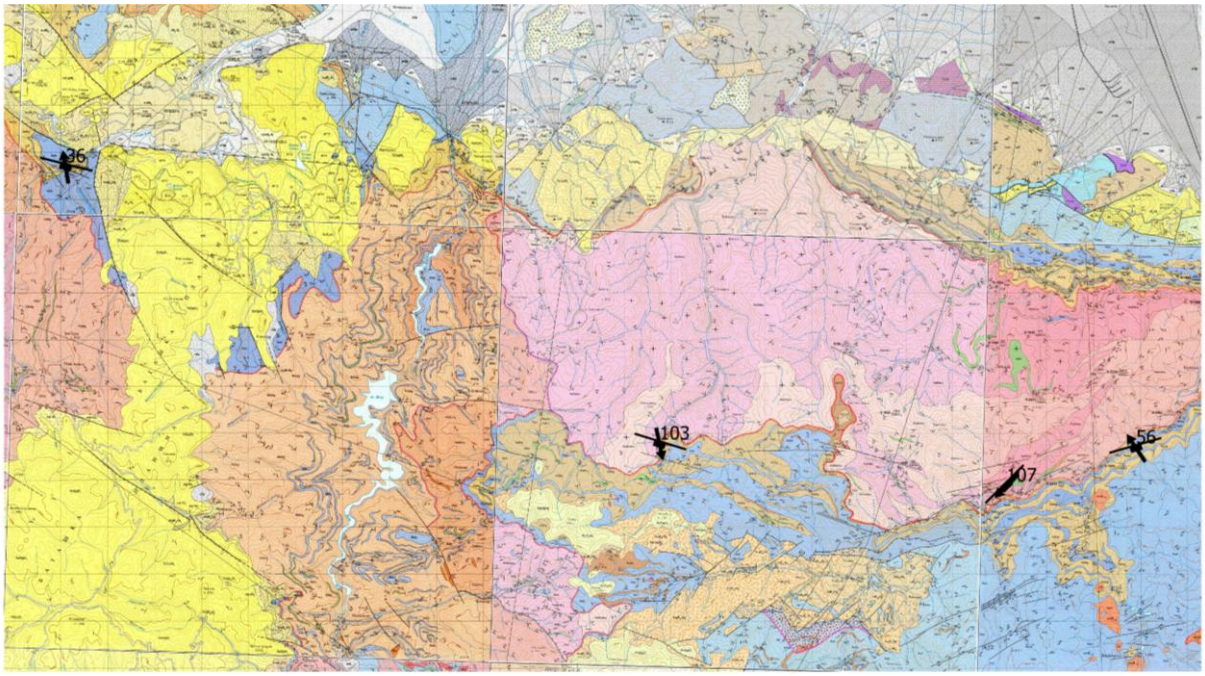

Figure 21 - The fieldwork area of this study, showing the Upper Unit and Uppermost Unit, after Bulgarian geological map sheets and Schmid *et al.* (2013) and D1 foliation planes and shear senses (arrows). The data is obtained from fieldwork and optical microscopy. The labels represent placemark numbers.

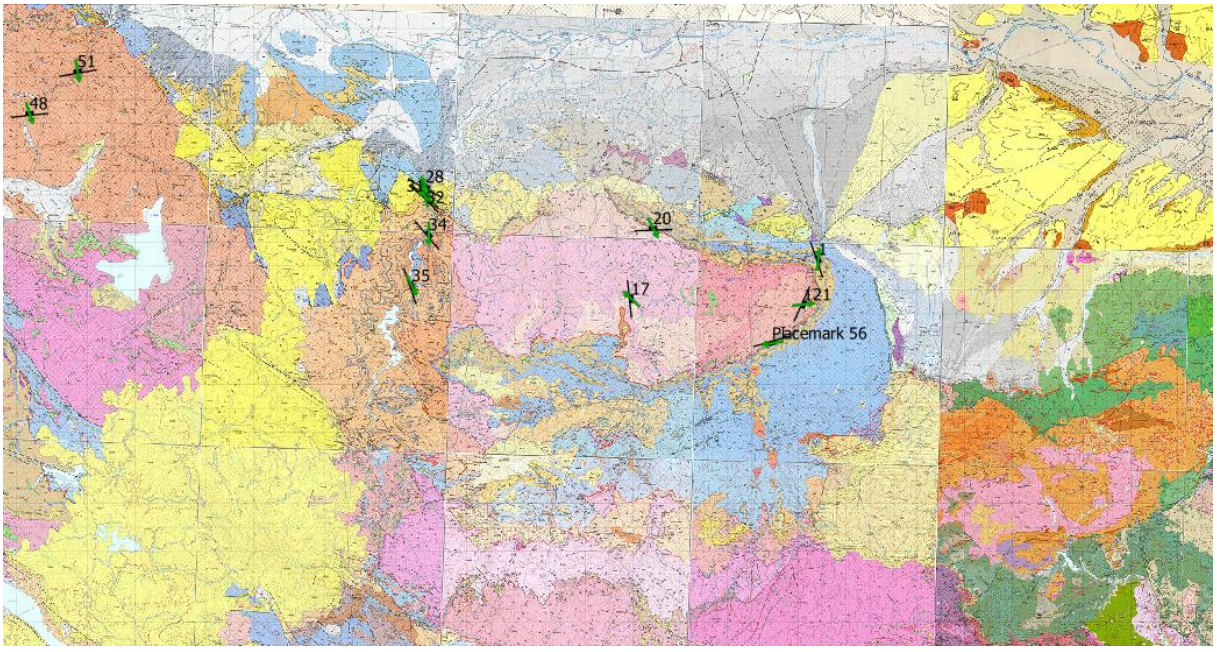

Figure 22 - The fieldwork area of this study, showing the Upper Unit and Uppermost Unit, after Bulgarian geological map sheets and Schmid *et al.* (2013) and D2 foliation planes and shear senses (arrows). The data is obtained from fieldwork and optical microscopy. The labels represent placemark numbers.

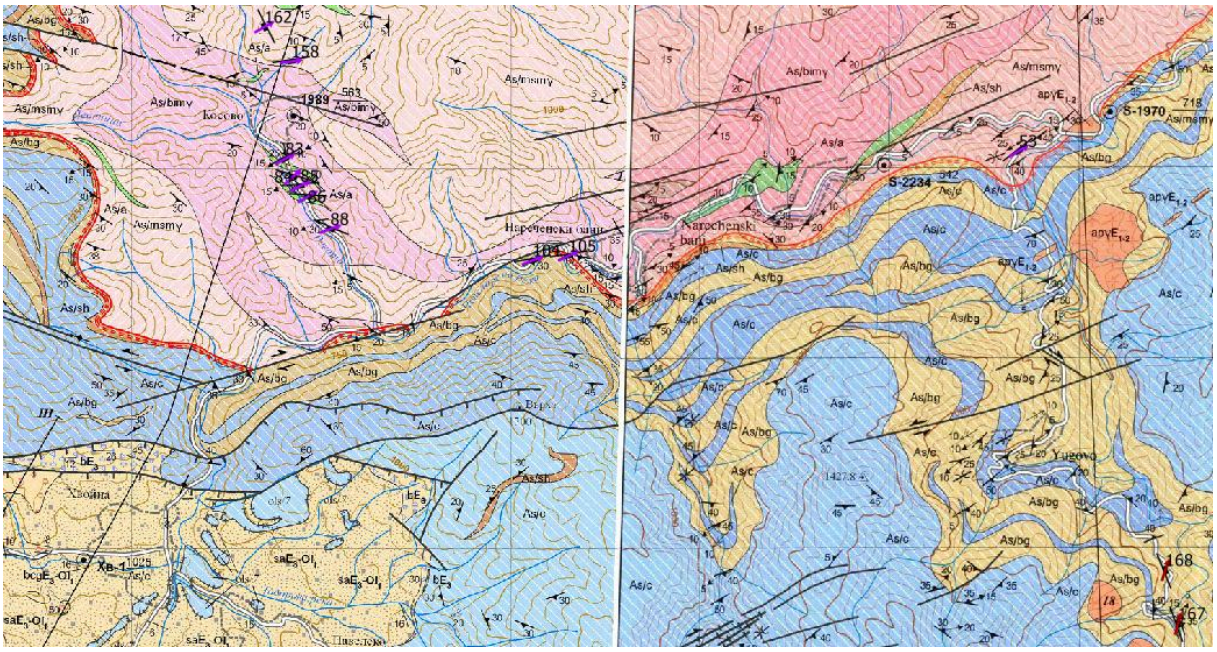

Figure 23 – Part of the fieldwork area of this study, showing the Upper Unit and Uppermost Unit, after Bulgarian geological map sheets and Schmid *et al.* (2013) and D3 foliation planes and shear senses (arrows). The data is obtained from fieldwork and optical microscopy. The labels represent placemark numbers.

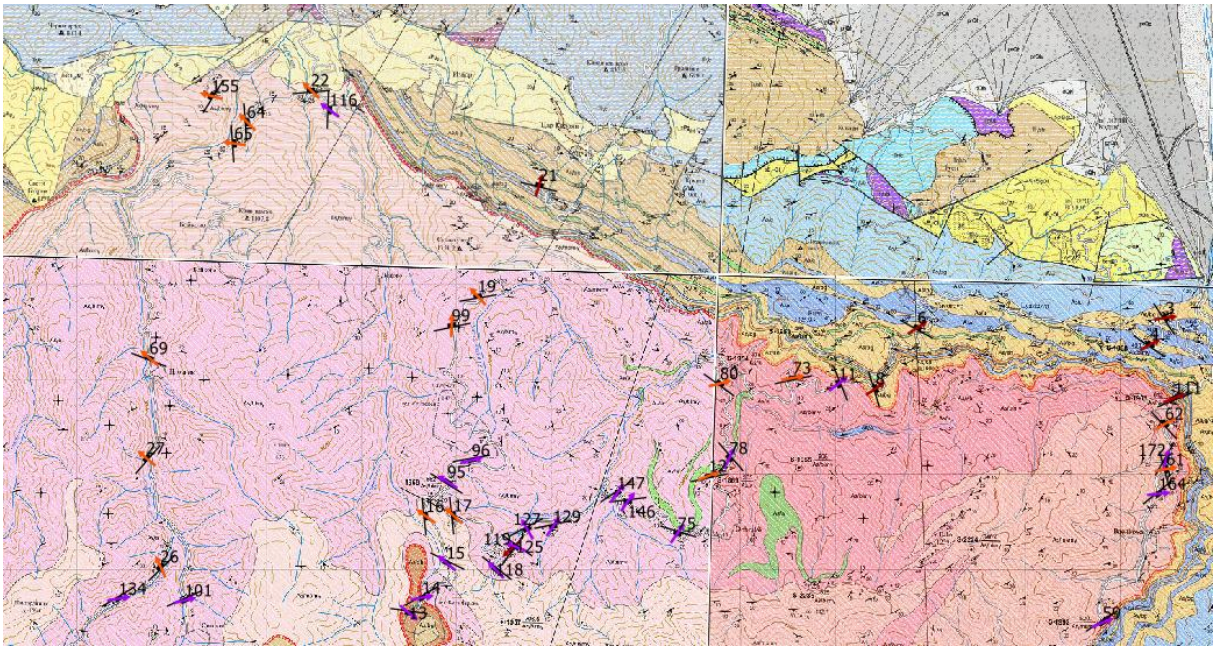

Figure 24 - Part of the fieldwork area of this study, showing the Upper Unit and Uppermost Unit, after Bulgarian geological map sheets and Schmid *et al.* (2013) and D3 foliation planes and shear senses (arrows). The data is obtained from fieldwork and optical microscopy. The labels represent placemark numbers.

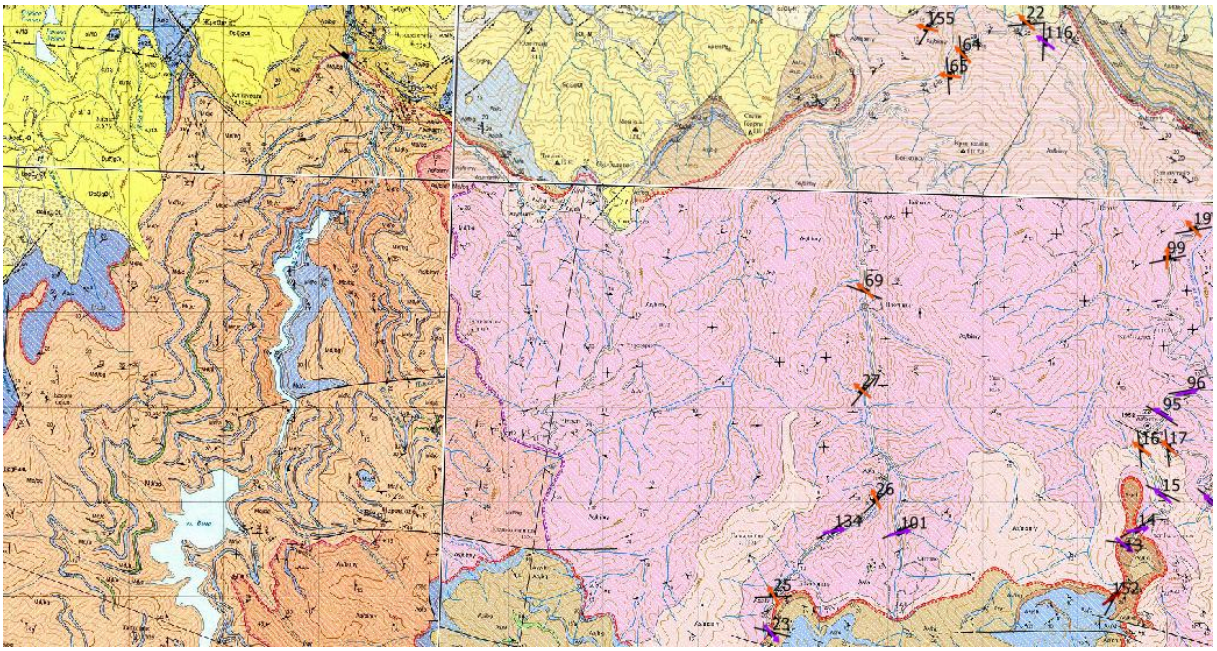

Figure 25 - Part of the fieldwork area of this study, showing the Upper Unit and Uppermost Unit, after Bulgarian geological map sheets and Schmid *et al.* (2013) and D3 foliation planes and shear senses (arrows). The data is obtained from fieldwork and optical microscopy. The labels represent placemark numbers.

For the complete subdivision of lithologies in the area of interest, the reader is referred to Sarov (2007).

For a more detailed description of the structural geological characteristics of the rocks, reference is made to Van der Sluis (2015).

Metamorphic petrologic and igneous characteristics

General features

Lithologies recording a similar mineral assemblage are migmatized biotite and amphibole-biotite gneisses, muscovite to two-mica gneisses of the Chepinska, migmatized biotite and amphibole-biotite gneiss of the Madan, biotite-epidote metagranites, muscovite metagranites (of the Upper unit) and amphibole-biotite gneisses and gneiss-schists (of the Uppermost unit). These consistently record the mineral assemblage: quartz, biotite, muscovite, K-feldspar, ±chlorite, with minor variations and additional minerals.

Amphibolites from both the Upper unit and Uppermost unit consistently record the mineral assemblage: amphibole (hornblende), biotite, muscovite and chlorite.

Marbles with graphite and medium-grained marbles both record a similar mineral assemblage. The crystal size of the marbles with graphite is larger than the crystal size of the massive marbles of the Uppermost unit. Impure marbles have been confirmed from both types of marble.

Biotite-schist with and without garnet of both the Upper unit and Uppermost unit consistently records the mineral assemblage: amphibole (hornblende for Upper unit, actinolite for Uppermost unit), garnet, biotite, muscovite, chlorite and K-feldspar.

Ultramylonites have been observed in biotite-epidote metagranites.

Pegmatite is generally thought to have formed in association with core complexes (personal communication Liviu Matenco; Jahn-Awe *et al.*, 2012). However, different generations of pegmatite seem to exist. Veins of this felsic material (pegmatite) seemingly contain remnant garnet crystals, occasionally.

Flow folds have formed during migmatisation in the migmatized biotite and amphibole-biotite gneisses, which indicate that the felsic material present in the hinge zones of folds was not completely solidified on folding.

Ptygmatic folds are indicative for in situ melting in the granites from which migmatized biotite and amphibole-biotite gneiss originated.

High-grade rocks that have ±N(W)-dipping foliation in association with top-N shear sense (±N extension) are believed to be located in a position to remote from detachments so that no retrograde characteristics could be documented.

The fold axes of the E-W-trending folds are ±parallel to pervasive N-plunging extension lineation, in occurrence with low-grade rocks.

The presence of chlorite may evidence (late-stage) retrogression.

4.2 – Microanalytical results

4.2.1 - Optical Microscopy

High-grade and prograde metamorphic evidence

The outer grain boundaries of stable garnets are generally often straight, and bordered by (seemingly stable) minerals, which include white mica, feldspar and mostly quartz. Original garnets are often still present or only partly recrystallized, in which case the original shape of garnet crystals can often still be recognized (figure 26 to 28, the XPL versions of which are presented in appendix 2.3; see figure captions). Stable garnet crystals contain little inclusions.

Quartz has relatively small grain size and is deformed by subgrain rotation, as well as by grain boundary migration in sample 167. These features would indicate quite high temperature and pressure deformation.

Figure 26 – Sample 167. Seemingly stable µm-scale sized garnet. It is directly bordered by a rim of dark-colored material of which the nature cannot be constrained by optical microscopy. The crystal of garnet does not contain inclusions or internal breakdown-products associated with it.

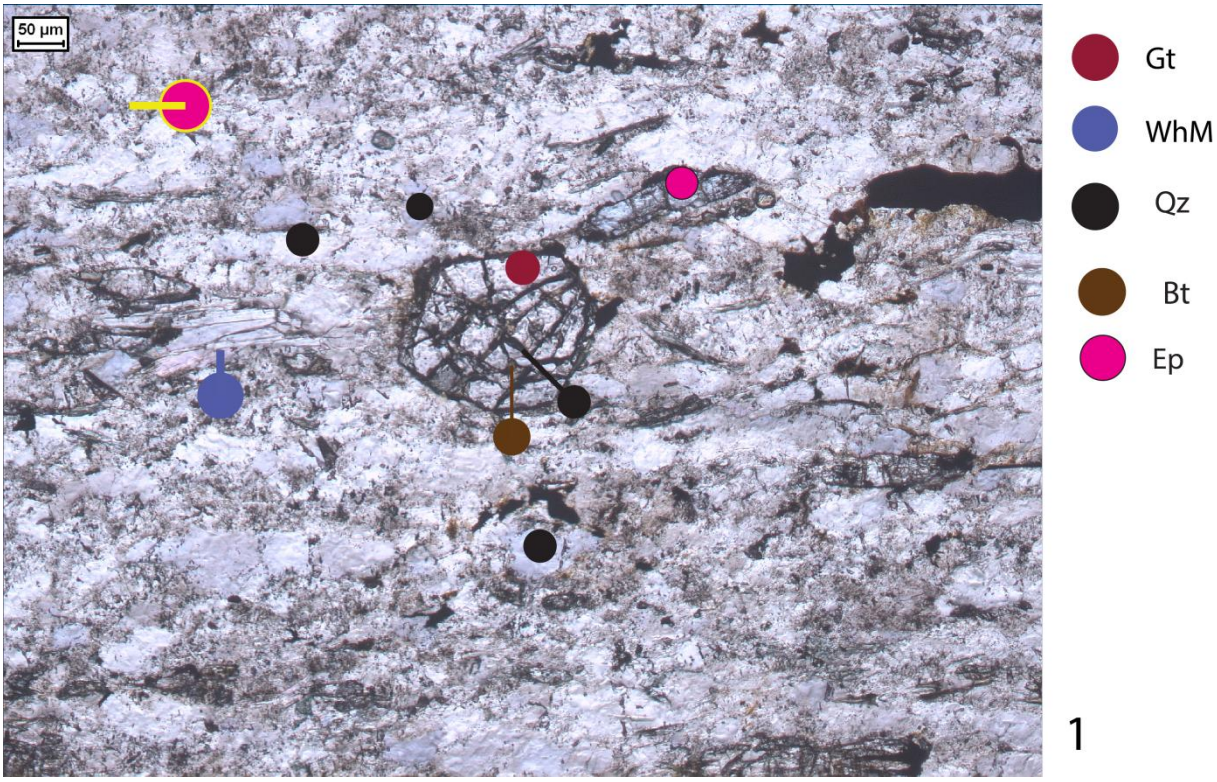

Figure 27 – Sample 23. A µm-scale sized gt clast that appears relatively stable. Grain boundaries of the garnet are relatively straight and the crystal has its distinctive hexagonal shape. It contains relatively small cracks, but is not fragmented. Garnet has partly broken down, the products of which coincide with the center of the garnet. The breakdown products include quartz and biotite. The XPL version of this area is presented in appendix 2.2, figure 22. Scale bar reads 50 µm.

Figure 28 - Sample 23. A µm-scale sized gt that appears relatively stable. Grain boundaries of the garnet are relatively straight and the crystal partly has its distinctive hexagonal shape. It contains relatively small cracks, and is slightly fragmented. Garnet has partly broken down into quartz and white mica. The XPL version of this area is presented in appendix 2.2, figure 23. Scale bar reads 50 µm.

The presence of stable, prograde quartz is confirmed that is interpreted to have crystallized from unstable, lower-grade feldspar (Samples 85, 14; figures 29 to 31). The presence of quartz may be the result of the prograde reaction chl+kfs = annite+ms+qtz+H_2O. Amphibole (hornblende) is thought to have grown at the expense of the unstable clasts hosted by 85, once these were fragmented. For sample 85 (figure 29), it can be observed that coarse grained crystals of unknown identity exist in the tails of unstable feldspar, relative to the interior. Adversely, sample 14 hosts recrystallized quartz that is progressively fine-grained in the tails of the clast (fig. 31). From the orientation of the minerals present internally, it appears that the former clast might record an earlier foliation. This foliation has been indicated by dashed red lines in figure 30. Sample 85 has been subject to two metamorphic stages: amphibolite facies metamorphism (from the assemblage hornblende + plagioclase) and greenschist facies metamorphism (from the assemblage chlorite and epidote).

Figure 32 displays quartz that has been deformed by (relatively high-temperature) dynamic recrystallization.

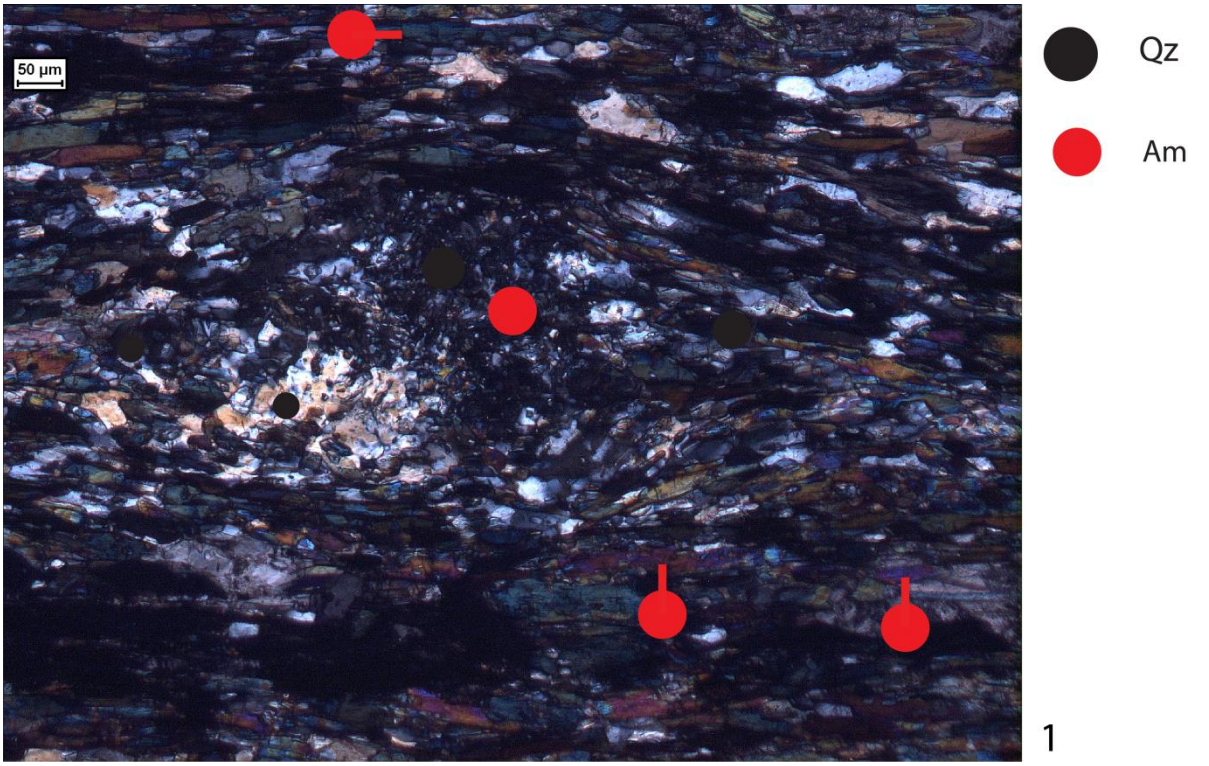

Figure 29 – Sample 85. A former µm-scale sized clast of feldspar which has seemingly been outstretched and become unstable. Internally, it consists of a relatively fine-grained assemblage of different minerals. Quartz is interpreted to have crystallized from feldspar during prograde metamorphism. Outstretched minerals have been wrapped around the former feldspar clast. The PPL version of this area is presented in appendix 2.2, figure 9.

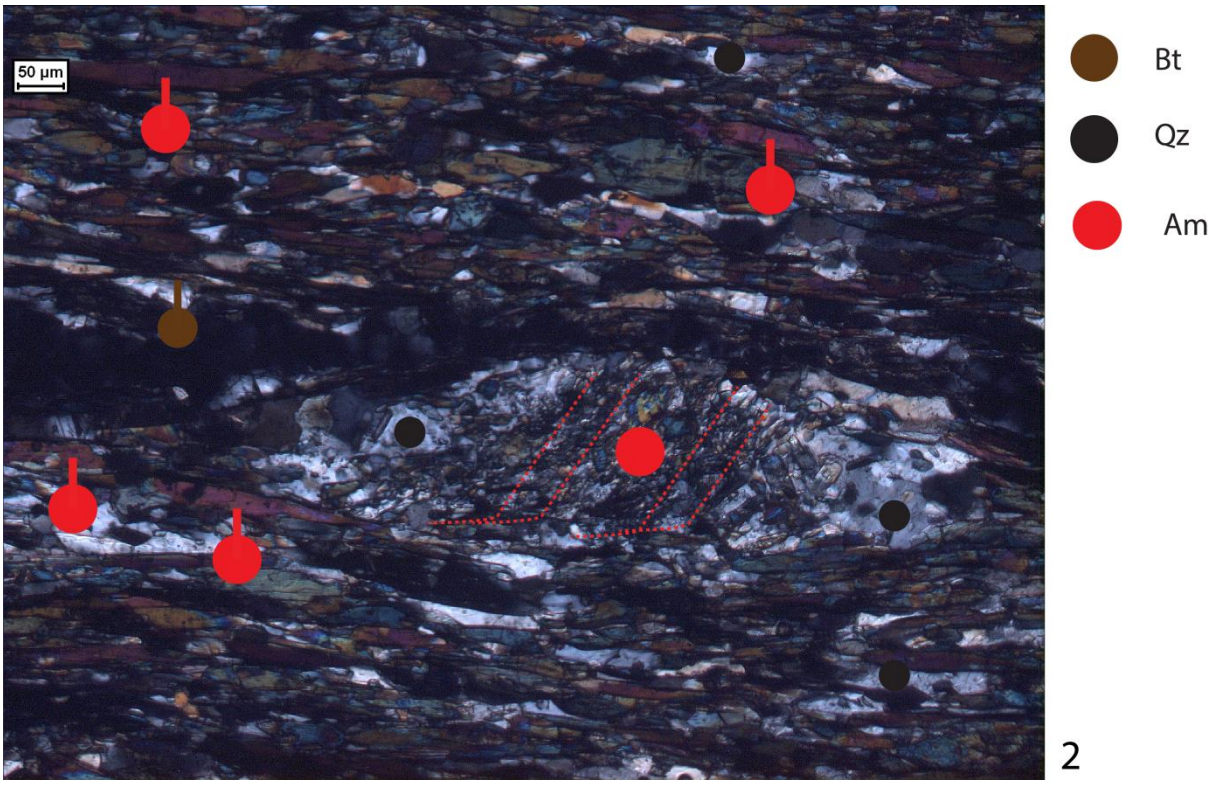

Figure 30 – Sample 85. A former µm-scale sized clast of feldspar, which has seemingly been outstretched and become unstable. Internally, it consists of a relatively fine-grained assemblage of different minerals. Quartz is interpreted to have crystallized from feldspar during prograde metamorphism. Dashed red lines indicate a possible earlier mineral-foliation recorded by the interior of the former clast. Coarse-grained crystals exist in the tails, relative to the interior. Amphibole might account for the incorporation of low-grade fluids in unstable crystals. Outstretched clasts of quartz and amphibole have wrapped around the main former feldspar clast. The PPL version of this area is presented in appendix 2.2, figure 10.

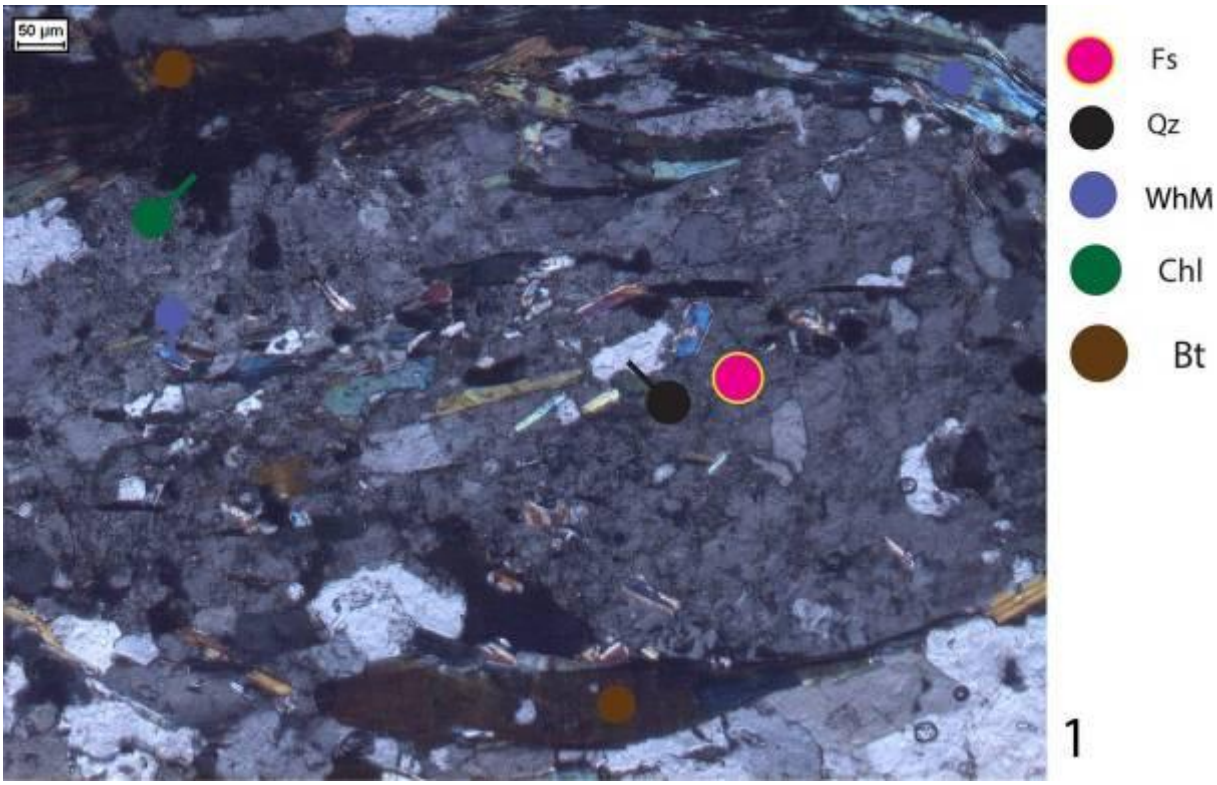

Figure 31 – Sample 14. A relatively large mm-scale sized recrystallized quartz clast that has partly broken down into an assemblage of minerals, including mainly white mica. At the edge of the clast, crystals of white mica, biotite and chlorite have wrapped around the main quartz clast. The PPL version of this area is presented in appendix 2.2, figure 12.

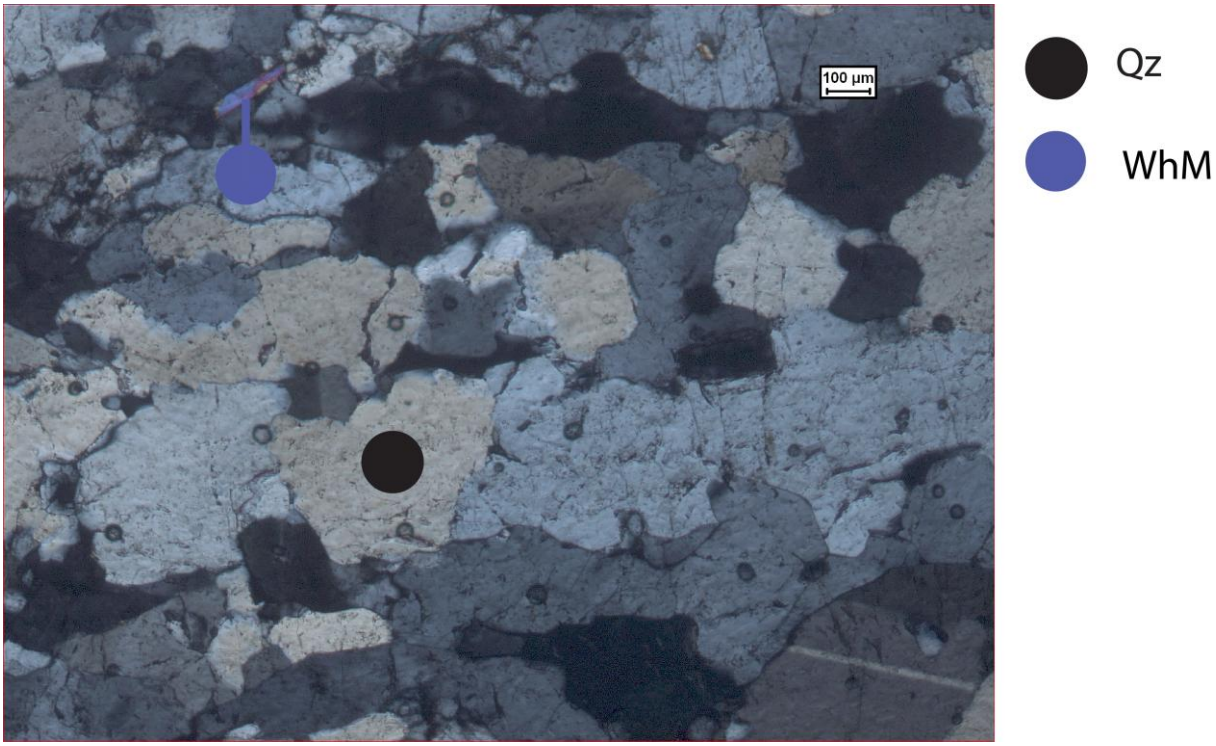

Figure 32 - Sample 16. Relatively large (up to) mm-scale sized grains of quartz, implying that originally grown grains have not been subject to a substantial degree of modification (low grade bulging in quartz is also evident). Other quartz crystals have evidently been deformed by dynamic recrystallization (relatively high temperature grain boundary migration).

Evidence of retrogression and low-grade metamorphism

Minerals have evidently been affected by changing metamorphic conditions. The presence of unstable garnet is confirmed. Garnet has been fragmented and overgrown by biotite in sample 167 (see figure 33). From the random orientation of biotite grains, it can be confirmed that sample 167 has experienced upper greenschist to amphibolite facies metamorphism; conditions at which biotite was stable (personal communication with Jan Pleuger).

Mineral instability exists. Garnet is obviously unstable in samples 133 and 167 (see figures 33-37). In sample 167 it appears very erratic and occasionally sheared and rotated (figure 35, 37).

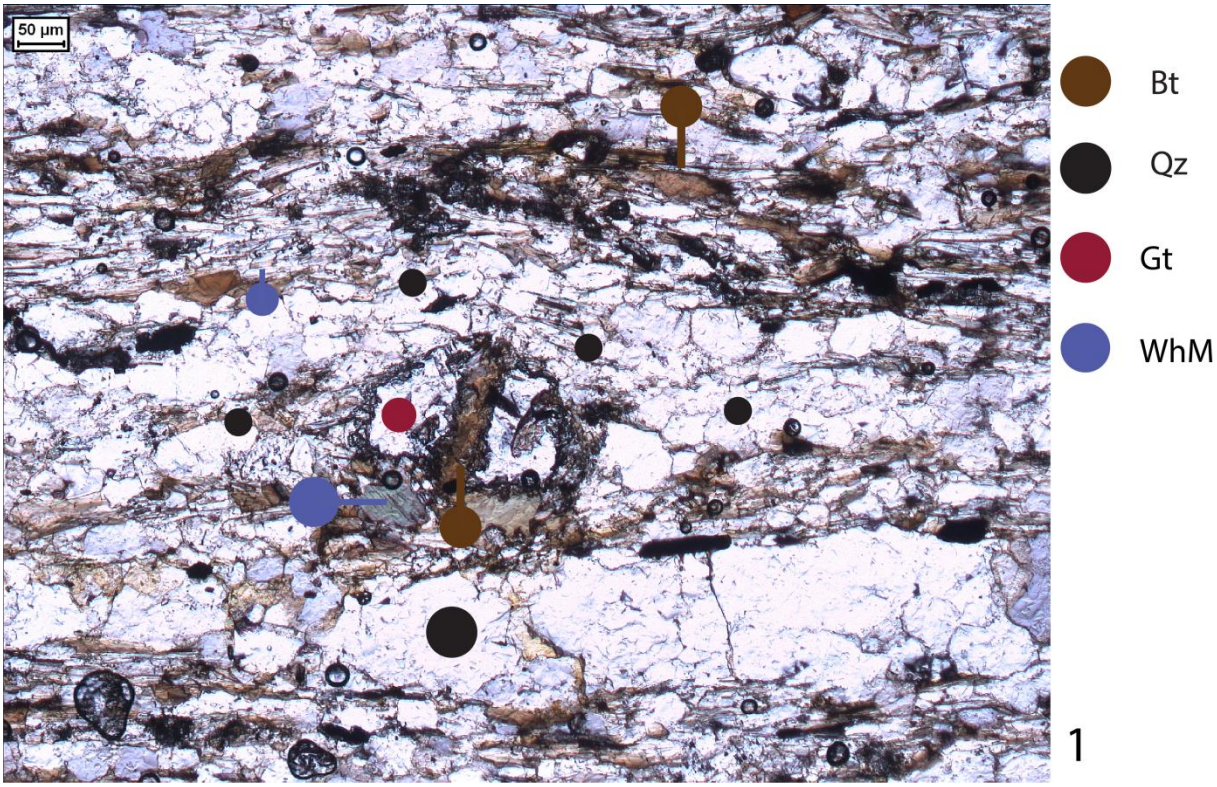

Figure 33 – Sample 167. Unstable µm-scale sized garnet has erratic grain boundaries. The crystal is fragmented and the cracks are filled with biotite. The original shape can still be recognized. Garnet is directly bordered by a corona of dark-colored material of which the nature cannot be constrained by optical microscopy. Moreover, white mica, quartz and biotite appear in association with garnet. The XPL version of this area is presented in appendix 2.2, figure 16. Scale bar reads 50 µm.

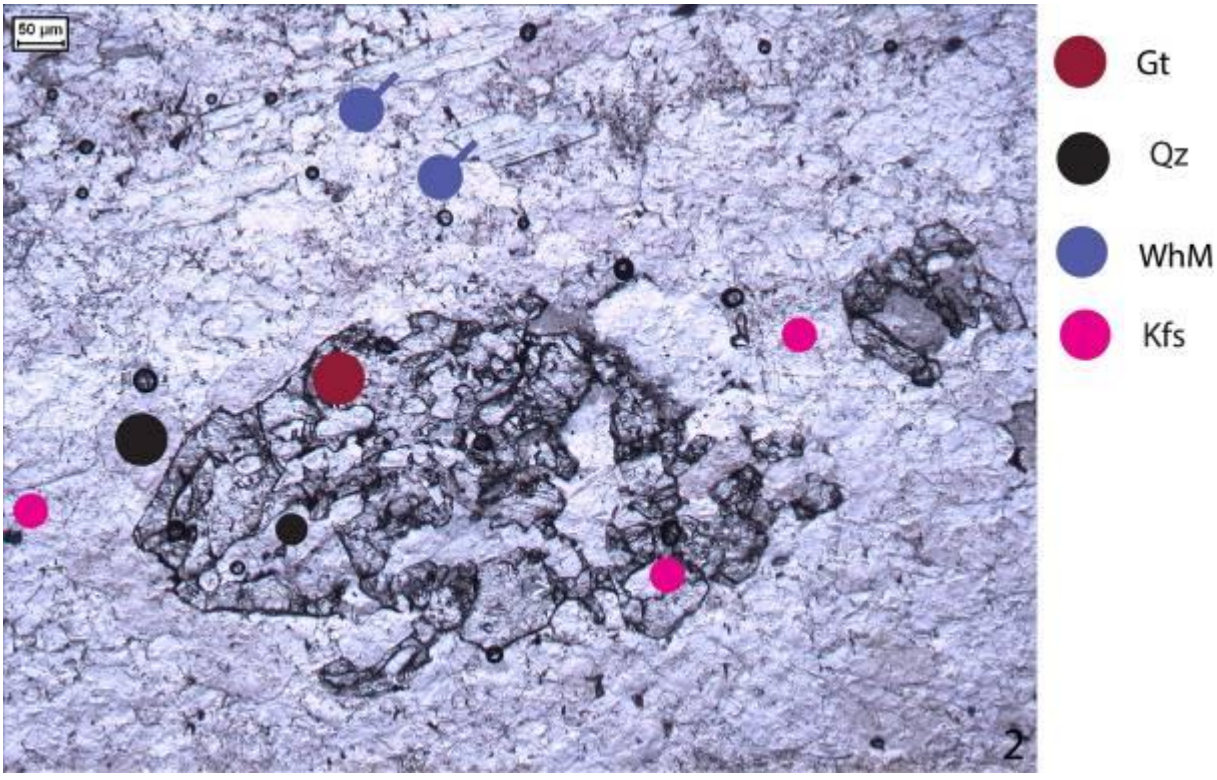

Figure 34 – Sample 133. Unstable µm-scale sized garnet which appears to have once originated as a single (relatively large), complete garnet crystal. Garnet possesses fairly straight grain boundaries which border white mica, feldspar and mostly quartz. Internally, the garnet has recrystallized into quartz and k-feldspar, mainly. This image has been rotated 180° from its original position in appendix 2.2, figure 1. The XPL version of this area is presented in appendix 2.3, figure 3.

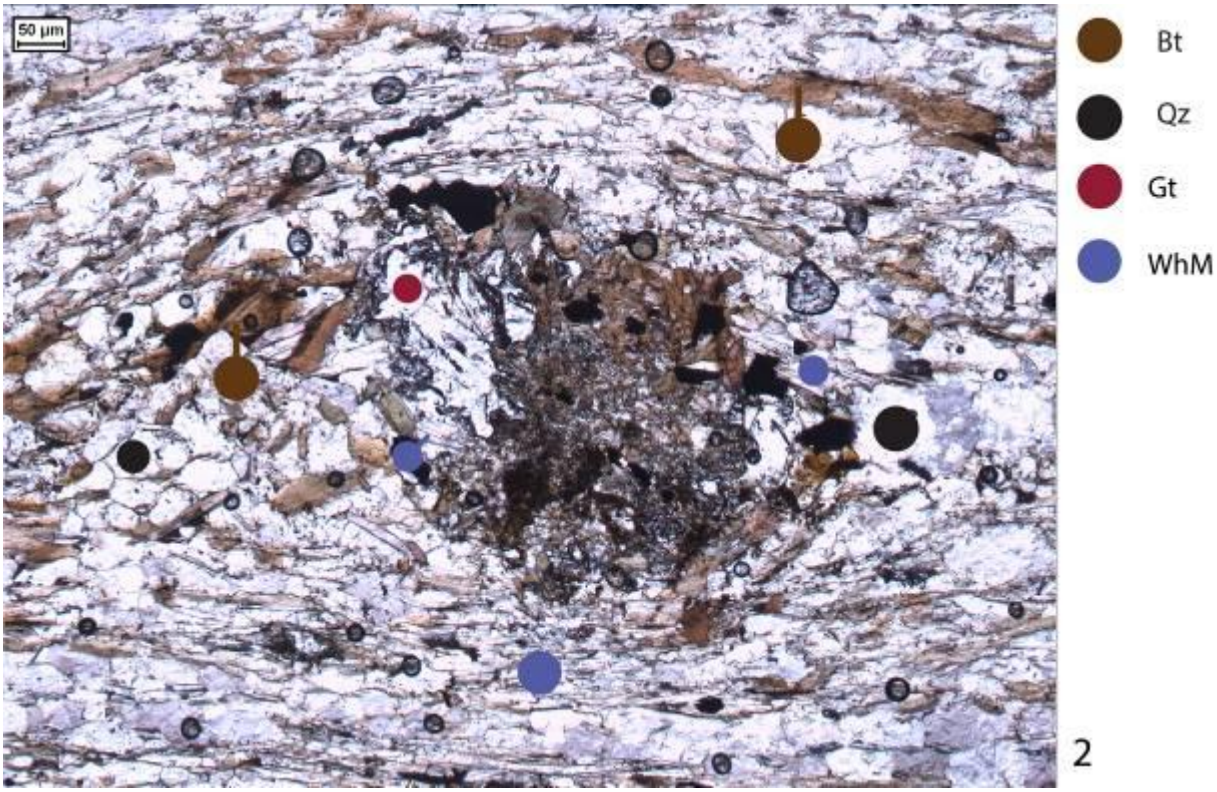

Figure 35 – Sample 167. Unstable µm-scale sized garnet has erratic grain boundaries. Garnet is directly bordered by a corona of dark-colored material of which the nature cannot be constrained by optical microscopy. To the right of garnet, a very fine-grained assemblage of white mica, quartz and biotite exists. Possibility exists that this assemblage represents the breakdown products of garnet, in which case most of the area is occupied by a former garnet clast. It appears that this arrangement has been rotated dextral, with surrounding minerals wrapping around it. Quartz has crystallized in the pressure shadow of the rotated assemblage. The XPL version of this area is presented in appendix 2.2, figure 17. Scale bar reads 50 µm.

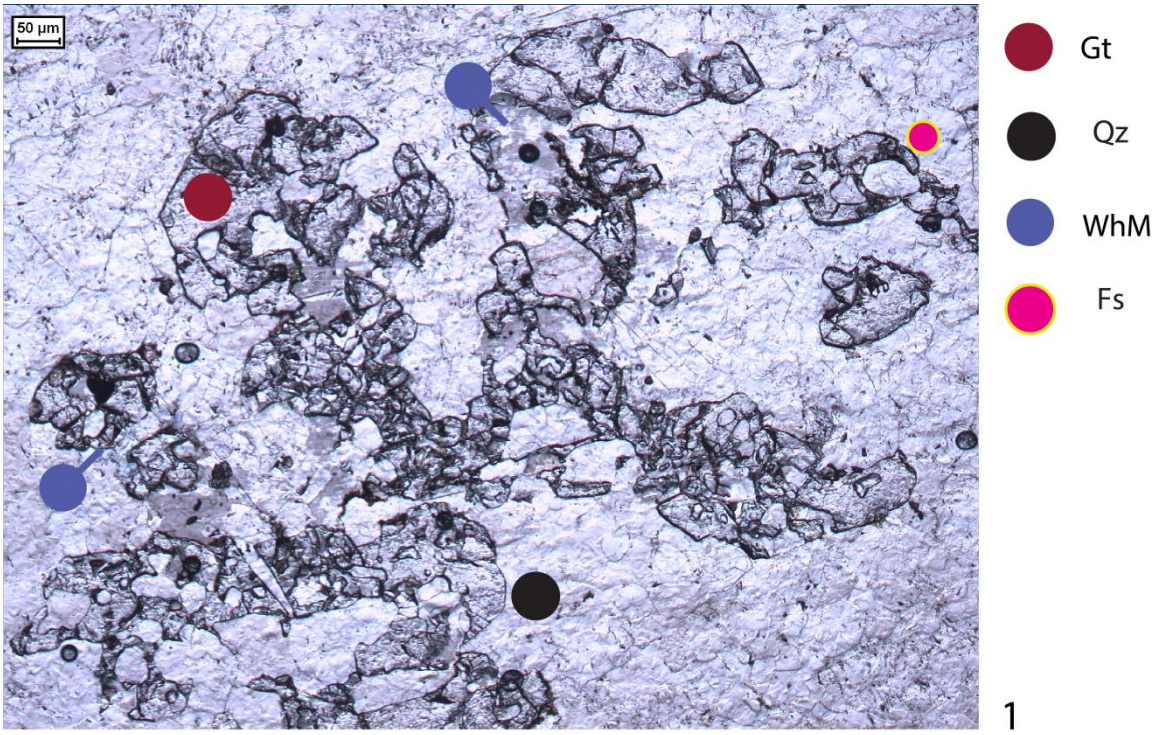

Figure 36 – Sample 133. Unstable mm-scale sized garnet, which appears to have once originated as a single (relatively large), complete garnet crystal. Garnet possesses fairly straight grain boundaries which border white mica, feldspar and mostly quartz. This image has been rotated from its original position in Appendix 2.2, figure 1. The XPL version of this area is presented in appendix 2.2, figure 2.

Figure 37 – Sample 167. Unstable µm-scale sized garnet has been fragmented and broken down in different types of minerals. Quartz appears in association with garnet and is supposedly a breakdown product of the unstable garnet. Additional minerals seemingly crystallized at the expense of garnet include biotite and white mica. Quartz and biotite are moreover present in the pressure shadows/tails of the unstable garnet crystal. The complete assemblage has seemingly been rotated and biotite, together with quartz wrap around the unstable garnet crystal. The XPL version of this area is presented in appendix 2.2, figure 18. Scale bar reads 50 µm.

It is suggested that unstable minerals have broken down into a (relatively fine-grained) assemblage of different minerals.

Breakdown products mostly form inclusions or border the unstable crystal with which these are associated.

Quartz, white mica and biotite form a common assemblage of breakdown products for unstable garnet. For garnet in sample 133, feldspar forms an addition to this assemblage (figure 34). Quartz appears the most common of breakdown products, which means it has also been stable during retrogression.

Garnet crystals are often directly bordered by a corona of dark-colored material of which the nature cannot be constrained by optical microscopy (figures 26, 33, 35). It is thought this corona is indicative for retrograde metamorphism.

The presence of chlorite often justifies retrograde metamorphism. This can be observed from samples 85, 23, 14.

The presence of carbonate in sample 167 and 85 is thought to result from the breakdown of anorthite. This would exemplify normal zoning, a type of plagioclase zoning where Ca decreases towards the rim of the crystal and is transferred to carbonate. Normal zoning is characteristic for retrograde metamorphism. The presence of epidote in sample 23, 85(?), may indicate decomposition of the anorthitic component of plagioclase.

Relatively large grain size of quartz (and plagioclase) and the limited extent of apparent high-grade dynamically recrystallized quartz provide another diagnostic for low-grade conditions. Sample 16 fulfills both criteria to a certain extent (see figure 38).

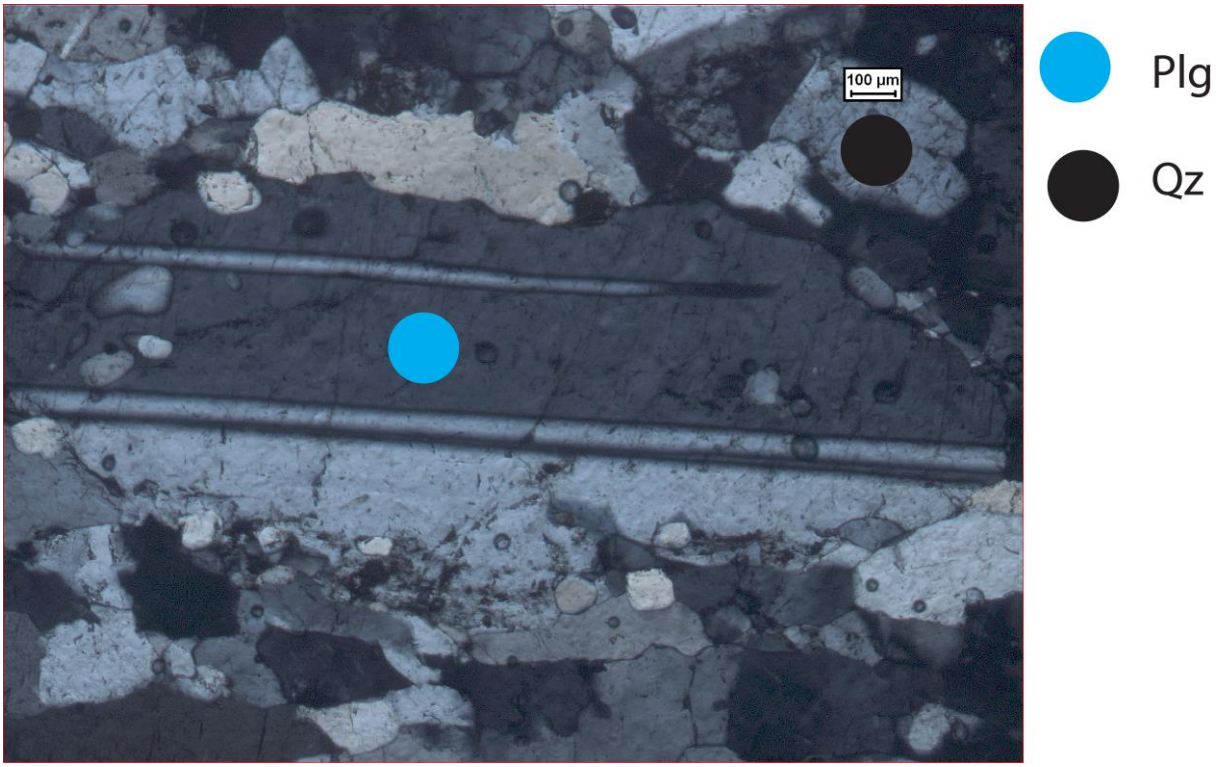

Figure 38 – Sample 16. Relatively large mm-scale sized grain of plagioclase, implying that the originally grown grains have not been subject to a substantial degree of recrystallization.

4.2.2 - EMPA

Prograde evidence

Prograde metamorphic characteristics are encountered in samples 167, 23 and 133.

Reverse zoning of plagioclase is encountered continuously in sample 167 in Niels_167_Foto-section01 (figure 39) & Niels_167_Foto-section04b (appendix 2.3, figure 9) and in area Niels_23_Foto-section02e in sample 23 (figure 46). Variation in chemical composition within plagioclase accounts for the markedly color-differences.

In Niels_167_Foto-section01, reversely zoned plagioclase occupies internal fractures of relatively homogenous almandine. As rim-almandine is not evidently depleted in Ca, this raises questions as to the source of Ca for the plagioclase. As at lower grade garnet is relatively immobile to element transfer, this out rules the possibility of Ca having been obtained from the whole of the garnet (including its center). Most likely, garnet rims have decayed altogether and released Ca and Al to form anorthite and Fe to form biotite.

From the WD measurements associated with sample 167, it can be generally implied that certain minerals have grown initially during prograde metamorphism, after which decreasing metamorphic grade resulted in extensive mineral instability.

Area Niels_167_Foto-section05 (figure 40) displays an arrangement which is interpreted as a former garnet crystal, remnants of which have been maintained within the interior of the arrangment, as well as at the edge. Interior garnet ([1] and [6]) is dominantly almandine and contains minor spessartine. Edge garnet ([21]) is increasingly enriched in almandine, pyrope and GAU (grossular-andradite-uvarovite) and contains less spessartine. Pyrope represents the high grade garnet endmember (Putnis, 1992).

The entire assemblage of area Niels_167_Foto-section05 is bordered by biotite. Biotite in area Niels_167_Foto-section05 is enriched in annite, relative to biotite in Niels_167_Foto-section01, which contains phlogopite/annite in a ratio ±45/55. Biotite in area Niels_167_Foto-section05, bordering the entire assemblage, appears to have grown from chlorite, as chlorite is interpreted to have remained in the center of a mica crystal, currently dominated by biotite.

Heterogeneous, zoned, white mica, adjacent to unstable garnet, is recorded by sample 133 (133-Gt-01b, [15-16] (figure 42). Enrichment in the Si-content of white mica (from [15] to [16]), on crystal growth, generally indicates increasing P-conditions (Zhu & Wei, 2007 and references therein).

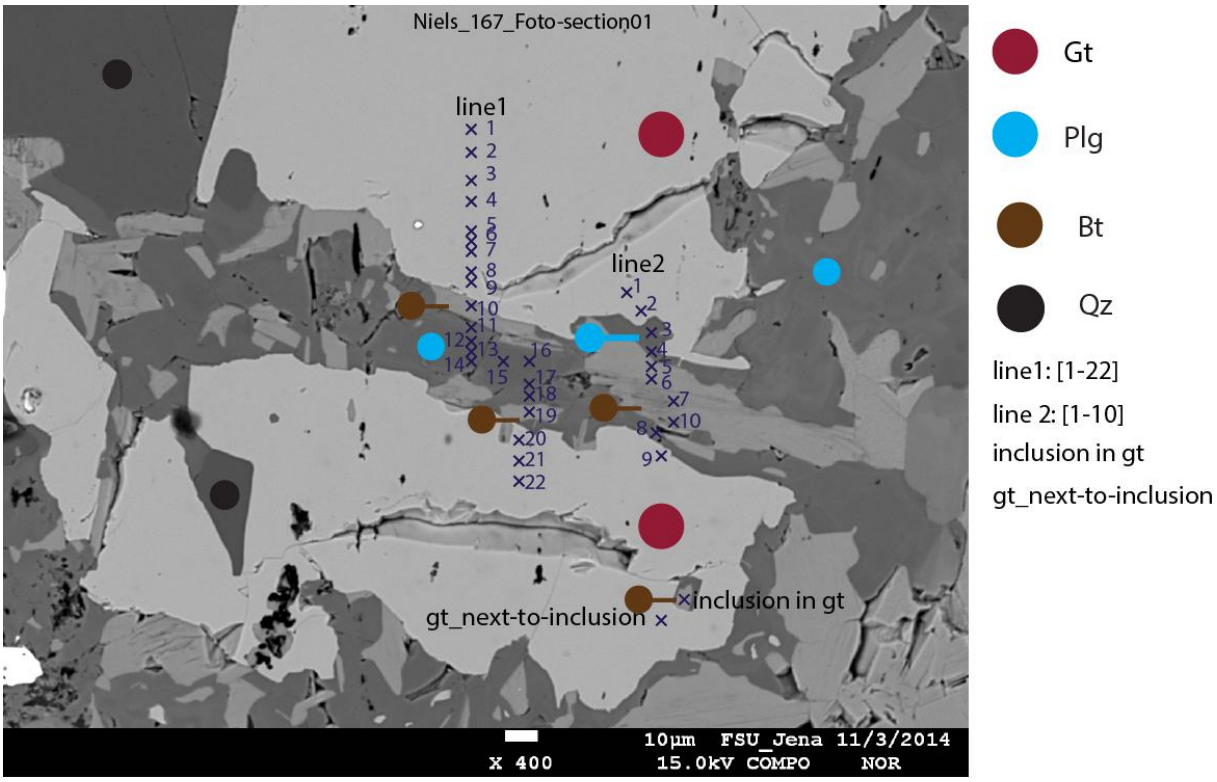

Figure 39 – Niels_167_Foto-section01, showing broken up garnet. The space left is occupied by mainly plagioclase and biotite. Line 1 and 2 represent lines of consecutive WD measurements. Plagioclase is reversely zoned and thus formed by prograde metamorphism. See the text for further explanation.

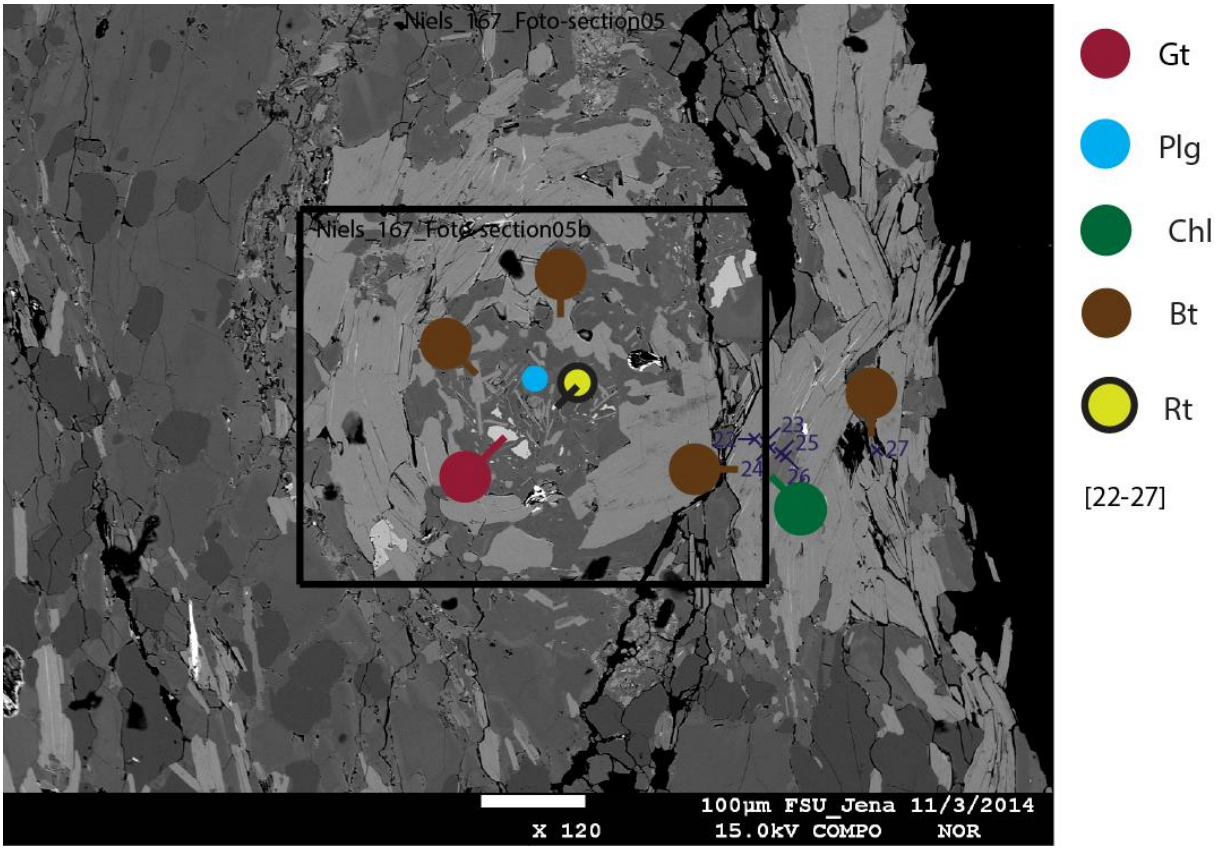

Figure 40– Niels_167_Foto-section05. The area within the black-rimmed rectangle is a former garnet, broken down into mainly plagioclase and biotite. Ancient garnet is preserved within the center of the composition and at the edge. Garnet located in the center is lower grade than the garnet at the edge. The garnet has thus initially grown by prograde metamorphism, where after the metamorphic conditions of the crystal degraded. See the text for further explanation.

Retrograde evidence

Sample 133, 14, 167, 23 host unstable minerals (garnet) that contain internal fractures and voids.

Retrograde metamorphic characteristics can be observed from samples 133, 14, 167 and 23. The common assemblage of minerals hosted by internal fractures and voids in garnet is quartz and white mica. Additionally, inclusions of plagioclase, feldspar and biotite can be confirmed (see figures 41 to 46). Commonly, unstable garnet is bordered by quartz and plagioclase. Additionally, unstable garnet is bordered by K-feldspar, white mica, biotite (±chloritized) and epidote (see figures 41 to 46). Chlorite appears in association with garnet in sample 23.

Heterogeneous, zoned garnet, grown during retrograde metamorphism, is encountered in sample 133 (133-Gt-01b, [8-9] (figure 42) and 133-Gt-01c, [18-19] (figure 43)), sample 14 (Niels_14_Foto-section01, [7], [11-12] (figure 44), sample 23 (Niels_23_Foto-section01, [2], [7] (figure 45) and

Niels_23_Foto-section02e, [65-66], [69] (figure 46)), even though it records high grade, with highest pyrope content (±11.5%) preserved in the interior of (retrograde) garnet.

Homogeneous muscovite hosted by the interior of unstable garnet is encountered in sample 133 (133-Gt-01, [3] (figure 41) and 133-Gt-01b, [13] (figure 42)).

Homogeneous, unzoned muscovite bordering unstable garnet is encountered in sample 14 (Niels_14_Foto-section01, [12], [17], [19] (figure 44)).

Heterogeneous, zoned white mica, adjacent to unstable garnet, is recorded by sample 14 (Niels_14_Foto-section01, [1], [4] (figure 44)). Depletion in the Si-content of white mica, on crystal growth, generally indicates decreasing P-conditions, which means that this specific white mica crystal has grown coincident with retrograde metamorphism.

Datapoint 17 (133-Gt-01b) represents kaolinite, crystallized along the rim of white mica. This arrangement is reoccurring in area 133-Gt-01b. Kaolinite is generally produced by the chemical weathering of aluminum silicate minerals. Likely, kaolinite is produced by the chemical weathering of bordering white mica, which means that its production is unrelated to retrograde metamorphism and thus relatively late-stage.

Lamellae of albite in K-feldspar (bordering unstable garnet) are encountered in sample 133 (133-Gt-01c).

Normal zoning in plagioclase is encountered in sample 23 (Niels_23_Foto-section02c, [93], [99] (appendix 2.3, image 14)).

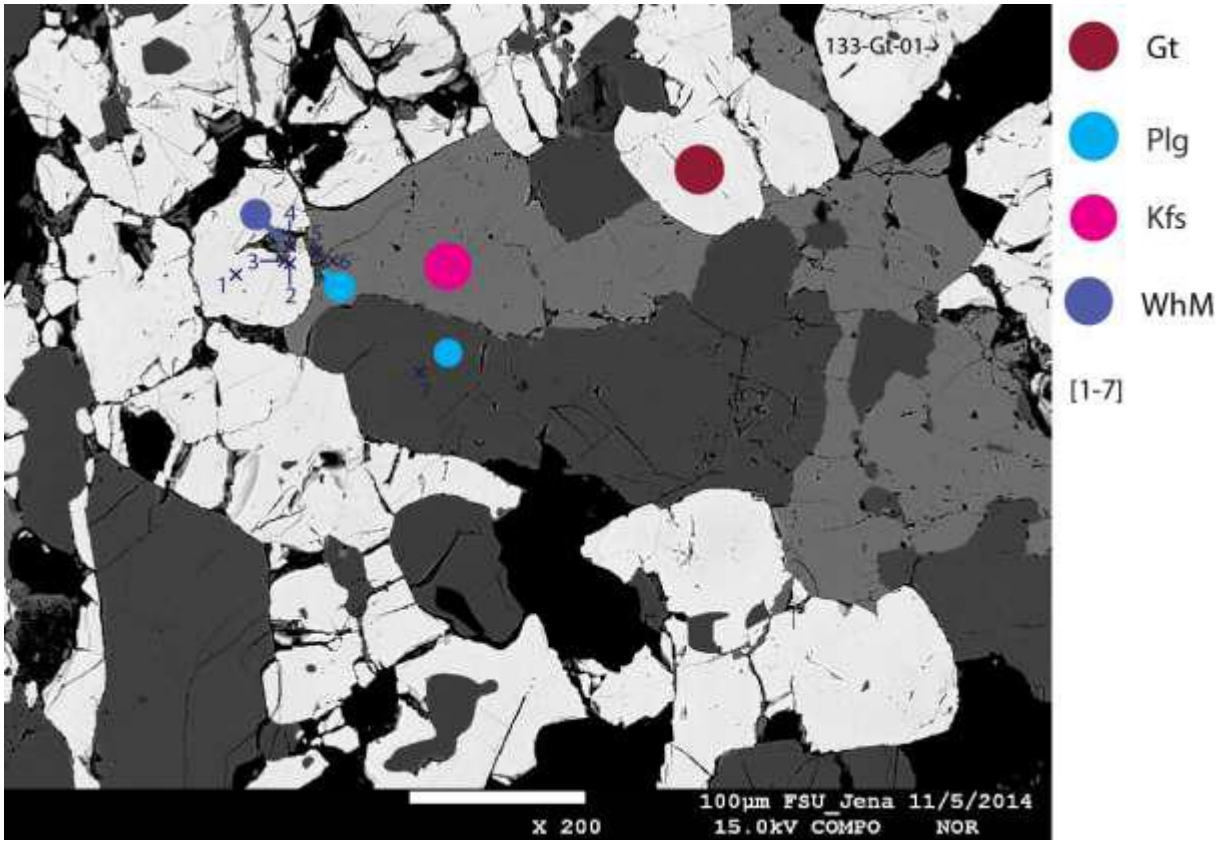

Figure 41 – Area 133-Gt-01, mainly displaying unstable garnet which has been broken down into an assemblage of different minerals. Garnet occasionally possesses fairly straight grain boundaries which border plagioclase and K-feldspar. White mica, K-feldspar and plagioclase seemingly form inclusions in garnet.

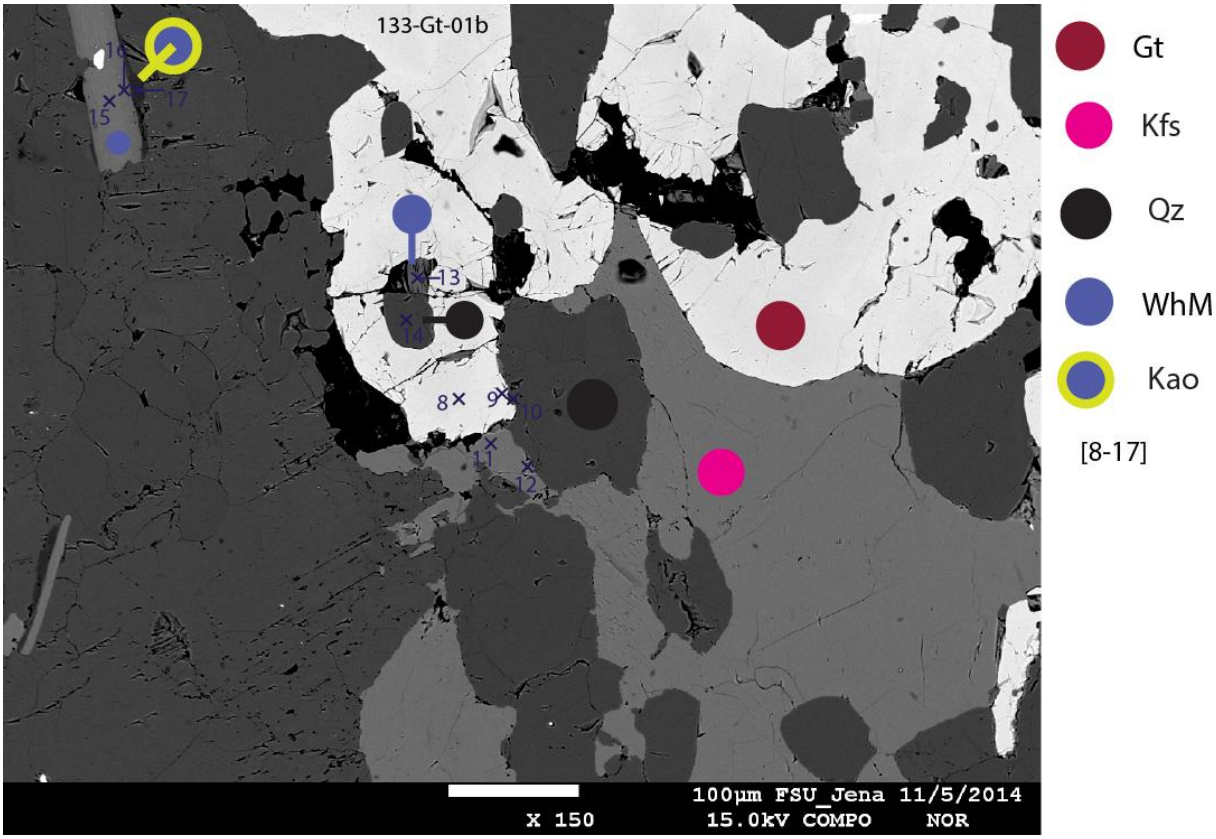

Figure 42 - Area 133-Gt-01b, displaying garnet. Garnet occasionally possesses fairly straight grain boundaries which border K-feldspar and quartz. White mica, K-feldspar and quartz are seemingly present internally.

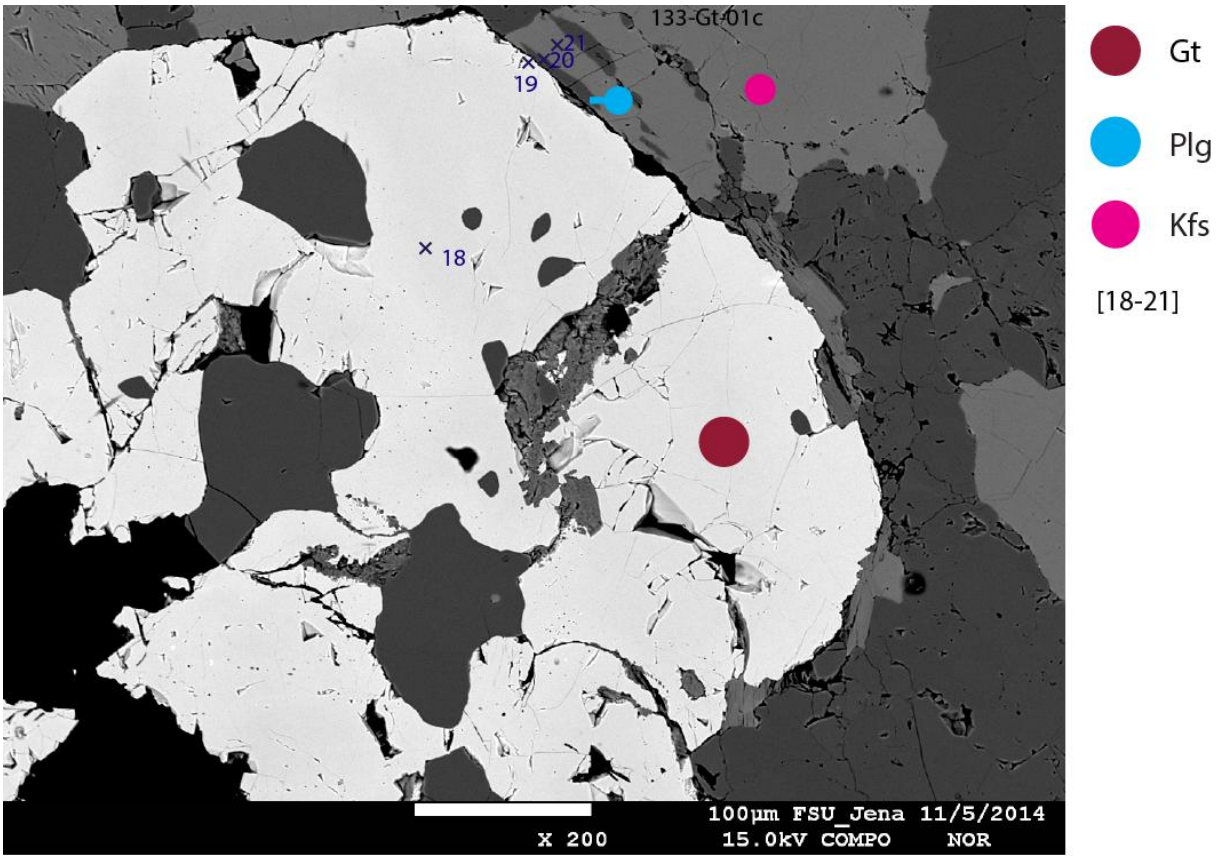

Figure 43 - Area 133-Gt-01c, mainly displaying garnet. Garnet occasionally possesses fairly straight grain boundaries which border plagioclase and K-feldspar and quartz. K-feldspar plagioclase and quartz are seemingly present internally.

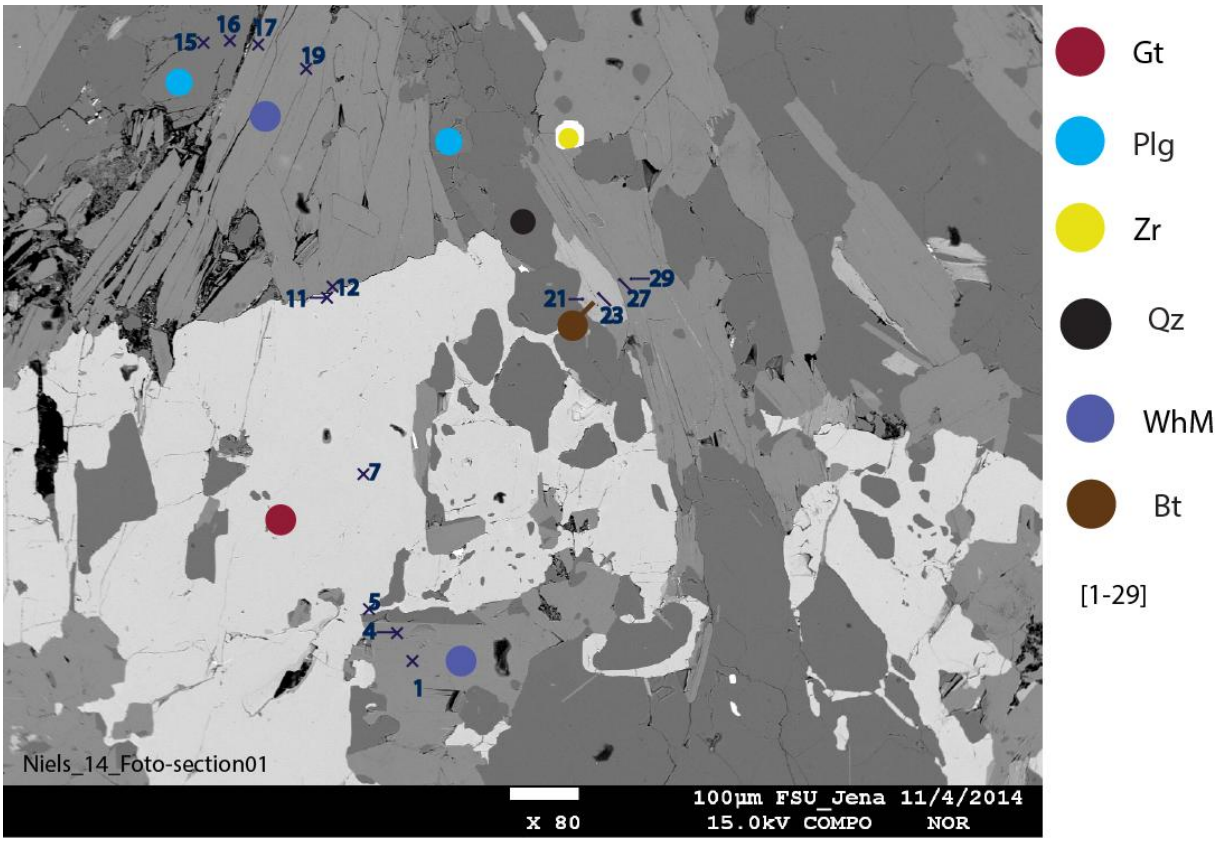

Figure 44 - Niels_14_Foto-section01. Homogeneous, unzoned and heterogeneous, zoned muscovite borders unstable garnet.

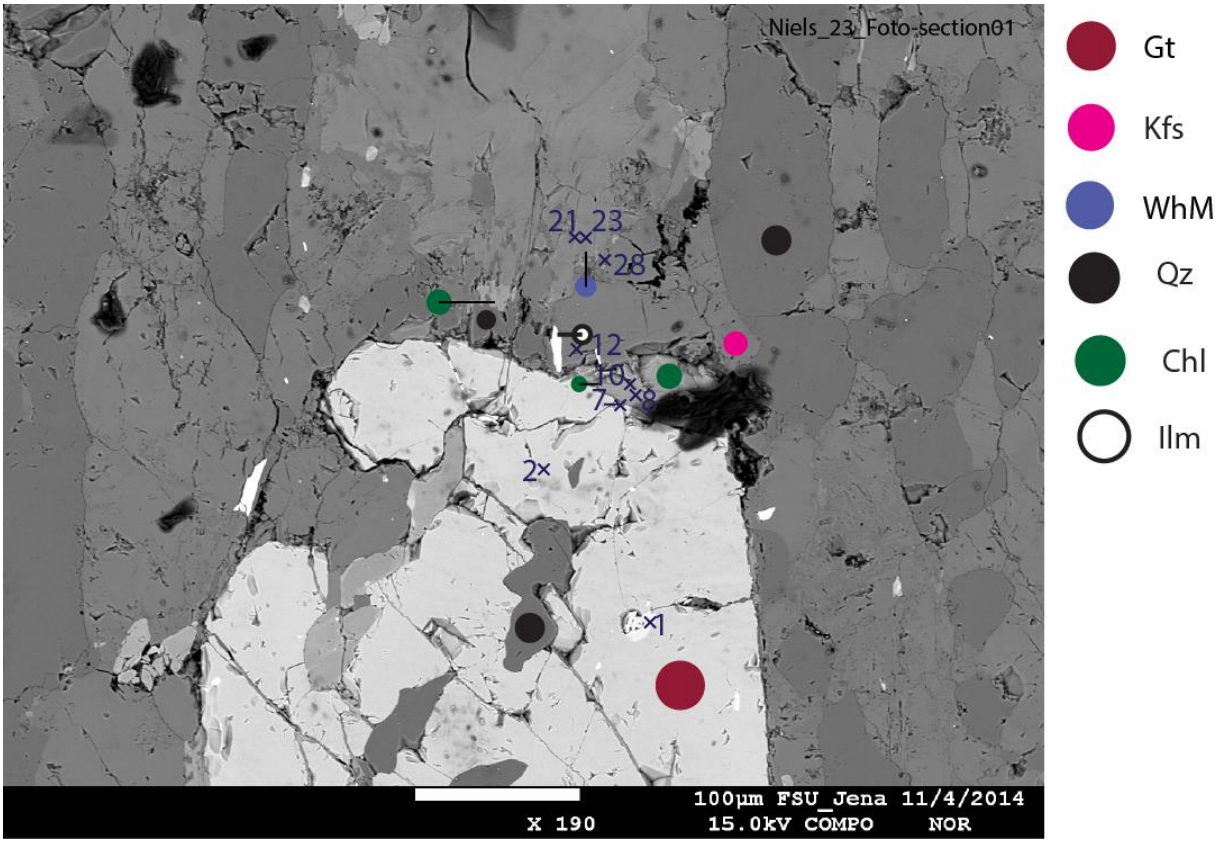

Figure 45 – BSE image of area Niels_23_Foto-section01. Garnet is often associated with white mica, epidote, feldspar, chlorite, quartz and ilmenite.

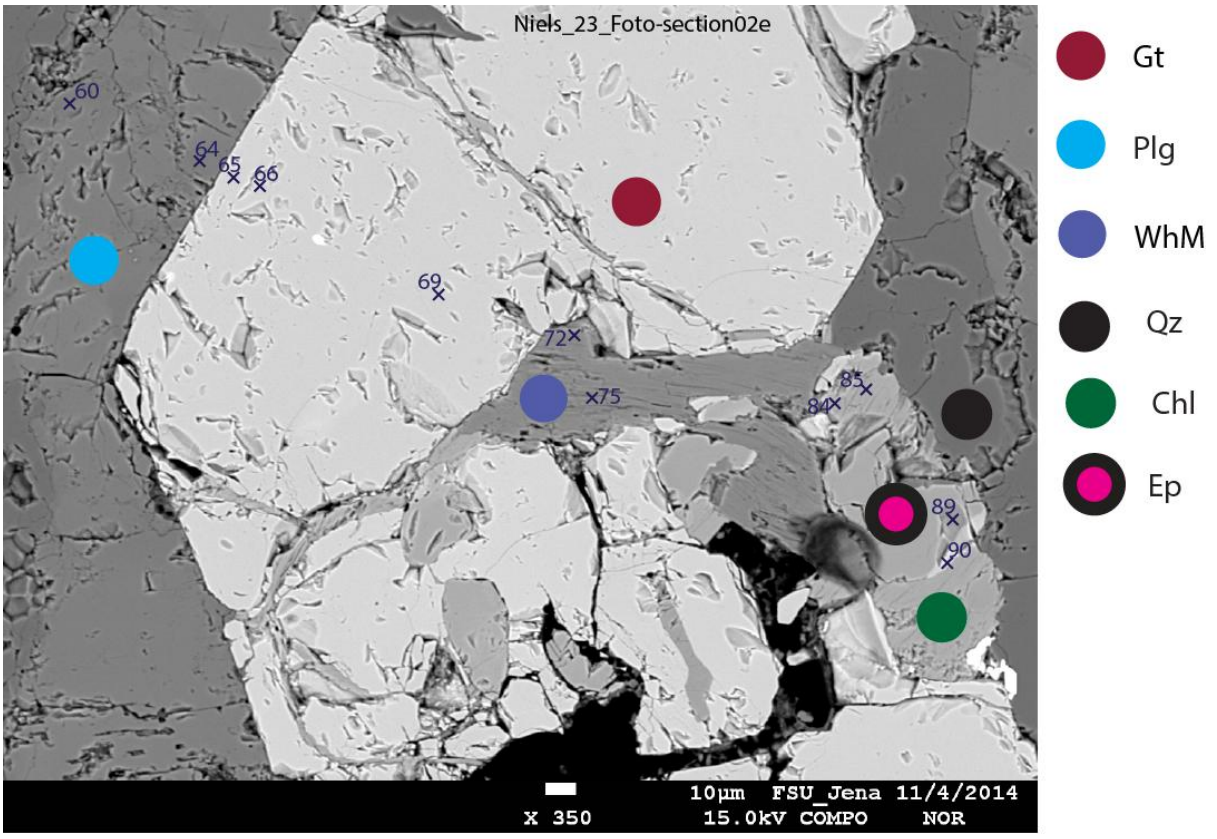

Figure 46– BSE image of area Niels_23_Foto-section02e. Garnet is associated with epidote, feldspar, chlorite, white mica and quartz.

4.2.3 - PT calculations and geothermobarometry

PT calculations

Garnet-biotite geothermometers may be applied to garnet and biotite hosted by Niels_167_Foto-section01. These geothermometers are based on the Fe-Mg exchange between garnet-biotite. Geothermometric calculations from 8 different geothermometers yield temperature calculations in the range of: T = 470-565˚C for a reference pressure of 5 kbar. [9] & [10] have been used as input for the calculations.

Attempt has been made in order to constrain whether or not the garnet-muscovite geothermometer can be used confidently for sample 133. From Wu & Zhao (2006), it is evident that this geothermometer has been calibrated for metapelitic samples in compositional ranges which do not coincide with those determined by EMPA analyses. Therefore, it is established that this geothermometer cannot be confidently employed.

Hornblende-plagioclase assemblages may be analyzed using the set of geothermometers after Holland & Bundy (1994). This set includes:

A) edenite + 4quartz = tremolite + albite

B) edenite + albite = richterite + anorthite

Following Holland & Bundy (1994), it is evident that these thermometers can be used over a broad range of bulk compositions for P: 1-15 kbar and T: 400-1000˚C. The typical temperature uncertainty for both thermometers is ± 35-40˚C.

The set of geothermometers after Holland & Bundy (1994) have been used for sample 85, employing the combined sets of spot analyses: [1+5], [23+22], [24+22], [26+25], [27+25] and [43+46] (see figures 47-50). Using the set of geothermometers after Holland & Bundy (1994) for sample 85, the following PT-estimates have been obtained:

A) T: 669-683˚C; P: 7.1-8.8 kbar.

B) T: 625-675˚C; P: 7.3-8.9 kbar.

It must be noted that it is thought these PT-estimates represent a rather inaccurate assessment. In either case, the pressure range suggested from these estimates is elevated to a degree much higher than logically expected for this sample, on the basis of microstructural analysis. It is therefore concluded that these PT-estimates may be used solely as a first-order indication.

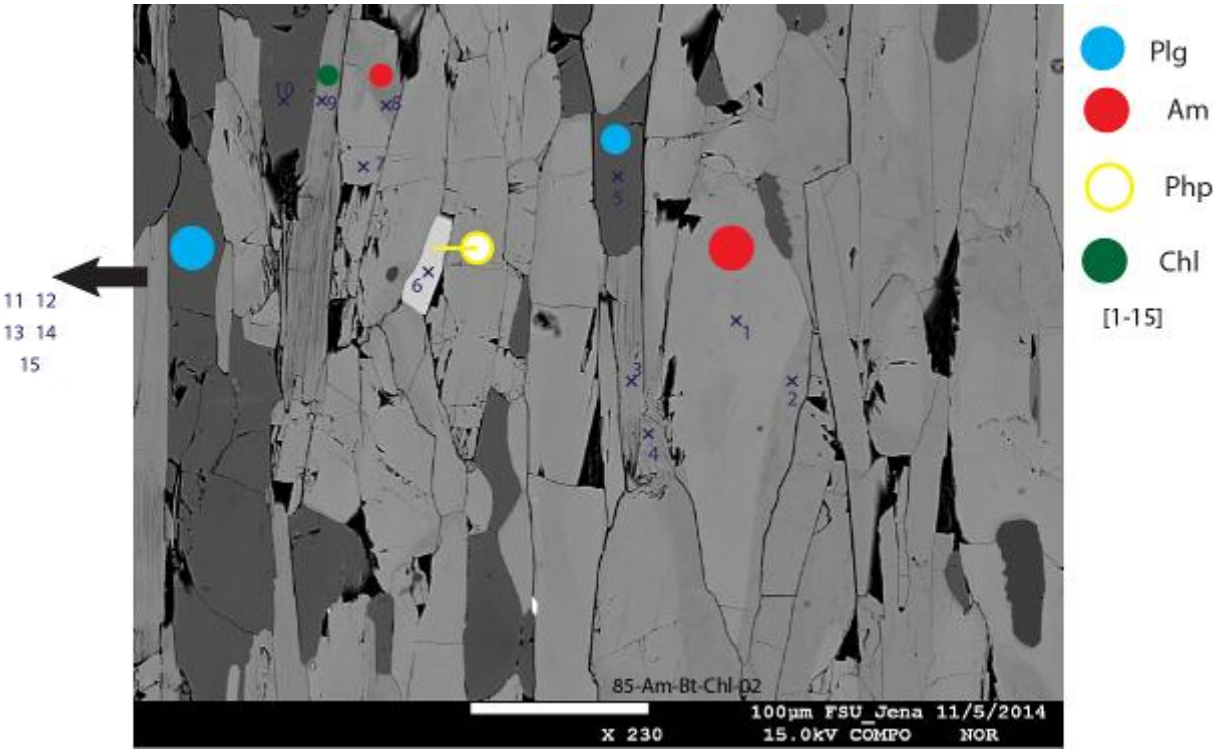

Figure 47 – BSE image of sample 85, shown to indicate the location of spot analyses [1+5] used for geothermometry with the Holland & Bundy (1994) geothermometers. Furthermore, aligned µm-scale sized crystals of hornblende coexist with chlorite and plagioclase.

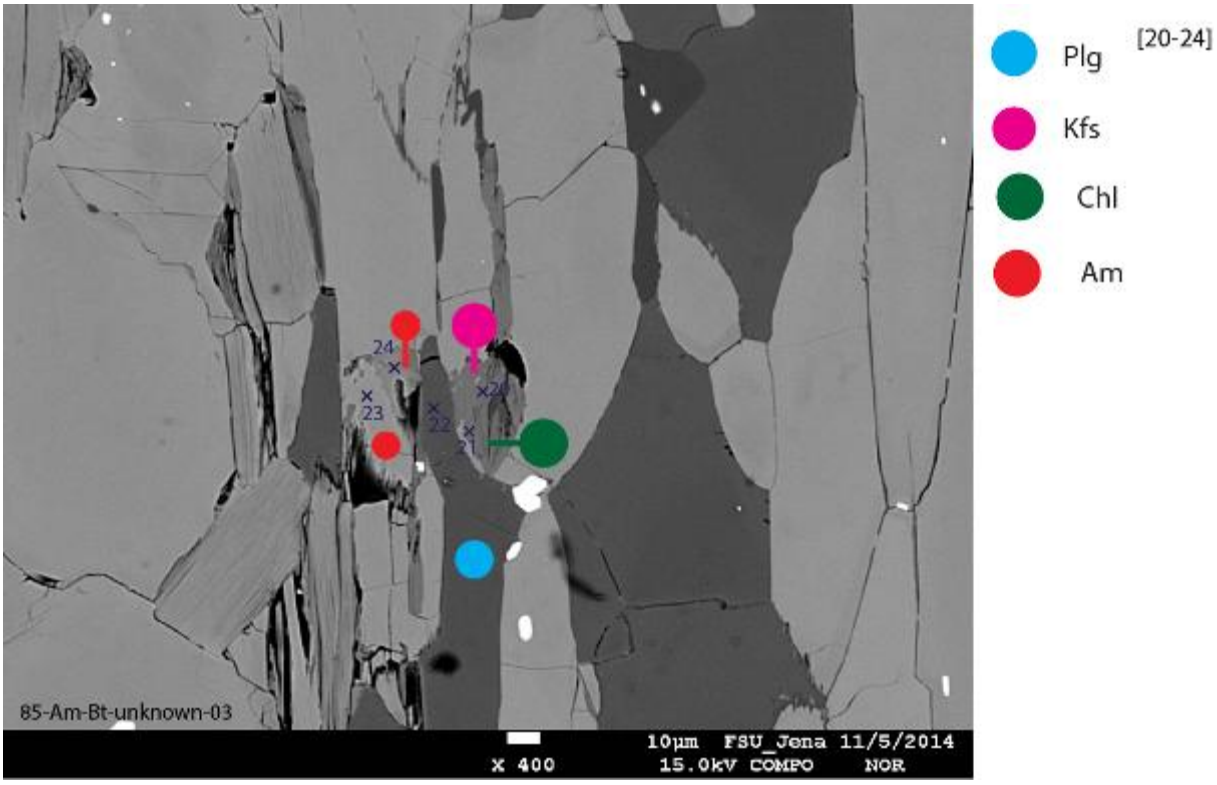

Figure 48 - Sample 85, shown to indicate the location of spot analyses [23+22] and [24+22] used for geothermometry with the Holland & Bundy (1994) geothermometers.

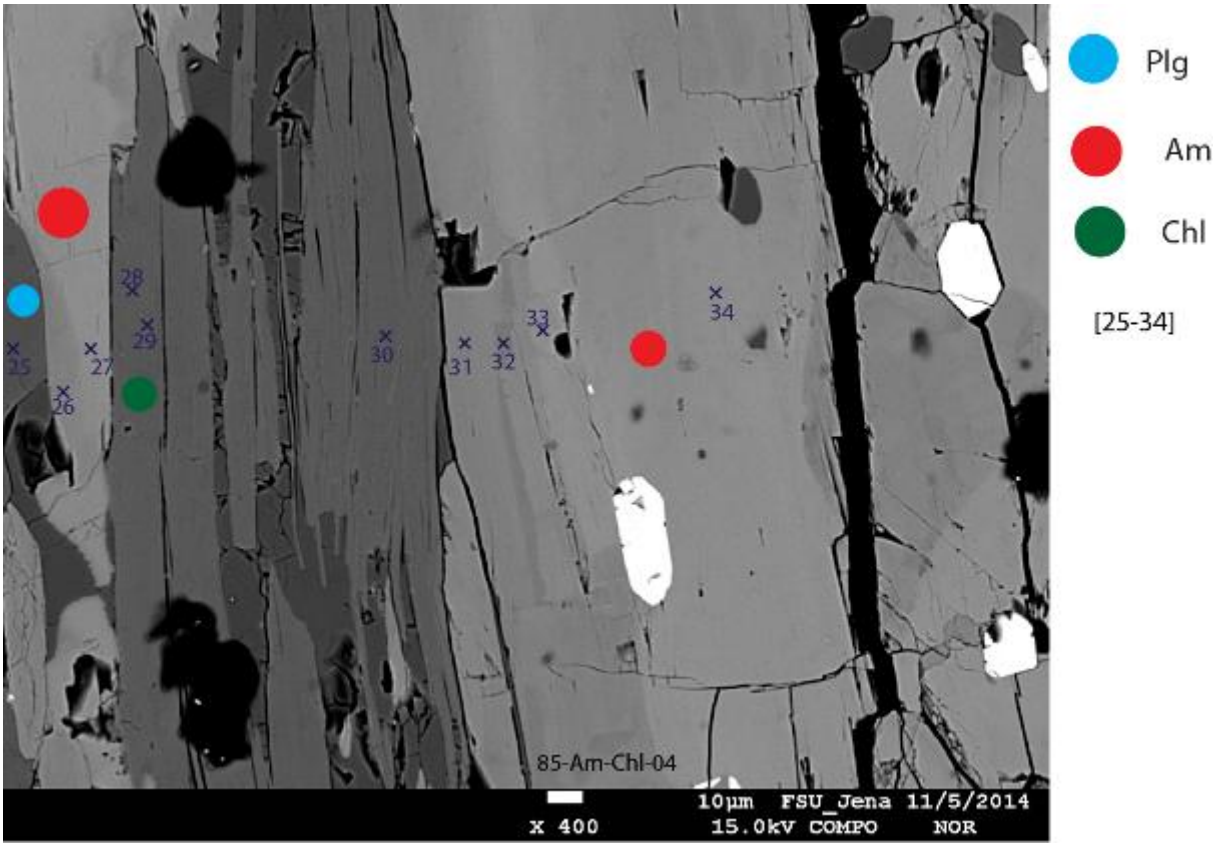

Figure 49 - Sample 85, shown to indicate the location of spot analyses [26+25] and [27+25] used for geothermometry with the Holland & Bundy (1994) geothermometers.

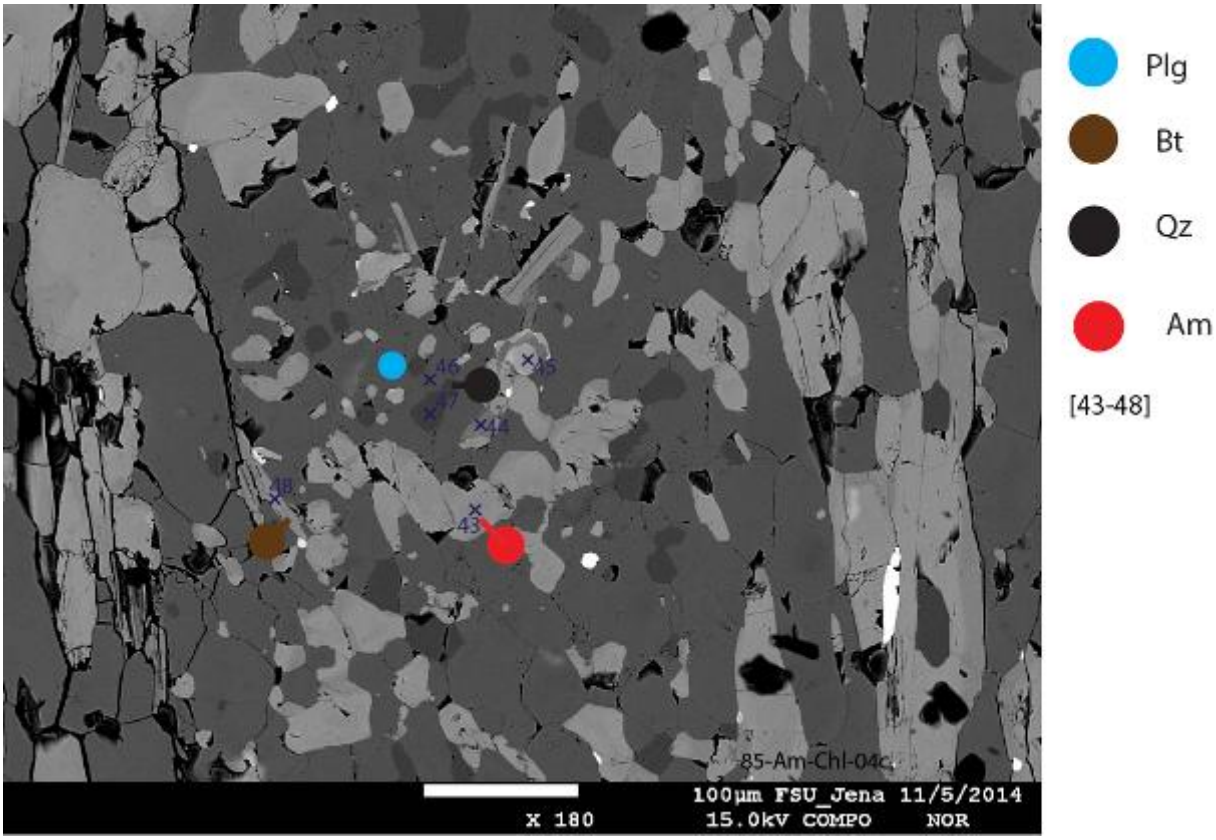

Figure 50- Sample 85, shown to indicate the location of spot analyses used [43+46] used for geothermometry with the Holland & Bundy (1994) geothermometers.

Geothermobarometry

PT diagrams have been obtained by winTWQ v. 2.32 for samples 14, 133, 167 and 23. These have been assembled below.

PT calculations have been carried out for reference P = 4kb-9kb. Assumptions regarding this range of reference pressures have been made on the basis of amphibole-plagioclase equilibrium pairs of Raeva & Cherneva (2009) from amphibolites situated in the eastern part of the Madan unit, yielding 640-720°C/0.6-1.0GPa. This range of pressures is consistent with the range of pressures determined above for 85. Using the range of reference pressures suggested, similarly a range of temperatures is obtained.

Figure 51 to 54 represent PT diagrams for sample 14, 23, 133 and 167, respectively. These have been constructed by geothermobarometric modeling, using the updated partial database of Berman & Aranovich (1996). Thermobarometric calculations for sample 23 yield higher metamorphic conditions than for sample 14. PT calculated for sample 23 is ±700-800°C for 9kb. PT calculated for sample 23 is ±500-600°C for 9kb. Expectedly, P estimations for both samples have been exaggerated, and therefore T might be exaggerated likewise. Relative temperature

differences from the samples however are useful. It is apparent that sample 23 and 167 record highest temperature and sample 14 and 133 record lowest temperature for the same reference pressure (P=9 kb).

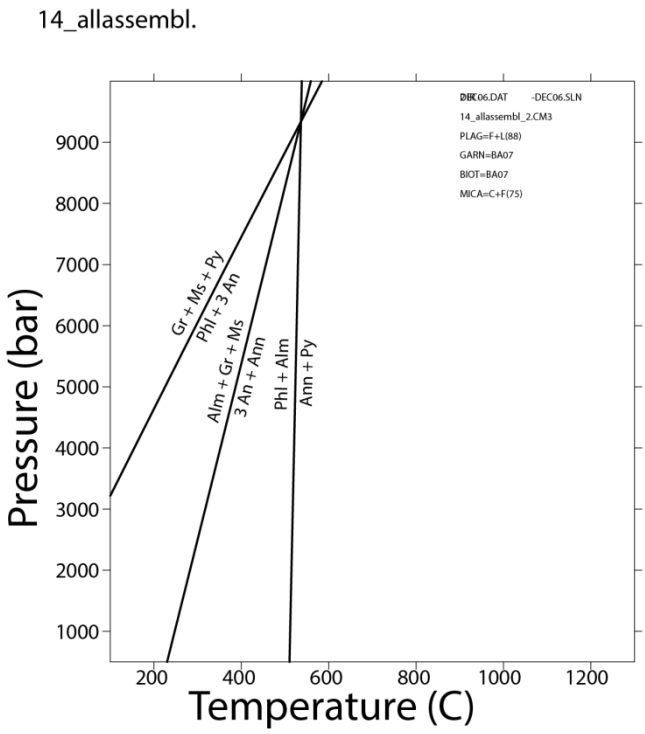

Figure 51 – PT diagram for sample 14. Obtained with the aid of TWQwin, using the update of Berman & Aranovich (1996), partial database. Sample 133 and 14 record kfs, qtz and bt. This permits using Si-content of white mica as a diagnostic for pressure (Zhu & Wei, 2007 and references therein). From phengite-in-whm barometry, it is evident that sample 14 and 133 both record highest grade (with Si-content in the range ±47-49.51). From appendix 2, it is obvious that sample 23 does not contain kfs; hence utilization of phengite-in-whm barometry is not permitted.

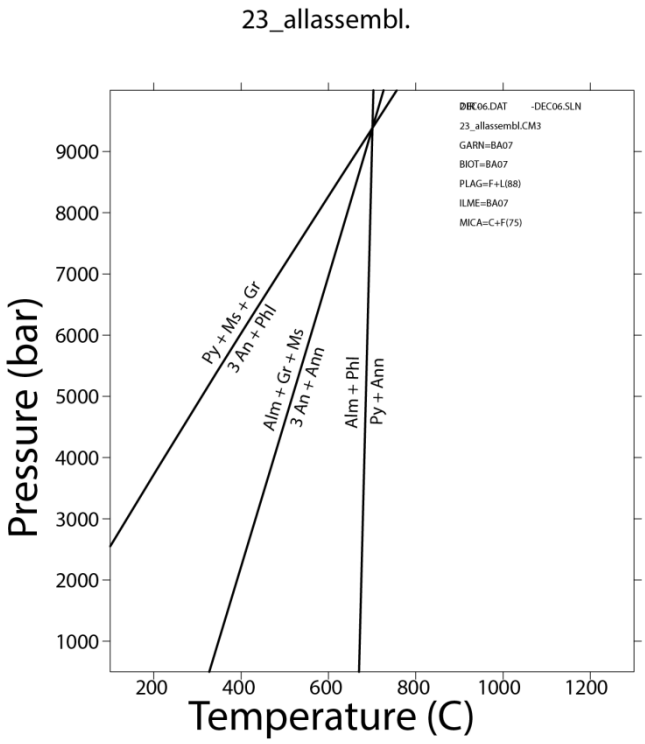

Figure 52 - PT diagram for sample 23. Obtained with the aid of TWQwin, using the update of Berman & Aranovich (1996), partial database.

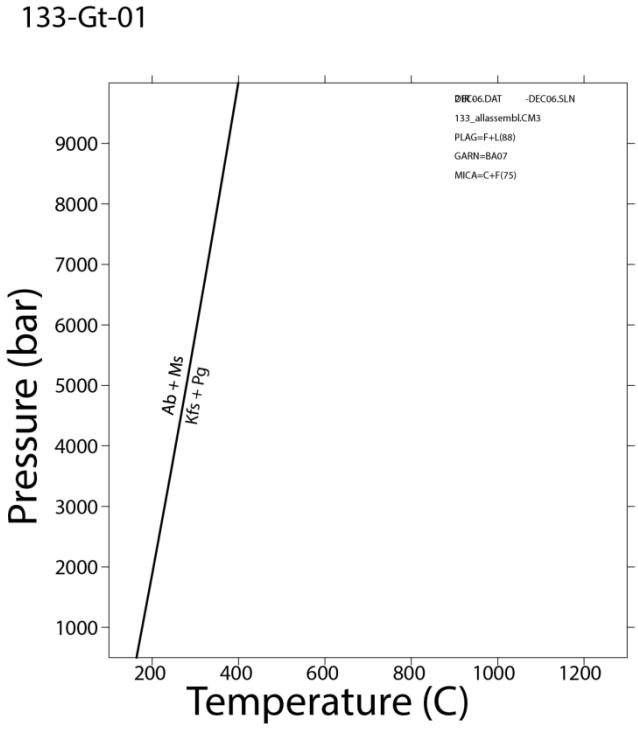

Figure 53 – PT diagram for sample 133. Obtained with the aid of TWQwin, using the update of Berman & Aranovich (1996), partial database. Sample 133 and 14 both record Kfs, qtz and bt. This permits using Si-content of white mica as a diagnostic for pressure (Zhu & Wei, 2007 and references therein). From phengite-in-Whm barometry, it is evident that sample 14 and 133 both record highest grade (with Si-content in the range ±47-49.51). From appendix 2, it is obvious that sample 23 does not contain Kfs; hence utilization of phengite-in-Whm barometry is not permitted.

Niels_167_Foto-section01

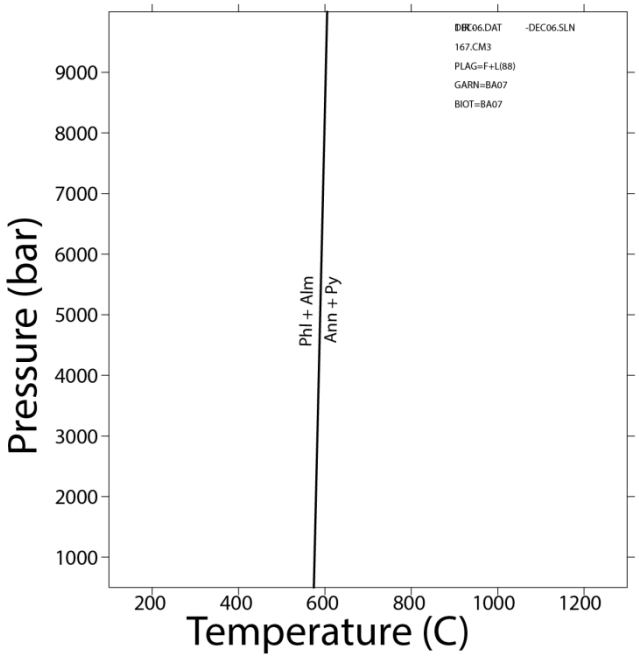

Figure 54 – PT diagram for sample 167. Obtained with the aid of TWQwin, using the update of Berman & Aranovich (1996), partial database.

5. Discussion

5.1 - Factual discussion

±S-dipping foliation with top-±S sense of shear in the Upper unit and ±S-dipping foliation with top-±N sense of shear in the Uppermost unit are related to compression and nappe stacking (D1) described earlier on pages 10-11.

±N-dipping foliation with top-±S sense of shear in the Upper unit and ±N-dipping foliation with top-±N sense of shear in the Uppermost unit are related top-±N exhumation (D2).

D3 is associated with core complex formation-related detachment and exhumation. D3 is characterized by 2 combinations of foliation dip-direction and shear sense (±S-dipping foliation with top-±N sense of shear for the Upper unit + ±S-dipping foliation with top-±S sense of shear in the Uppermost unit, ±N-dipping foliation with top-±S sense of shear for the Upper unit + ±N-dipping foliation with top-E/NE sense of shear for the Uppermost unit) and ±N-dipping foliation with top-±N sense of shear in the Upper unit. Top-±N sense of shear on a ±N-dipping foliation plane in the Bachkovo-Dobralak unit (as in figure 13) is interpreted as S-ward exhumation of the Asenitsa unit. For the Asenitsa, the tectonic response would show top-±S sense of shear on ±S-dipping foliation planes. This is however not recognized in the field.

Often, earlier structures have been modified and metamorphic features have been overprinted. For example, S-dipping (S1) foliation that is crenulated by N-dipping (S2: 05/12) foliation implies a tectonic shift, potentially from N-ward compression to exhumation (see fig. 9). Pervasive NW (313)-trending lineation for placemark 142 on a ±S dipping foliation plane in the Bachkovo-Dobralak may indicate either D1 compression or D3 extension. No definite sense of shear is associated with it. Another example is sample 23 in the Uppermost unit that records relatively high grade metamorphism, but shows inferred ±SE sense of shear with ±S-dipping foliation (characteristic for extension: D3).

Classically, top-to ±E/NE sense of shear with ±N-dipping foliation in the Uppermost unit has been related to Cenozoic extension along local detachments and subsequent exhumation. This is confirmed from field research associated with this study. Top-to ±N sense of shear in the Asenitsa has been thought to represent shortening in the Rhodope Massif. Top-to ±N(W) sense of shear is therefore considered to have incorporated a significant high-grade metamorphic imprint.

From section 1 (Infield results) of the Results, it is evident that for both the Bachkovo-Dobralak unit and Asenitsa unit these preconceptions are not always justified. Throughout the entire Bachkovo-Dobralak unit, ±N-dipping foliation with top-N shear sense has been recognized

in association with evidently low-grade metamorphic rocks (see e.g. sample 16, appendix 2.1). For the Asenitsa unit, rocks showing top-to ±N sense of shear, containing quartz that has evidently not been dynamically recrystallized, represents an example of this. Lack of dynamical recrystallization is consistent with relatively low prevailing temperature conditions.

It is therefore deemed necessary to incorporate exhumation-driven processes into the tectono-evolutionary history of the Rhodope Massif, explaining top-to ±N sense of shear in relation with low-grade metamorphic rocks.

Sample 167 (of the Asenitsa unit) records minerals (e.g. garnet and plagioclase) having a confident prograde metamorphic imprint. Examples of garnet originated in a period prior to peak metamorphism and grew coincident with prevalent prograde metamorphism (see fig. 40). It is evident that the Asenitsa unit has been influenced by D1.

Sample 23 (of the Asenitsa unit) records highest peak metamorphic conditions (T) and records minerals which appear least retrogressed. Increasing metamorphic grade for 23 has been associated with growth of examples of plagioclase crystals. Sample 23 possesses a stretching lineation that trends ±NW-SE (appendix 2.1 - Thin section description), and may have experienced top-to ±N shortening (D1).

The fact that sample 23 (former plagiogranite), located closely to the North-Rhodopean detachment fault, experienced relatively early, high grade metamorphism, may additionally account for the fact that it has possibly been enhanced by contact metamorphism of intruding magmatic bodies associated with early core-complex formation. This can also be implied from comparison between sample 14 and 133, both constituting the Bachkovo-Dobralak unit. Sample 14 (located close to the North-Rhodopean detachment fault), has recorded higher grade metamorphism than sample 133 (which is located further from the North-Rhodopean detachment fault).

Plastic flow of Kfs crystals near a contact in the Bachkovo-Dobralak confirms the fact that rocks become progressively higher temperature close by a, purely tectonic, contact.

Sample 16 shows top-to ±N(W) sense of shear, and additionally records relatively low-grade conditions (i.e. relatively large grain size of quartz and plagioclase). This may imply that sample 16 originated in a structurally relatively uplifted level and was never buried significantly (D2).

From appendix 2.2, figure 23, it appears that shear bands exist for sample 23 that suggest sense of shear in a direction parallel to the lineation plunging direction measured, which is top-to-140 (SE). Although sample 23 records highest peak metamorphic conditions (T), it also

possesses an evident retrograde metamorphic imprint. Garnet originated in a period of or close to peak metamorphism and has subsequently grown coincident with retrograde metamorphism. It is interpreted that sample 23 has been subject to early high grade metamorphic conditions, potentially as a consequence of top-to ±N shortening (D1), which has been overprinted by top-to ±S(E) sense of shear, related to Cenozoic extension and subsequent exhumation (D3). This may also be derived from the fact that earlier thrust faults have been reactivated during exhumation (Schmid *et al.,* in prep.) and trend of the lineation has thus most likely been not been significantly overprinted/enhanced.

5.2 - Interpretative Discussion

Top-to N(W) shear sense and exhumation

Figure 55 has been incorporated to suggest a mechanism for exhumation of the Bachkovo-Dobralak unit and explain top-to ±N sense of shear in association with low-grade metamorphic rocks of the Asenitsa unit.

Figure 55 graphically presents the tectonic evolution of the northern Rhodopes. A ±S-ward plane of subduction exists in (a), consequently nappes are thrust ±northward (b). Progressive stacking of nappes results in gravitational instability of the most uplifted part of the nappe stack. Top-to NW normal shearing accommodates gravitational instability in the Asenitsa unit and a significant portion of Bachkovo-Dobralak is unloaded, leaving a tectonic scarp in the process. This is interpreted as syn-orogenic extension and is thought to partly explain the observed retrograde metamorphic imprint for the Bachkovo-Dobralak unit. Ancient high-grade metamorphic characteristics are thought to have been overprinted as a consequence.

No overall horizontal stretching of the crust or lithosphere is thought to be necessary to accommodate extension.

It may be possible that retrograde metamorphism resulting from this stage of unloading also already affected rocks (14, 133) that currently possess top-to NE sense of shear, related to Cenozoic exhumation.

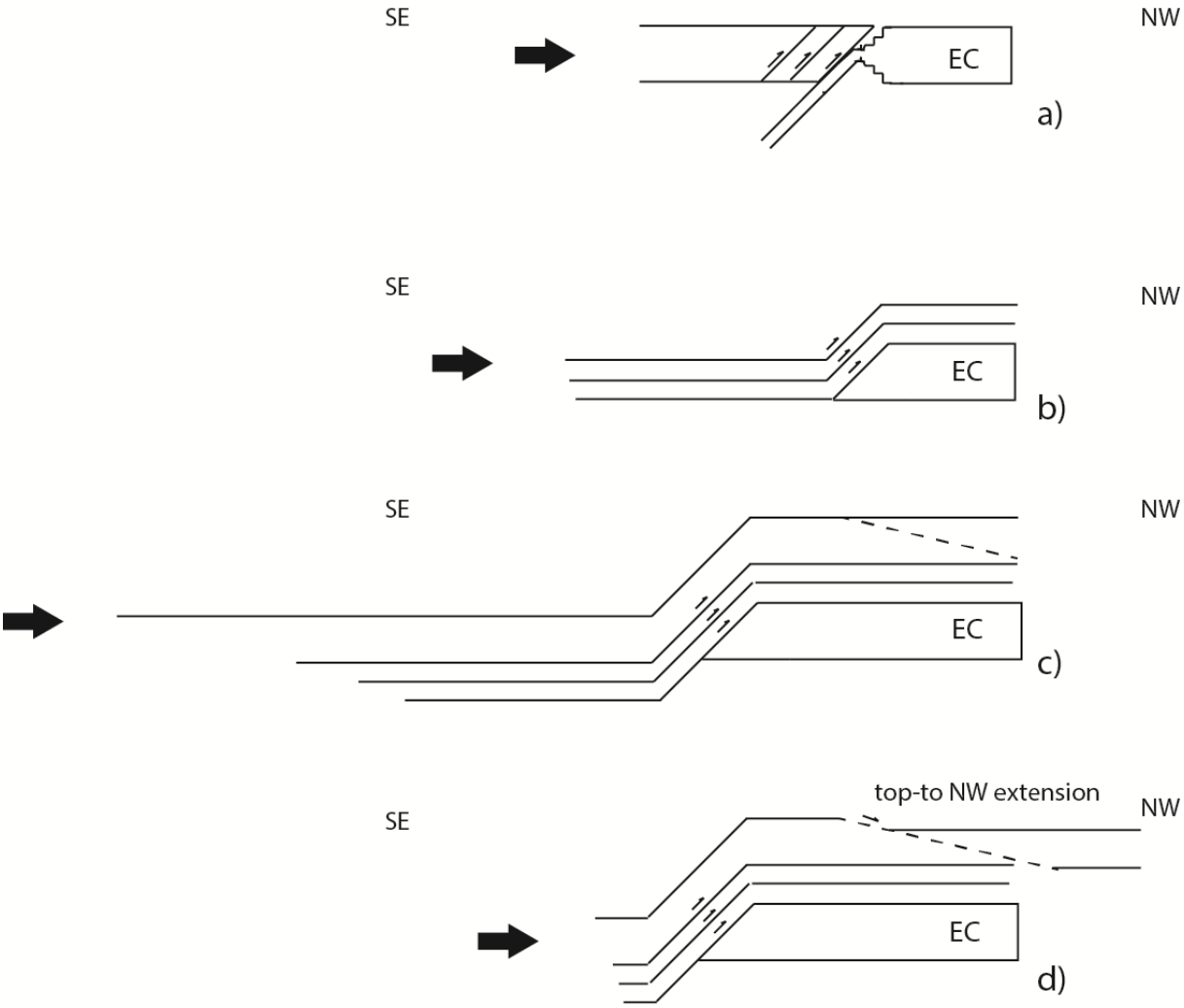

Figure 55 – Tectonic model for the northern Rhodopes suggesting a mechanism for exhumation of the Bachkovo-Dobralak unit and explaining top-to ±N sense of shear in association with low-grade metamorphic rocks of the Asenitsa unit. The stacking of nappes results in gravitational instability of the most uplifted part of the nappes. Top-to N(W) normal shearing accommodates gravitational instability and provides the observed retrograde metamorphic imprint for the Bachkovo-Dobralak unit. EC = European continental Crust. In figure c) and d) the uppermost thrust sheet has been assumed to possess great thickness and incorporate both Bachkovo-Dobralak and Asenitsa (after Ivanov, 1988 and Burg *et al.*, 1990). Infer from the text in the report that this is not thought necessary in the light of the tectono-evolutionary explanation.

Ivanov (1988) and Burg *et al.* (1990) argue that the Bachkovo-Dobralak and Asenitsa (jointly termed the tectonic unit Asenitsa), represent the uppermost thrust sheet, constituting the Central Rhodopian Dome. Gravitational instability is likely to commence in the most uplifted unit, which is assisted by conclusions of Ivanov (1988) and Burg *et al.* (1990).

An implication of this model is that the uppermost thrust sheet (Asenitsa) possesses great thickness, when a steep detachment is assumed in association with top-to NW extension, or very low-angle detachment is associated with top-to NW extension in the Asenitsa unit. Furthermore, only a very small portion of uplift (due isostatic rebound associated with to core-

complex formation) is required to have subsequently been accomplished, so that not a significantly large portion of Asenitsa is displaced as a consequence of Cenozoic extension.
Note that further discussion does not necessarily assume that both the Bachkovo-Dobralak and Asenitsa are part of a single, uppermost, thrust sheet.

Complete tectono-metamorphic evolution model

Figure 56 indicates the northern Rhodopes tectono-metamorphic evolution incorporating nappe-stacking (a), top-to N(W) detachment and subsequent unloading of the Bachkovo-Dobralak unit (b-c), and core-complex formation (e-g). The approximate interpreted pathways for samples 167, 23, 14 and 133 have been indicated. It incorporates the suggested prograde path for sample 167, peak metamorphism for sample 23 and direct exhumation for samples 14 and 133.

It is considered that rocks from the Bachkovo-Dobralak unit that once originated as granite experienced mostly retrograde metamorphism, as they were possibly only uplifted from their original position, onwards. This may imply that these rocks were quickly unloaded after nappe stacking and exhumed relatively rapidly. Rocks from the Bachkovo-Dobralak unit have been metamorphosed relatively shallow within the earth. Rocks from the bordering Asenitsa unit have been buried for a significantly extended period even though these rocks originated in a tectonically/stratigraphic more elevated position. The latter rocks therefore experienced less retrogression.

By separating the Bachkovo-Dobralak from the Asenitsa, it is assumed that the Bachkovo-Dobralak does not form part of an uppermost thrust sheet (after Ivanov, 1988 and Burg *et al.*, 1990), because it represents basement and is thus likely to have originated in a structurally lower position.

According to this model, Asenitsa was buried for a longer period and experienced prograde metamorphism for an extended amount of time. Therefore it does not possess such a significant retrograde metamorphic imprint as Bachkovo-Dobralak, and even records ancient prograde metamorphism.

In e), sample 167 is subject to only a minor amount of uplifting (or none at all) for it is mainly displaced laterally, in contrast to samples 14, 133 (and 23) and therefore, it records prograde metamorphism most clearly, even though it records top-to NE, exhumation-related sense of shear.

Sample 23 records highest metamorphic grade for it has still been buried for a significant period (and deeper than 167).

Sample 133 (located in the centre of the dome) is exhumed at highest rate and has recorded greatest retrograde metamorphism. Sample 14 (located at the edge of the dome) is still exhumed at high rate, but remains close to the tectonic contact, separating it from the overlying Asenitsa. Therefore it possibly still records high-grade metamorphic characteristics.

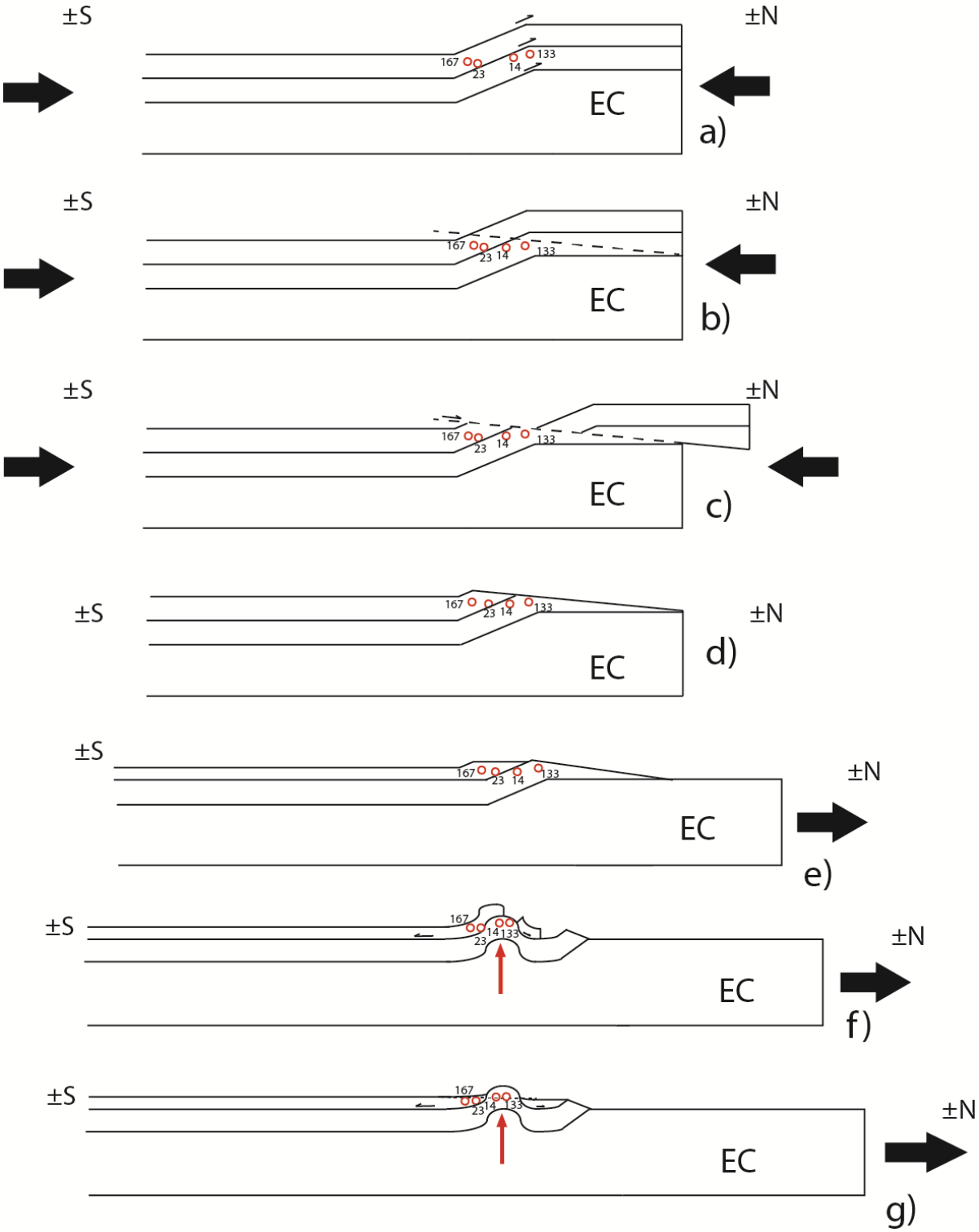

Figure 56 – The complete tectono-metamorphic evolution model for the northern Rhodopes, incorporating the approximate interpreted pathways for samples 167, 23, 14 and 133. A significant portion of Asenitsa has been displaced in a northeastward direction along local detachments as a consequence Cenozoic extension. This is not clearly evident from the figure, which implies that a fixed separation is present, displacing rocks towards the ±N and ±S. I would like to clarify that also rock of Asenitsa to the south of the dome record top-to NE sense of shear. The model incorporates two individual thrust sheets: the lower Bachkovo-Dobralak and the upper Asenitsa. Note that this does not imply that structurally deeper thrust sheets are absent. The dotted line in g) implies erosion, exposing the rock samples.

The driving mechanism for extension and core-complex formation in figure 56e-g is thought to be related to post-orogenic, slab-rollback driven extension (as illustrated in figure 57). It is considered that syn-orogenic gravitational collapse of the Asenitsa has provided a minor, initial means of extension, as the Bachkovo-Dobralak was unloaded which may have been uplifted to a minor extent as a consequence of isostatic rebound. Adjacent rocks from the Asenitsa unit may have been displaced laterally, as a response.

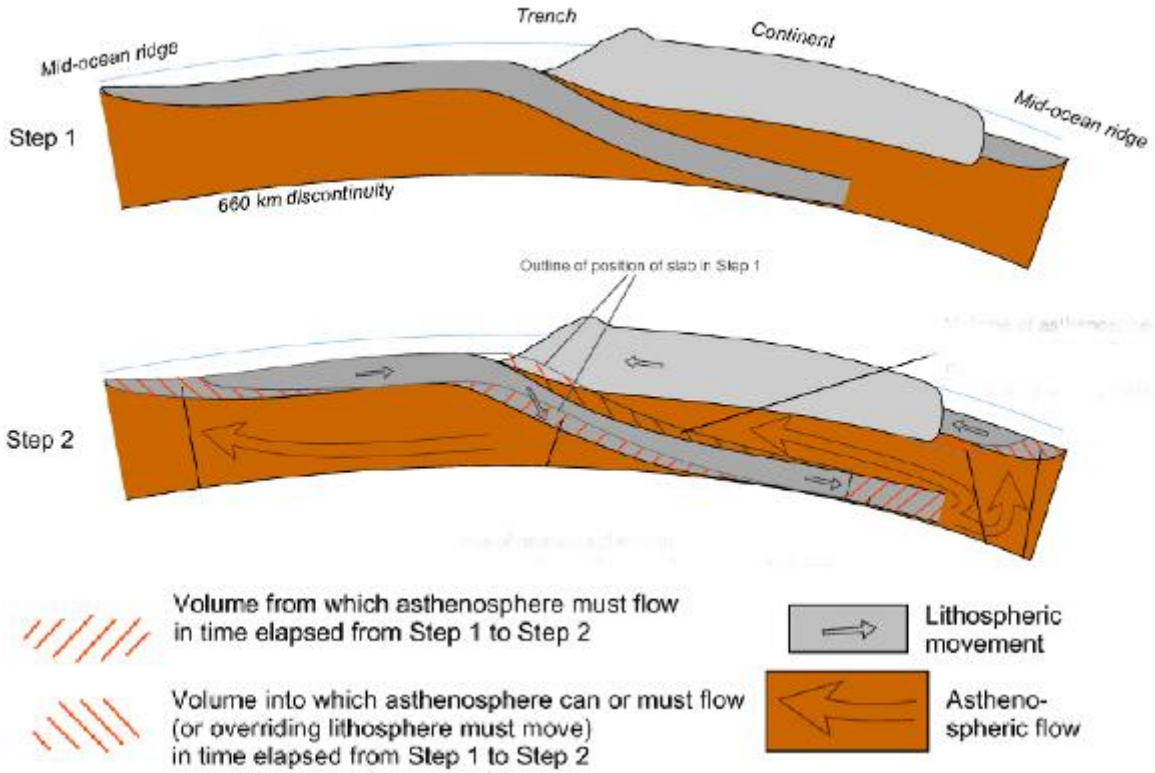

Figure 57 – Representation of the concept of slab-rollback. The legend is provided below the configuration. The 660 km discontinuity, indicated in the upper configuration, is not necessarily supported by the incorporation of this image, but is indicated merely as a means to limit the size of the diagram. After Railsback (2006).

An implication of the model shown in figure 56 is that a metamorphic gradient exists in the Bachkovo-Dobralak. In the North, the Bachkovo-Dobralak may likely record highest grade metamorphism, because these rocks have originally been buried deepest. This may be disproved by rocks that have been metamorphosed to a greater degree as a consequence of contact metamorphism on the southern edge of the North-Rhodopean detachment fault.

In the model, sample 133 has been provided with the greatest initital depth. Therefore, the implication exists that all (or most) high-grade characteristics of sample 133 are completely overprinted by retrograde metamorphism. Complete retrograde overprinting of the (originally higher grade) Bachkovo-Dobralak is thought to be unlikely. This model succeeds to explain the observed metamorphic paradox for the Bachkovo-Dobralak and Asenitsa, but fails to explain

why, according to our observations, no confident high-grade metamorphic characteristics have been preserved in the Bachkovo-Dobralak, even though it is evident that Bachkovo-Dobralak records N-ward thrusting, from a structural geological point of view (see fig. 21). Potentially, Bachkovo-Dobralak has at no instant been subject to prograde metamorphism (because top-to NW detachment commenced quickly after stacking of Bachkovo-Dobralak). It remains however inexplicable that no evidence of a high-grade protolith of Bachkovo-Dobralak can be traced.

Initial exhumation of the Asenitsa unit in 56f is characterized by top-S sense of shear on N-dipping foliation planes. This has however not been identified in the field because the exhumed portion of Asenitsa is now completely transported toward the south and its foliation has been tilted S-ward as a consequence.

In general, sections transported as a consequence of post-orogenic extension-related detachment in figure 56f&g, have recorded a significant component of stretching along the strike of foliation (figure 23). Likely, sections that were originally located at the edge of the uplifted dome and occupied a topographically lower position have trends of lineation parallel to strike of foliation. Sections that have been transported from the top of the dome would have trends of lineation at an angle to the strike of foliation.

6 - Conclusions

- The existing views on the tectonometamorphic evolution of the northern Rhodopes are confirmed by this study. ±N-dipping foliation with top-N shear sense in association with evidently low-grade metamorphic rocks both in the Bachkovo-Dobralak and Asenitsa units form significant additions to the history of the northern Rhodopes. Top-to ±N extension in the Asenitsa unit and subsequent exhumation of the Bachkovo-Dobralak unit is related to the gravitational instability of a nappe stack. ±N-dipping foliation with top-N shear sense in the Bachkovo-Dobralak is related to the exhumation of the entire Rhodope (associated with core-complex formation).
- The rate and timing of exhumation appears to have played significant part in the variations of metamorphic grade recorded by rocks from the Bachkovo-Dobralak and Asenitsa units. Prograde characteristics of rocks that were quickly brought back to the surface have largely been overprinted by retrograde metamorphism. Rocks that were largely transported laterally instead of directly upward record higher grade metamorphism.
- Burial residence time appears to have played significant part in maintaining ancient prograde metamorphic characteristics for samples that have obviously been enhanced by retrograde metamorphism. Rocks that have been buried for an extended period have kept their prograde metamorphic characteristics, whereas rapidly unloaded rocks solely record retrograde characteristics.
- The presence of a metamorphic gradient in the Bachkovo-Dobralak of progressively higher grade metamorphism towards the north may confirm the tectono-metamorphic evolution model suggested for the northern Rhodopes in this report, explaining top to ±N, syn-orogenic extension in the Asenitsa unit. On top of the ±N-dipping detachment, rocks exposed in the northern part of the Bachkovo-Dobralak unit have likely been located deeper than rocks in the southern part of the Bachkovo-Dobralak unit (see figures 53c,d and 54b,c).
- Top-to ±N detachment associated with gravitational instability may have guided the formation of late Eocene extensional basins to the north of the Rhodopes (i.e. the Plovdiv Basin).
- Separation of the Bachkovo-Dobralak from the Asenitsa (as suggested by Burg, 2011) is supported by this study.

7 - References

Avigad, D. & Garfunkel, Z. (1998). Low-angle faults above and below a blueschist belt – Tinos Island, Cyclades, Greece. Terra Nova, 1(2), 182-187.

Avigad, D., Garfunkel, Z., Jolivet, L. & Azanon, J. M. (1997). Back arc extension and denudation of Mediterranean ecogites. Tectonics, 16(6), 924-941.

Barbieri, M., Caggianelli, A., Di Florio, M. R. & Lorenzoni, S. (1994). Plagiogranites and gabbroic rocks from the Mignora ophiolitic mélange, Swat Valley, NW Frontier Province, Pakistan. Mineralogical Magazine, 58, 564.

Berman, R. G. (1991). Thermobarometry using multi-equilibrium calculations: a new technique, with petrological applications. *Canadian Mineralogist*, *29*(4), 833-855.

Berman, R. G., & Aranovich, L. Y. (1996). Optimized standard state and solution properties of minerals. *Contributions to Mineralogy and Petrology*, *126*(1-2), 1-24.

Berman, R. G., Aranovich, L. Y., Rancourt, D. G., & Mercier, P. (2007). Reversed phase equilibrium constraints on the stability of Mg-Fe-Al biotite. *American Mineralogist*, *92*.

Bonev, N., & Beccaletto, L. (2007). From syn-to post-orogenic Tertiary extension in the north Aegean region: constraints on the kinematics in the eastern Rhodope–Thrace, Bulgaria–Greece and the Biga Peninsula, NW Turkey. *Geological Society, London, Special Publications*, *291*(1), 113-142.

Bonev, N., Burg, J. -P. & Ivanov, Z. (2006a). Mesozoic-Tertiary structural evolution of an extensional gneiss dome – the Kesebir-Karadamos dome, eastern Rhodope (Bulgaria-Greece). International Journal of Earth Sciences, 95(2), 318-340.

Bonev, N.G., Stampfli, G.M., 2003. New structural and petrologic data on Mesozoic schists in the Rhodope (Bulgaria): geodynamic implications. C. R. Geosci. 335, 691–699.

Brichau, S., Ring, U., Carter, A., Monie, P., Bolhar, R., Stockli, D. & Brunel, M. (2007). Extensional faulting on Tinos island, Aegean sea, Greece: How many detachments? Tectonics, 26(4), 19.

Brichau, S., Ring, U., Ketcham, R. A., Carter, A., Stockli, D. & Brunel, M. (2006). Constraining the long-term evolution of the slip rate for a major extensional fault system in the central Aegean, Greece, using thermochronology. Earth and Planetary Science Letters, 241 (1-2), 293-306.

Brun, J. -P. & Facenna, C. (2008). Exhumation of high-pressure rocks driven by slab rollback. Earth and Planetary Science Letters, 272(1-2), 1-7.

Brun, J. -P. & Sokoutis, D. (2007). Kinematics of the southern rhodope core complex (north Greece). International Journal of Earth Sciences, 96(6), 1079-1099.

Btbien J., L'association ignee de Guevgueli. ofioliti, 8(3)
(1983) 293-302.

Buick, I.S. (1991). The late Alpine evolution of an extensional shear zone, Naxos, Greece. Journal of the Geological Society, 148, 93-103

Buick, I. S. & Holland, T. (189). The P-T-t path associated with crustal extension, Naxos, Cyclades, Greece. In Daly, J.S.; Cliff, R. A.; Yardly, B. W. D., editors, Evolution of Metamorphic Belts, volume 43, 365-369. Geological Society, London, Special Publications.

Burchfiel, B. C., Nakov, R., & Tzankov, T. (2003). Evidence from the Mesta half-graben, SW Bulgaria, for the Late Eocene beginning of Aegean extension in the Central Balkan Peninsula. *Tectonophysics*, *375*(1), 61-76.

Burg, J. -P. (2011). Rhodope: From Mesozoic convergence to Cenozoic extension. Review of petro-structural data in the geochronological frame. Journal of the Virtual Explorer. In: (Eds.) Emmanuel Skourtsos and Gordon S. Lister, Journal of the Virtual Explorer, 39, paper 1. doi: 10.3809/jvirtex.2011.00270-

Burg, J. -P., Godfriaux, I. & Ricou, L. E. (1995). Extension of the Mesozoic Rhodope thrust units in the Vertiskos Kerdillion Massifs (northern Greece). *Comptes Rendus De L'Academie Des Sciences Paris*, 320(9), 889-896.

Burg, J. -P., Ivanov, Z., Ricou, L. -E., Dimor, D. & Klain, L. (1990). Implications of shear-sense creteria for the tectonic evolution of the Cebtral Rhodope massif, southern Bulgaria. Geology, 18, 451-454.

Burg, J. -P., Klain, L., Ivanov, Z., Ricou, L. E. & Dimov, D. (1996a). Crustal-scale, thrust complex in the rhodope massif. Evidence from structures and fabrics. In *The ocean basins and margins*, 8, 125-149.

Burg, J.-P., Ricou, L. E., Ivanov, Z., Godfriaux, I., Dimov, D. & Klain, L. (1996b). Syn-metamorphic nappe complex in the Rhodope Massif. Structure and kinematics. Terra Nova, 8(1), 6-15.

Chemenda, A. I., Mattauer, M., Malavieille, J., & Bokun, A. N. (1995). A mechanism for syn-collisional rock exhumation and associated normal faulting: results from physical modelling. *Earth and Planetary Science Letters*, *132*(1), 225-232.

Coleman, R.G. & Peterman, Z. E. (1975). Oceanic plagiogranite. *Journal of Geophysical Research (Solid Earth and Planets)*, 80 (8), 1099-1108

Coney, P. J. (1987). The regional tectonic setting and possible causes of Cenozoic extension in the North American Cordillera. *Geological Society, London, Special Publications*, *28*(1), 177-186.

de Capitani C. & Petrakakis K. (2010). The computation of equilibrium assemblage diagrams with Theriak/Domino software. *American Mineralogist*, 95:1006-1016

Dinter, D. A. (1998). Late Cenozoic extension of the Alpine collisional orogen, northeastern Greece: origin of the north Aegean basin. *Geological Society of America Bulletin*, *110*(9), 1208-1230.

Dinter, D. A. & Royden, L. (1993). Late Cenozoic extension in northeastern Greece – Strymon Valley detachment system and Rhodope Metamorphic Core Complex. Geology, 21(1), 886-908.

Dixon, J. E. & Dimitriadis, S. (1984). Metamorphosed ophiolitic rocks from the Serbo-Macedonian Massif, near Lake Volvi, North-east Greece, *Spec. Publ. Gwl. Soc. London,* 17, 603-618.

Ferrière, J. Reynaud, J. Y., Pavlopoulos, A., Bonneau, M., Mitgos, G., Chanier, F., Proust, J. N. & Gardin, S. (2004). Geologic evolution and geodynamic controls of the Tertiary intramontane piggyback Meso-Hellenic basin, Greece. Bulletin De La Societe Geologique De France, 175(4), 361-381

Froitzheim, N., Jahn-Awe, S., Frei, D., Wainwright, A. N., Maas, R., Georgiev, N., ... & Pleuger, J. (2014). Age and composition of meta-ophiolite from the Rhodope Middle Allochthon (Satovcha, Bulgaria): A test for the maximum-allochthony hypothesis of the Hellenides. *Tectonics*, *33*(8), 1477-1500.

Gautier, P., & Brun, J. P. (1994). Crustal-scale geometry and kinematics of late-orogenic extension in the central Aegean (Cyclades and Ewia Island). *Tectonophysics*, *238*(1), 399-424.

Gautier, P., Brun, J. -P., & Jolivet, L. (1993). Structure and kinematics of Upper Cenozoic extensional detachment on Naxos and Paros (Cyclades Islands, Greece). Tectonics, 12(5), 1180-1194.

Georgiev, N., Pleuger, J., Froitzheim, N., Sarov, S., Jahn-Awe, S., & Nagel, T. J. (2010). Separate Eocene–Early Oligocene and Miocene stages of extension and core complex formation in the Western Rhodopes, Mesta Basin, and Pirin Mountains (Bulgaria). *Tectonophysics*, *487*(1), 59-84.

Gerdjikov, I. (2004). High-strain greenschist belt along the margins of the Central Rhodopes. In Bulgarian Geological Society, Annual Scientific Conferences, 24-26.

Godfriaux, 1965

Görür, N., & Okay, A. I. (1996). A fore-arc origin for the Thrace Basin, NW Turkey. *Geologische Rundschau*, *85*(4), 662-668.

Guiraud, R., & Maurin, J. C. (1992). Early Cretaceous rifts of Western and Central Africa: an overview. *Tectonophysics*, *213*(1), 153-168.

Helgeson H.C., Kirkham D. H., and Flowers G. C. (1981) Theoretical prediction of the thermodynamic behavior of aqueous electro- lytes at high pressures and temperatures: IV. Calculation of activ- ity coefficients, osmotic coefficients, and apparent molal and stan- dard and relative partial molal properties to 600°C and 5 kbar. Amer. J. Sci. 281, 1249-1516.

Holland, T. & Bundy, J. 1994. Non-ideal interactions in calcic amphiboles and their bearing on amphibole-plagioclase thermometry. CONTRIB MINERAL PETROL, 116, 433-47.

Ivanov, Z. (1988). Aperçu général sur l'évolution géologique et structurale du massif des Rhodopes dans le cadre des Balkanides: Société Géologique de France, Bulletin, 8, 227-240.

Ivanov, Z., Dimov, D., & Sarov, S. (2000). Tectonic position, structure and tectonic evolution of Rhodope massif. In *Guide to Excursion B. ABCD–GEODE Workshop, Borovets* (pp. 1-5).

Jahn-Awe, S., Froitzheim, N., Nagel, T. J., Frei, D., Georgiev, N., & Pleuger, J. (2010). Structural and geochronological evidence for Paleogene thrusting in the western Rhodopes, SW Bulgaria: Elements for a new tectonic model of the Rhodope Metamorphic Province. *Tectonics*, *29*(3).

Jansen, J. B. H., & Schuiling, R. D. (1976). Metamorphism on Naxos; petrology and geothermal gradients. *American Journal of Science*, *276*(10), 1225-1253.

Jolivet, L., Daniel, J. M., Truffert, C., & Goffé, B. (1994). Exhumation of deep crustal metamorphic rocks and crustal extension in arc and back-arc regions. *Lithos*, *33*(1), 3-30.

Jolivet, L., Goffe, B., Monie, P., Truffert-Luxey, C., Patriat, M. & Bonneau, M. (1996). Miocene detachment in Crete and exhumation P-T-t paths of high-pressure metamorphic rcks. Tectonics, 15(6), 1129-1153 .

Jolivet, L., Lecomte, E., Huet, B., Denèle, Y., Lacombe, O., Labrousse, L., ... & Mehl, C. (2010). The north cycladic detachment system. *Earth and Planetary Science Letters*, *289*(1), 87-104.

Jolivet, L., Rimmele, G., Oberhansli, R., Goffe, B. & Candan, O. (2004). Correlation of syn-orogenic tectonic and metamorphic events in the Cyclades, the Lycian nappes and the Menderes massif. Geodynamic implications. Bulletin de la Society Geologique de France, 175(3), 217-238.

Kilias, A., Falalakis, G., & Mountrakis, D. (1999). Cretaceous–Tertiary structures and kinematics of the Serbomacedonian metamorphic rocks and their relation to the exhumation of the Hellenic hinterland (Macedonia, Greece). *International Journal of Earth Sciences*, *88*(3), 513-531.

Kockel, F., & Walther, H. W. (1965). Die Strimonlinie als Grenze zwischen Serbo-Mazedonischem und Rila-Rhodope-Massiv in Ost-Mazedonien. *Geol. Jahrb*, *83*, 575-602.

Kounov, A., Seward, D., Bernoulli, D., Burg, J. P., & Ivanov, Z. (2004). Thermotectonic evolution of an extensional dome: the Cenozoic Osogovo–Lisets core complex (Kraishte zone, western Bulgaria). *International Journal of Earth Sciences*, *93*(6), 1008-1024.

Kounov, A., Seward, D., Burg, J. P., Bernoulli, D., Ivanov, Z., & Handler, R. (2010). Geochronological and structural constraints on the Cretaceous thermotectonic evolution of the Kraishte zone, western Bulgaria. *Tectonics*, *29*(2).

Kozhoukharov, D. (1984a,b). Litostratigraphy of Precambrian metamorphic rocks of the Rhodope Supergroup in the Central Rhodopes. Geologica Balcanica, 14, 1, 43–92 (in Russian)

Krenn, K., Bauer, C., Proyer, A., Klötzli, U., & Hoinkes, G. (2010). Tectonometamorphic evolution of the Rhodope orogen. *Tectonics*, *29*(4).

Krohe, A., & Mposkos, E. (2002). Multiple generations of extensional detachments in the Rhodope Mountains (northern Greece): evidence of episodic exhumation of high-pressure rocks. *SPECIAL PUBLICATION-GEOLOGICAL SOCIETY OF LONDON*, *204*, 151-178.

Kronberg, P. (1969) Gliederung, Petrographie und Tektogenese des Rhodopen-Kristallins im Tsal-Dag, Simvolon und Ost-Pangäon (Griechisch-Makedonien), *Geotekt. Forsch.,* 31, 1-49.
Kronberg, P.**,** Meyer, W. & Pilger A. (1970). Geologie der Rila-Rhodope-Masse zwischen Strimon und Nestos (Nordgriechenland), Beiheffe Geol. Jb., 88, 133-180.

Le Pichon, X., Lallemant, S. J., Chamot-Rooke, N., Lemeur, D., & Pascal, G. (2002). The Mediterranean Ridge backstop and the Hellenic nappes. *Marine Geology*, *186*(1), 111-125.

Liati, A. (2005). Identification of repeated Alpine (ultra) high-pressure metamorphic events by U–Pb SHRIMP geochronology and REE geochemistry of zircon: the Rhodope zone of Northern Greece. *Contributions to Mineralogy and Petrology*, *150*(6), 608-630.

Liati, A., Mposkos, E. & Perdikatsis, V. (1990). Geochemical constraints on the nature and tectonic setting of the metabasite protoliths from the Rhodope zone, N Greece. Ber. Deutsch. Mineral. Gesellschaft, 1, 162.

Liati, A., Gebauer, D. & Fanning, C. M. (2004). The duration of exhumation processes in (U)HP terranes – a geochronological approach applied to the Rhodope terrane, N Greece. *'Geoscience Africa 2004', The Birth and Growth of Continents, Abstract volume*, 1, 384-385.

Lips, A. L. W., White, S. H. & Wijbrans, J. R. (2000). Middle-Late Alpine thermotectonic evolution of the southern Rhodope Massif, Greece, Geodinamica Acta, 13(5), 281-292.

Lister, G. S., Banga, G., & Feenstra, A. (1984). Metamorphic core complexes of Cordilleran type in the Cyclades, Aegean Sea, Greece. *Geology*, *12*(4), 221-225.

Lister, G., & Forster, M. (2009). Tectonic mode switches and the nature of orogenesis. *Lithos*, *113*(1), 274-291.

personal communication Liviu Matenco and Neven Georgiev

Mercier, 1968

Meyer, W. (1968). Alterstellung des Plutonismus im Sdteil der Rila-Rhodope-Masse, *Geol. Palhont., 2,* 173-192.

Mposkos, E. D., & Kostopoulos, D. K. (2001). Diamond, former coesite and supersilicic garnet in metasedimentary rocks from the Greek Rhodope: a new ultrahigh-pressure metamorphic province established. *Earth and Planetary Science Letters*, *192*(4), 497-506.

Mposkos, E., Papadopoulos, P. & Perdikatsis, B. (1989). The Rhodope crystalline basement east of Komotini, *Bull. Geol. SOC. Greece*, 20 (2), 259-273.

Naydenov, K., Peytcheva, I., von Quadt, A., Sarov, S., Kolcheva, K., & Dimov, D. (2013). The Maritsa strike-slip shear zone between Kostenets and Krichim towns, South Bulgaria—Structural, petrographic and isotope geochronology study. *Tectonophysics*, *595*, 69-89.

Okay, A. L., Satır, M., Tüysüz, O., Akyüz, S., & Chen, F. (2001). The tectonics of the Strandja Massif: late-Variscan and mid-Mesozoic deformation and metamorphism in the northern Aegean. *International Journal of Earth Sciences*, *90*(2), 217-233.

Olfert, N.C. (2014). An investigation of the origin of multi-phase solid inclusions within minerals of the Friningen garnet peridotite, N. Jämtland, central Sweden.

Perraki, M., Proyer, A., Mposkos, E., Kaindl, R., & Hoinkes, G. (2006). Raman micro-spectroscopy on diamond, graphite and other carbon polymorphs from the ultrahigh-pressure metamorphic Kimi Complex of the Rhodope Metamorphic Province, NE Greece. *Earth and Planetary Science Letters*, *241*(3), 672-685.

Pleuger J, Georgiev N, Jahn-Awe S, Froitzheim N, Valkanov N (2011) Kinematics of Palaeogene low-angle extensional faults and basin formation along the eastern border of the Central Rhodopes (Bulgaria). *Z dt Ges Geowiss*, 162:171–192

Putnis, A. (1992). *An introduction to mineral sciences*. Cambridge University Press.

Raeva, E. & Cherneva, Z. 2009. Metamorphic grade of the Madan unit in the southern part of the Central Rhodopes, Bulgaria. Geochemistry, Mineralogy and Petrology Sofia, 47, 135-161.

Railsback, L.B. (2006). Some Fundamentals of Mineralogy and Geochemistry. www.gly.uga.edu/railsback/FundamentalsIndex.html.

Ricou, L. E. (1994). Tethys reconstructed – Plates, continental fragments and their boundaries since 260 Ma from Central-America to south-eastern Asia. *Geodinamica Acta*, 7(4), 169-218.

Ricou, L. E., Burg, J.-P., Godfriaux, I. & Ivanov, Z. (1998). Rhodope and vardar: the metamorphic and the olistostromic paired belts related to the Cretaceous subduction under Europe. Geodinamica Acta, 11(6), 285-309.

Ring, U., Glodny, J., Will, T. & Thomson, S. (2007a). An Oligocene extrusion wedge of blueschist-facies nappes on Evia, Aegean Sea, Greece: implications for the early exhumation of high-pressure rocks. Journal of the Geological Society, 164(3), 637-652.

Ring, U., Will, T., Glodny, J., Kumerics, C., Gessner, K., Thomson, S., Gungor, T., Monic, P., Okrusch, M. & Druppel, K. (2007b). Early exhumation of high-pressure rocks in extrusion wedges: Cycladic blueschist unit in the eastern Aegean, Greece, and Turkey. Tectonics, 26(2).

Sarov, S., Cherneva, Z., Kolcheva, K., Voinova, E. & Gerdjikov, I. (2004). Lithotectonic subdivision of the metamorphic rocks from the eastern parts of the Central Rhodope extension structure. Review of the Bulgarian Geological Society, 65(1-3), 101-106.

Sarov, S., & Gerdjikov, I. (2002). Unroofing the Central Rhodopian Dome from the East---Kanarata Extensional Shear Zone. *Comptes Rendus de l'Academie Bulgare des Sciences*, *55*(2), 71.

Sarov, S., Voinova, E., Moskovski, S., Zhelezarski, T., Naydenov, K., Nikolov, D., Georgieva, I., Nedkova, K., Petrov, I. & Markov, I. (2007): Geological map of Bulgaria 1:50000, Map sheet K-35-74-A Hvoina, with explanatory notes. Geology and Geophysics Ltd., Sofia

Schmädicke, E., & Will, T. M. (2003). Pressure–temperature evolution of blueschist facies rocks from Sifnos, Greece, and implications for the exhumation of high-pressure rocks in the Central Aegean. *Journal of Metamorphic Geology*, *21*(8), 799-811.

Schmid, S.M., Bernoulli, D., Fügenschuh, B., Georgiev, N., Kounov, A., Matenco, L., Oberhänsli, R., Pleuger, J., Schefer, S., Ustaszewski, K. & van Hinsbergen, D. (in prep.) Map of the tectonic units of the Alpine collision zone between Eastern Alps and Western Turkey.

Schmid, S.M., Bernoulli, D., Fügenschuh, B., Matenco, L., Schefer, S., Oberhänsli, R., Ustaszewski, K. (2011). Tracing the closure of Neotethys from the Alps to Western Turkey II: Similarities and differences between Dinarides, Hellenides and Anatolides-Taurides. Geophysical Research Abstracts 13, EGU2011- 4000.

Schmid, S. M., Bernoulli, D., Fugenschuh, B., Matenco, L., Schefer, S., Schuster, R., Tischler, M. & Ustaszewski, K. (2008). The Alpine-Carpathian-Dinaridic orogenic system: correlation and evolution of tectonic units. Swiss Journal of Geosciences, 101(1), 139-183.

Sokoutis, D., Brun, J. P., Van Den Driessche, J., & Pavlides, S. (1993). A major Oligo-Miocene detachment in southern Rhodope controlling north Aegean extension. *Journal of the Geological Society*, *150*(2), 243-246.

Sonder, L. J., England, P. C., Wernicke, B. P., & Christiansen, R. L. (1987). A physical model for Cenozoic extension of western North America. *Geological Society, London, Special Publications*, *28*(1), 187-201.

Turpaud, P., & Reischmann, T. (2010). Characterisation of igneous terranes by zircon dating: implications for UHP occurrences and suture identification in the Central Rhodope, northern Greece. *International Journal of Earth Sciences*, *99*(3), 567-591.

Twinning, K. (…). Origin of plagiogranite in the Troodos ophiolite, Cyprus. Department pf Geosciences, Trinity University,715 Stadium Dr., San Antonio, TX 78212-7200, *Faculty sponsor: Diane R. Smith, Trinity University*

Underhill, J. R. (1989). Late Cenozoic deformation of the Hellenic foreland, western Greece. Geological Society of America Bulletin, 101(5), 613-634.

Van der Sluis, 2014

van Hinsbergen, D. J. J., Hafkenscheid, E., Spakman, W., Meulenkamp, J. E., & Wortel, R. (2005). Nappe stacking resulting from subduction of oceanic and continental lithosphere below Greece. *Geology*, *33*(4), 325-328.

Wawrenitza, N. & Mposkos, E. (1997). First evidence for Lower Cretaceous HP/HT-metamorphism in the eastern Rhodope, north Aegean Region, North-East Greece. European Journal of Mineralogy, 9(3), 659-664.

Wijbrans, J. R., & McDougall, I. (1988). Metamorphic evolution of the Attic Cycladic metamorphic belt on Naxos (Cyclades, Greece) utilizing 40Ar/39Ar age spectrum measurements. *Journal of Metamorphic Geology*, *6*(5), 571-594.

Wu, C. M., & Zhao, G. (2006). Recalibration of the garnet–muscovite (GM) geothermometer and the garnet–muscovite–plagioclase–quartz (GMPQ) geobarometer for metapelitic assemblages. *Journal of Petrology*, *47*(12), 2357-2368.

Wutrich, E. D. (2009). Low temperature thermochronology of the northern Aegean Rhodope massif, a dissertation submitted to the Swiss Federal Institute of Technology Zurich, for the degree of Doctor of Sciences.

Zachos, S. & Dimadis, E. (1983). The geotectonic position of the Skaloti-Echinos granite and its relationship to the metamorphic formations of Greek Western and Central Rhodope, *Geol. Balcanica*, 13(5), 17-24.

Zeffren, S., Avigad, D., Heimann, A., & Gvirtzman, Z. (2005). Age resetting of hanging wall rocks above a low-angle detachment fault: Tinos Island (Aegean Sea). *Tectonophysics*, *400*(1), 1-25.

Zhu, W.-P. & Wei, C.-J. (2007). Thermodynamic modelling of the phengite geobarometry. Science in China, Series D-Earth Sciences, vol. 50 (7), pp.: 1033-1039